Title

A Search for Extragalactic Fast Blue Optical Transients in ZTF and the Rate of AT2018cow-like Transients

Journal

The Astrophysical Journal, 949(2)

ISSN

0004-637X

Authors

Ho, Anna YQ
Perley, Daniel A
Gal-Yam, Avishay
et al.

Publication Date

2023-06-01

DOI

10.3847/1538-4357/acc533

The Astrophysical Journal, 949:120 (37pp), 2023 June 1 https://doi.org/10.3847/1538-4357/acc533

A Search for Extragalactic Fast Blue Optical Transients in ZTF and the Rate of AT2018cow-like Transients

Anna Y. Q. Ho[1,2,3,4], Daniel A. Perley[5], Avishay Gal-Yam[6], Ragnhild Lunnan[7], Jesper Sollerman[7], Steve Schulze[7], Kaustav K. Das[8], Dougal Dobie[9,10], Yuhan Yao[8], Christoffer Fremling[8], Scott Adams[8], Shreya Anand[11], Igor Andreoni[8], Eric C. Bellm[12], Rachel J. Bruch[13], Kevin B. Burdge[11], Alberto J. Castro-Tirado[14], Aishwarya Dahiwale[8], Kishalay De[8], Richard Dekany[15], Andrew J. Drake[8], Dmitry A. Duev[16], Matthew J. Graham[8], George Helou[17], David L. Kaplan[18], Viraj Karambelkar[8], Mansi M. Kasliwal[8], Erik C. Kool[7], S. R. Kulkarni[8], Ashish A. Mahabal[11,19], Michael S. Medford[20,21], A. A. Miller[22,23], Jakob Nordin[24], Eran Ofek[6], Glen Petitpas[25], Reed Riddle[15], Yashvi Sharma[8], Roger Smith[15], Adam J. Stewart[26], Kirsty Taggart[27], Leonardo Tartaglia[28,29], Anastasios Tzanidakis[8], and Jan Martin Winters[30]

[1] Miller Institute for Basic Research in Science, 468 Donner Lab, Berkeley, CA 94720, USA; annayqho@cornell.edu
[2] Department of Astronomy, University of California, Berkeley, 501 Campbell Hall, Berkeley, CA, 94720, USA
[3] Lawrence Berkeley National Laboratory, 1 Cyclotron Road, MS 50B-4206, Berkeley, CA 94720, USA
[4] Department of Astronomy, Cornell University, Ithaca, NY 14853, USA
[5] Astrophysics Research Institute, Liverpool John Moores University, IC2, Liverpool Science Park, 146 Brownlow Hill, Liverpool L3 5RF, UK
[6] Department of Particle Physics and Astrophysics, Weizmann Institute of Science, 234 Herzl St., 76100 Rehovot, Israel
[7] The Oskar Klein Centre, Department of Astronomy, Stockholm University, AlbaNova, SE-10691 Stockholm, Sweden
[8] Cahill Center for Astrophysics, California Institute of Technology, MC 249-17, 1200 E. California Boulevard, Pasadena, CA, 91125, USA
[9] Centre for Astrophysics and Supercomputing, Swinburne University of Technology, Hawthorn, Victoria, Australia
[10] ARC Centre of Excellence for Gravitational Wave Discovery (OzGrav), Hawthorn, Victoria, Australia
[11] Division of Physics, Mathematics and Astronomy, California Institute of Technology, Pasadena, CA 91125, USA
[12] DIRAC Institute, Department of Astronomy, University of Washington, 3910 15th Avenue NE, Seattle, WA 98195, USA
[13] Department of Particle Physics and Astrophysics Weizmann Institute of Science 234 Herzl St., 76100 Rehovot, Israel
[14] Instituto de Astrofísica de Andalucía (IAA-CSIC) Glorieta de la Astronomia E-18008, Granada, Spain
[15] Caltech Optical Observatories, California Institute of Technology, Pasadena, CA 91125, USA
[16] Division of Physics, Mathematics, and Astronomy, California Institute of Technology, Pasadena, CA 91125, USA
[17] IPAC, California Institute of Technology, 1200 E. California Blvd., Pasadena, CA 91125, USA
[18] Center for Gravitation, Cosmology, and Astrophysics, Department of Physics, University of Wisconsin-Milwaukee, P.O. Box 413, Milwaukee, WI 53201, USA
[19] Center for Data Driven Discovery, California Institute of Technology, Pasadena, CA 91125, USA
[20] Department of Astronomy, University of California, Berkeley, Berkeley, CA 94720, USA
[21] Lawrence Berkeley National Laboratory, 1 Cyclotron Rd., Berkeley, CA 94720, USA
[22] Center for Interdisciplinary Exploration and Research in Astrophysics (CIERA) and Department of Physics and Astronomy, Northwestern University, 1800 Sherman Road, Evanston, IL 60201, USA
[23] The Adler Planetarium, Chicago, IL 60605, USA
[24] Institute of Physics, Humboldt-Universität zu Berlin, Newtonstr. 15, D-12489 Berlin, Germany
[25] Harvard-Smithsonian Center for Astrophysics, 60 Garden Street, Cambridge, MA 02138, USA
[26] Sydney Institute for Astronomy, School of Physics, The University of Sydney, NSW 2006, Australia
[27] Department of Astronomy and Astrophysics, University of California, Santa Cruz, CA 95064, USA
[28] The Oskar Klein Centre, Department of Astronomy, AlbaNova, SE-106 91 Stockholm, Sweden
[29] INAF—Osservatorio Astronomico di Padova, Vicolo dell'Osservatorio 5, I-35122 Padova, Italy
[30] Institut de Radioastronomie Millimétrique (IRAM), 300 rue de la Piscine, F-38406 St. Martin d'Héres, France
Received 2021 May 18; revised 2023 February 21; accepted 2023 February 28; published 2023 June 5

Abstract

We present a search for extragalactic fast blue optical transients (FBOTs) during Phase I of the Zwicky Transient Facility (ZTF). We identify 38 candidates with durations above half-maximum light 1 day $< t_{1/2} <$ 12 days, of which 28 have blue ($g - r \lesssim -0.2$ mag) colors at peak light. Of the 38 transients (28 FBOTs), 19 (13) can be spectroscopically classified as core-collapse supernovae (SNe): 11 (8) H- or He-rich (Type II/IIb/Ib) SNe, 6 (4) interacting (Type IIn/Ibn) SNe, and 2 (1) H&He-poor (Type Ic/Ic-BL) SNe. Two FBOTs (published previously) had predominantly featureless spectra and luminous radio emission: AT2018lug (The Koala) and AT2020xnd (The Camel). Seven (five) did not have a definitive classification: AT 2020bdh showed tentative broad Hα in emission, and AT 2020bot showed unidentified broad features and was 10 kpc offset from the center of an early-type galaxy. Ten (eight) have no spectroscopic observations or redshift measurements. We present multiwavelength (radio, millimeter, and/or X-ray) observations for five FBOTs (three Type Ibn, one Type IIn/Ibn, one Type IIb). Additionally, we search radio-survey (VLA and ASKAP) data to set limits on the presence of radio emission for 24 of the transients. All X-ray and radio observations resulted in nondetections; we rule out AT2018cow-like X-ray and radio behavior for five FBOTs and more luminous emission (such as that seen in the Camel) for four additional FBOTs. We conclude that exotic transients similar to AT2018cow, the Koala, and the Camel represent a rare subset of FBOTs and use ZTF's SN classification experiments to measure the rate to be at most 0.1% of the local core-collapse SN rate.

Unified Astronomy Thesaurus concepts: Transient sources (1851); Time domain astronomy (2109); Core-collapse supernovae (304); Surveys (1671)

Supporting material: machine-readable tables

1. Introduction

In the past decade, high-cadence optical surveys have uncovered a variety of extragalactic transients with light curves that evolve faster than those of established supernova (SN) classes. As reviewed in Inserra (2019), rapid transients have diverse origins, including massive-star explosions with low ejecta masses, thermonuclear explosions, and interaction-powered SNe. In recent years, a subset of rapid transients dubbed "fast blue optical transients" (FBOTs; Drout et al. 2014; Pursiainen et al. 2018; Margutti et al. 2019) have attracted significant attention owing to the discovery of luminous X-ray (Rivera Sandoval et al. 2018; Ho et al. 2019b; Margutti et al. 2019), radio (Margutti et al. 2019), and submillimeter (Ho et al. 2019b) emission accompanying the nearby ($d = 60$ Mpc) FBOT AT2018cow (Prentice et al. 2018; Perley et al. 2019).

A commonly used definition of "FBOT" is blue colors ($g - r \lesssim -0.2$ mag) at peak light and a short duration above half-maximum light ($t_{1/2} \lesssim 12$ days) (Inserra 2019). Approximately 100 FBOTs have been discovered in archival searches, the vast majority too late for spectroscopic follow-up observations (Drout et al. 2014; Pursiainen et al. 2018). Single-object studies suggest that some FBOTs arise from shock interaction with a dense wind (Ofek et al. 2010) or shell (Rest et al. 2018; Ho et al. 2019a), with spectral types ranging from hydrogen-rich (Ofek et al. 2010) to hydrogen-poor (Ho et al. 2019a; Pritchard et al. 2021).

In the past few years, the improved grasp of optical surveys (Bellm 2016; Ofek & Ben-Ami 2020) has made the discovery of rapid transients routine. In this paper we present the first sample of FBOTs with spectroscopic classifications, using data from the Zwicky Transient Facility (ZTF; Bellm et al. 2019b; Graham et al. 2019) high-cadence surveys (Bellm et al. 2019a). In Section 2 we present our selection criteria and the ZTF FBOT sample. In Section 3 we analyze the photometric and spectroscopic evolution of the ZTF FBOTs, set limits on accompanying X-ray and radio emission, and identify several subtypes. We conclude that AT2018cow-like FBOTs are rare, and we estimate their rate in Section 4. We discuss the implications of our work for the progenitors in Section 5, and we summarize in Section 6.

Throughout the paper we assume a flat Λ CDM cosmology with $H_0 = 67.7$ km s^{-1} Mpc^{-1} and $\Omega_M = 0.307$ (Planck Collaboration et al. 2016). Times are presented in UTC, and magnitudes are given in AB. The optical photometry and spectroscopy will be made public through WISeREP, the Weizmann Interactive Supernova Data Repository (Yaron & Gal-Yam 2012).

2. Observations and Selection Criteria

2.1. ZTF

The ZTF custom mosaic camera (Dekany et al. 2020) is mounted on the 48-inch Samuel Oschin Telescope (P48) at Palomar Observatory. As summarized in Bellm et al. (2019a), observing time for ZTF Phase I was divided between public (40%), partnership (40%), and Caltech surveys (20%). Three custom filters are used ($g_{\rm ZTF}$, $r_{\rm ZTF}$, and $i_{\rm ZTF}$; hereafter g, r, and i; Dekany et al. 2020), and images reach a typical dark-time limiting magnitude of $r \sim 20.5$ mag.

Images are processed and reference-subtracted by the IPAC ZTF pipeline (Masci et al. 2019) using the Zackay et al. (2016) image subtraction algorithm. Every 5σ point-source detection is saved as an "alert." Alerts are distributed in Avro format (Patterson et al. 2019) and can be filtered based on a machine-learning real-bogus metric (Duev et al. 2019; Mahabal et al. 2019); host galaxy characteristics, including a star−galaxy classifier (Tachibana & Miller 2018); and light-curve properties. During the time period relevant for this paper (ZTF Phase I), the collaboration used a web-based system called the GROWTH marshal (Kasliwal et al. 2019) to identify, monitor, and coordinate follow-up observations for transients of interest.

Although we use observations from all programs, the most effective surveys for discovering FBOTs are the high-cadence partnership survey (HC), which covered 2500 deg^2 with six visits per night (three in r and three in g); the ZTF Uniform Depth Survey (ZUDS[31]), which covered 2500 deg^2 with six visits per night (2r, 2g, and 2i); the 1-day cadence Caltech survey (1DC), which covered 3000 deg^2 with 1r and 1g visit per night; and 1-day cadence observations for shadowing the Transiting Exoplanet Survey Satellite (TESS; Ricker et al. 2014) fields.

2.2. ZTF Sample Selection

We searched data from ZTF Phase I, i.e., obtained from 2018 March through 2020 October. We used `ztfquery` (Rigault 2018) to identify fields in the primary grid with $E(B-V) < 0.3$ mag at the central field coordinate, and we only searched field nights that had at least one observation in the same field within the preceding and subsequent five nights. This left a total of 127,487 field nights.

For each of the 127,487 field nights, we searched for transients fulfilling the criteria laid out in Table 1. We performed the search with the following steps:

1. We applied basic cuts to remove artifacts and stellar phenomena. We kept sources with a real-bogus score rb > 0.5 (Mahabal et al. 2019) and a deep-learning score braai > 0.8 (Duev et al. 2019). The `braai` score corresponds to a false-positive rate of 0.7% and a false-negative rate of 3% (Duev et al. 2019). We removed sources within 2″ of a counterpart with a star−galaxy score greater than 0.76 (Tachibana & Miller 2018) and sources within 15″ of a bright ($r < 15$ mag) star. We removed sources that arose from negative subtractions. This left ∼2.5 M unique sources.
2. We required that each source be detected in at least three alerts, leaving 651,920 sources.
3. To remove flaring and long-duration transients, we required that the time from the first to last detection (including the 30-day history in the alert packets, which uses a lower threshold than issued alerts) is between 1

[31] https://github.com/zuds-survey/zuds-pipeline

Table 1
Steps for Selecting Transients with Optical Light-curve Durations 1 day $< t_{1/2} <$ 12 Days in ZTF Data

Step[a]	Criteria	No. Candidates
1	Basic cuts on subtractions	2.5M
2	Candidate has $\geqslant$3 alerts	651,920
3	Light curve has short duration	19,715
4	Light curve is well sampled	6059
5	Fast-rising in g or r	1779
6	Manual inspection	38

Note.
[a] Details on each step are provided in the text.

and 120 days.[32] Following the FBOT definition commonly adopted in the literature (Drout et al. 2014; Inserra 2019), we required that the duration above half-maximum of the light curve be 1 day $< t_{1/2} <$ 12 days. We applied the cut to the g-band light curve. This left 19,715 sources.

4. Because color is an important characteristic of FBOTs, we required that the light curve be well sampled with multiband photometry, i.e., that there is a P48 observation (resulting in either an upper limit or a detection) within 5.5 days of the peak of the g-band light curve, before and after, in g band and r band. This left 6059 sources.
5. We further required the source to be fast-rising—that in either g band or r band it rose 1 mag in the preceding 6.5 days. This left 1779 sources.
6. We examined each of the 1779 sources manually and removed events (75% of the total) that passed Step 5 only on the basis of spurious nondetections in between detections. We discarded an additional 20% of events for having a point-like counterpart[33] (making particular use of the eighth data release of the Legacy Survey; Dey et al. 2019), repeated flaring behavior, or spectroscopic classifications indicating that they were stellar outbursts. We used forced photometry (Yao et al. 2019) to confirm a short event duration of 1 day $< t_{1/2,g} <$ 12 days. This left 38 sources.

The 38 ZTF transients with 1 day $< t_{1/2,g} <$ 12 days and well-sampled light curves are listed in Table 2. Most were identified in the HC and 1DC surveys in real time by filters explicitly designed to find rapidly evolving transients (Ho et al. 2020a; Perley et al. 2021b), and the details of their discovery and follow-up are provided in Appendix A. Several of the objects in Table 2 have been previously published: the Type Ibn SN 2018bcc (Karamehmetoglu et al. 2021), the ultrastripped Type Ib candidate SN 2019dge (Yao et al. 2020), the Type Ic-BL SN 2018gep (Ho et al. 2019a), and the radio-loud transients AT 2018lug (the "Koala"; Ho et al. 2020b) and AT 2020xnd (the "Camel"; Perley et al. 2021b).

Our requirement of multiband photometry (Step 4) excludes some known rapidly evolving transients, including AT2018cow itself (which was only observed by ZTF in the r-band filter for the first month), the Type IIb SN 2018jak (Perley et al. 2020), and the Type Ibn SN 2019aajs (Kool et al., in preparation). In addition, two rapidly evolving Type Icn SNe, SN 2019hgp (Bruch et al. 2019; Gal-Yam 2021) and SN 2021csp (Perley 2021; Perley et al. 2021a), do not pass our cuts: SN 2019hgp had too long a duration, and SN 2021csp occurred outside the date range we considered. Our goal is to provide a systematically selected sample of well-observed objects, not a fully complete sample of rapidly evolving transients in ZTF.

Previous searches (e.g., Drout et al. 2014) have found that a cut of 1 day $< t_{1/2} <$ 12 days primarily (but not exclusively) selects events with blue colors ($g - r \lesssim -0.2$ mag) at peak light, leading to the term FBOT (e.g., Inserra 2019; Margutti et al. 2019). To estimate the peak $g-r$ color of the ZTF transients in Table 2, we used the r-band magnitude closest to the peak of the g-band light curve, which was within 1 day in all cases but one. As shown in Table 2, similarly to Drout et al. (2014), we find that most (28 of the 38) objects have $g - r \lesssim -0.2$ mag at peak light. The remaining 10 objects have redder colors at peak and would not be referred to as FBOTs, such as the Type Ic SN 2020ano. However, a strict peak-light color criterion will exclude FBOTs that are dust extinguished. Therefore, in this paper we present data for all 38 events in Table 2 but limit our use of the term FBOT to the 28 events with blue colors at peak light, which more closely resemble transients referred to as FBOTs in the literature. Light curves for the ZTF FBOTs with redshift measurements are shown in Figure 1. Light curves for all remaining objects in Table 2 are shown in Figure 15 in Appendix B.

2.3. Literature Sample Selection

We supplement the ZTF-selected events from Section 2.2 with objects from the literature. The literature transients are listed in Table 3, and a subset of their light curves are shown in Figure 2. To be consistent, we apply similar selection criteria: we require 1 day $< t_{1/2} <$ 12 days in a filter as close to rest-frame g-band as possible, an observation in that filter 5.5 days before the peak, and an observation in that filter within 5.5 days after the peak. We also require a redshift measurement. We measured the duration in as close to rest-frame g band as possible, since a number of the literature objects are at a significantly higher redshift than the ZTF objects. We estimate the peak absolute magnitude using

$$M = m_{\rm obs} - 5\log_{10}\left(\frac{D_L}{10\ {\rm pc}}\right) + 2.5\log_{10}(1+z). \quad (1)$$

Table 3 includes the radio- and X-ray-loud transients AT2018cow (Prentice et al. 2018) and AT2020mrf (Yao et al. 2022), as well as the PS1 (Drout et al. 2014) and DES (Pursiainen et al. 2018) samples, which are widely discussed as FBOTs in the literature (Fox & Smith 2019; Inserra 2019; Margutti et al. 2019; Coppejans et al. 2020; Lyutikov 2022). We include KSN2015K (Rest et al. 2018), SNLS04D4ec (Arcavi et al. 2016), and iPTF16asu (Whitesides et al. 2017), all of which have been referred to as FBOTs (Inserra 2019; Margutti et al. 2019; Coppejans et al. 2020), as well as SN 2019bkc (Chen et al. 2020; Prentice et al. 2020b), described as an FBOT in Inserra (2019) and Margutti et al. (2019). We include several interacting (Type IIn/Ibn) SNe (Ofek et al. 2010; Pastorello et al. 2015; Hosseinzadeh et al. 2017) whose similarity to FBOTs in terms of light curves and colors has been pointed out by others (Fox & Smith 2019;

[32] Intranight ($t < 1$ day) transients are presented in separate work (Ho et al. 2020a; Andreoni et al. 2020; Ho et al. 2022b).
[33] Extragalactic transients in compact hosts could accidentally be removed by this step. However, we found it important for removing outbursts from cataclysmic variables.

Table 2
Candidate Extragalactic Transients from ZTF Phase I with Durations 1 day $< t_{1/2,g} <$ 12 days and Well-sampled Light Curves

ZTF Name	R.A. (J2000)	Decl. (J2000)	IAU Name	Peak MJD	Peak Mag	$t_{1/2,g}$ (days)	$g-r$ (mag)	z	Class[d]	References
18aakuewf	16:14:22.65	+35:55:04.4	SN 2018bcc	58230.38	17.46 ± 0.04	9.1 ± 0.4	−0.3	0.0636	Ibn	1
18abfcmjw[e]	17:36:46.74	+50:32:52.1	SN 2019dge	58583.16	18.40 ± 0.02	6.1 ± 0.2	−0.2	0.0213	Ib	2
18abianhw	19:23:40.60	+44:48:30.1	AT2018lwd	58318.41	19.55 ± 0.05	6.8 ± 1.0	−0.2	⋯	⋯	⋯
18abukavn[e]	16:43:48.20	+41:02:43.3	SN 2018gep	58374.22	15.91 ± 0.01	9.3 ± 0.2	−0.4	0.03154	Ic-BL	3, 4
18abvkmgw	00:37:26.87	+15:00:51.2	SN 2018ghd	58377.35	18.49 ± 0.03	9.5 ± 0.9	−0.1	0.03923	Ib	5, 6
18abvkwla[e]	02:00:15.19	+16:47:57.3	AT2018lug	58374.41	19.34 ± 0.05	4.0 ± 0.1	−0.6	0.2714	Feat.;RL[b]	7
18abwkrbl	02:16:15.58	+28:35:28.6	SN 2018gjx	58379.44	15.58 ± 0.01	7.4 ± 0.1	−0.2	0.00999	IIb	8
19aankdan	11:53:47.14	+44:44:44.8	AT2019dcm	58572.27	19.09 ± 0.04	9.8 ± 0.6	−0.1	⋯	⋯	9
19aapfmki[f]	14:05:43.56	+09:30:56.6	SN 2019deh	58587.33	17.22 ± 0.02	10.7 ± 0.7	−0.2	0.05469	Ibn	10, 11, 12
19aapuudk	15:10:03.55	+38:07:11.8	AT2019aajt	58585.27	19.49 ± 0.05	5.7 ± 0.7	−0.3	⋯	⋯	⋯
19aasexmy	13:31:54.39	+25:44:05.9	AT2019aaju	58599.33	19.41 ± 0.02	10.3 ± 1.5	−0.3	⋯	⋯	⋯
19aatoboa	12:25:40.57	+44:44:48.8	AT2019esf	58609.22	18.84 ± 0.03	7.2 ± 0.6	−0.4	0.0758	⋯	13
19abeyvoi	23:50:15.80	+08:07:05.3	AT2019lbr	58675.45	19.09 ± 0.04	9.2 ± 0.8	−0.4	⋯	⋯	14, 15
19abfarpa	11:07:09.56	+57:06:03.2	AT2019kyw	58676.18	18.28 ± 0.04	11.9 ± 0.5	−0.2	0.074	⋯	⋯
19abobxik[f]	00:43:43.12	+37:03:38.9	SN 2019myn	58706.45	18.84 ± 0.02	9.5 ± 0.8	−0.1	0.1	Ibn	⋯
19abrpfps	18:36:27.30	+45:05:32.0	AT2019aajv	58720.22	19.48 ± 0.03	3.4 ± 0.5	−0.4	⋯	⋯	⋯
19abuvqgw	19:50:06.37	+66:04:56.5	SN 2019php	58730.30	18.68 ± 0.06	8.4 ± 0.4	−0.2	0.087	Ibn	16
19abyjzvd[f]	16:48:12.90	+48:04:50.0	SN 2019qav	58739.13	18.99 ± 0.06	10.8 ± 0.5	−0.3	0.1353	IIn/Ibn	17
19acaxbjt	23:12:35.94	+09:02:07.9	AT2019qwx	58754.20	19.03 ± 0.04	9.9 ± 0.7	−0.3	⋯	⋯	18
19acayojs	21:22:41.87	+22:52:54.8	SN 2019rii	58757.18	18.75 ± 0.02	10.0 ± 0.4	−0.1	0.1234	Ibn	19
19accjfgv	08:28:49.30	+75:19:41.0	SN 2019rta	58759.43	17.88 ± 0.02	6.8 ± 0.4	−0.1	0.027	IIb	20
19accxzsc	03:26:14.73	+04:47:26.7	AT2019scr	58763.42	18.91 ± 0.05	3.5 ± 1.5	−0.7[a]	⋯	⋯	21
19acsakuv	06:21:15.36	+53:16:39.5	AT2019van	58800.55	18.54 ± 0.11	6.4 ± 1.7	−0.4	⋯	⋯	22
20aaelulu[e]	12:22:54.92	+15:49:25.0	SN 2020oi	58862.48	14.06 ± 0.12	11.0 ± 0.6	0.1	0.0052	Ic	23, 24, 25
20aahfqpm	13:06:25.19	+53:28:45.5	SN 2020ano	58871.45	19.06 ± 0.03	3.4 ± 2.0	−0.5	0.03113	IIb	⋯
20aaivtof	02:48:18.49	−09:26:52.8	AT2020bdh	58875.16	18.60 ± 0.03	8.9 ± 1.4	−0.1	0.04106	IIn?	26, 27
20aakypiu	11:31:13.75	+34:30:00.7	AT2020bot	58880.45	19.46 ± 0.04	3.7 ± 0.4	−0.1	0.197	UB[c]	28
20aaxhzhc	13:36:05.01	+28:59:00.1	SN 2020ikq	58971.30	18.27 ± 0.03	11.8 ± 1.8	−0.2	0.042	IIb	29, 30
20aayrobw	09:31:13.19	+38:15:14.4	SN 2020jmb	58981.17	18.51 ± 0.03	10.0 ± 0.4	−0.5	0.061	II	31
20aazchcq	14:41:40.57	+19:20:56.9	SN 2020jji	58979.25	19.50 ± 0.09	10.8 ± 1.0	0.4	0.03788	II	32
20aazrcbp	11:02:20.89	+30:51:52.1	AT2020mlq	58986.21	19.71 ± 0.06	11.0 ± 0.8	0.0	⋯	⋯	33
20ababxjv	16:28:39.48	+56:13:40.6	AT2020kfw	58991.33	19.05 ± 0.03	8.4 ± 0.3	−0.2	0.059	⋯	34
20abmocba	16:34:38.89	+50:59:26.5	AT2020aexw	59051.26	19.39 ± 0.03	10.5 ± 0.4	−0.2	0.0734	⋯	⋯
20abummyz	16:50:45.92	+30:45:14.9	AT2020yqt	59080.21	19.17 ± 0.11	4.0 ± 1.0	−0.6	0.0986	Feat.	35
20aburywx[f]	01:19:56.51	+38:11:09.5	SN 2020rsc	59081.47	19.36 ± 0.07	3.3 ± 0.3	−0.2	0.0313	IIb	36
20acigmel[e]	22:20:02.02	−02:50:25.3	AT2020xnd	59136.21	19.24 ± 0.04	5.6 ± 1.6	−0.4	0.2442	UB;RL	37
20acigusw	22:50:25.37	+08:50:41.8	SN 2020vyv	59134.23	18.68 ± 0.03	5.6 ± 0.3	−0.3	0.062	II?	38
20aclfmwn	08:17:11.29	+64:31:34.7	SN 2020xlt	59141.45	19.59 ± 0.04	4.0 ± 0.5	−0.2	0.0384	IIb	⋯

Notes.
[a] The closest r-band detection was 2 days from the peak g-band measurement; for all other sources in the table, the g and r measurements were within 1 day of each other.
[b] Feat.: high-S/N featureless spectrum at peak light. RL: radio-loud.
[c] UB: unidentified broad features in spectrum.
[d] For a detailed review of the SN classifications in this table, see Gal-Yam (2017) and Smith et al. (2017). Briefly, Type II SNe have hydrogen P Cygni features, and Type Ib and Ic SNe lack hydrogen and helium, respectively. Type Ic-BL SNe have particularly broad P Cygni features indicative of large ejecta velocities ($v >$ 20,000 km s^{-1}). Type Ibn and Type IIn SNe have spectra dominated by emission lines of helium and hydrogen, respectively.
[e] Previously published multiwavelength (UV, X-ray, and/or radio) observations available.
[f] Multiwavelength observations published as part of this paper.
References. Published or classified by (1) Karamehmetoglu et al. 2021; (2) Yao et al. 2020; (3) Ho et al. 2019a; (4) Pritchard et al. 2021; (5) Tonry et al. 2018a; (6) Fremling et al. 2018; (7) Ho et al. 2020b; (8) Prentice et al. 2020a; (9) Nordin et al. 2019c; (10) Nordin et al. 2019a; (11) Prentice et al. 2019; (12) Pellegrino et al. 2022; (13) Nordin et al. 2019b; (14) Tonry et al. 2019a; (15) Wiseman et al. 2019; (16) Tonry et al. 2019b; (17) Chambers et al. 2019; (18) Forster 2019; (19) Förster et al. 2021; (20) Dahiwale & Fremling 2019; (21) Tonry et al. 2019c; (22) Nordin et al. 2019f; (23) Horesh et al. 2020; (24) Rho et al. 2021; (25) Gagliano et al. 2022; (26) Smith et al. 2020b; (27) Forster et al. 2020d; (28) Nordin et al. 2020; (29) Tonry et al. 2020; (30) Angus 2020; (31) Dahiwale & Fremling 2020a; (32) De 2020a; (33) Marques-Chaves et al. 2020; (34) Forster et al. 2020a; (35) Chambers et al. 2020; (36) Forster et al. 2020c; (37) Perley et al. 2021b; (38) Siebert et al. 2020.
(This table is available in machine-readable form.)

Margutti et al. 2019). We also include the Type Ic SNe SN 2018kzr (McBrien et al. 2019), SN 1999cq (Matheson et al. 2000), and SN 2005ek (Drout et al. 2013), which have been described as FBOTs (Pursiainen et al. 2018; Coppejans et al. 2020; Wiseman et al. 2020; Chen & Shen 2022). We include AT2018lqh (Ofek et al. 2021) and HSC17bhyl (Tampo et al. 2020), described as FBOTs in Lyutikov (2022) and Coppejans et al. (2020). We also include

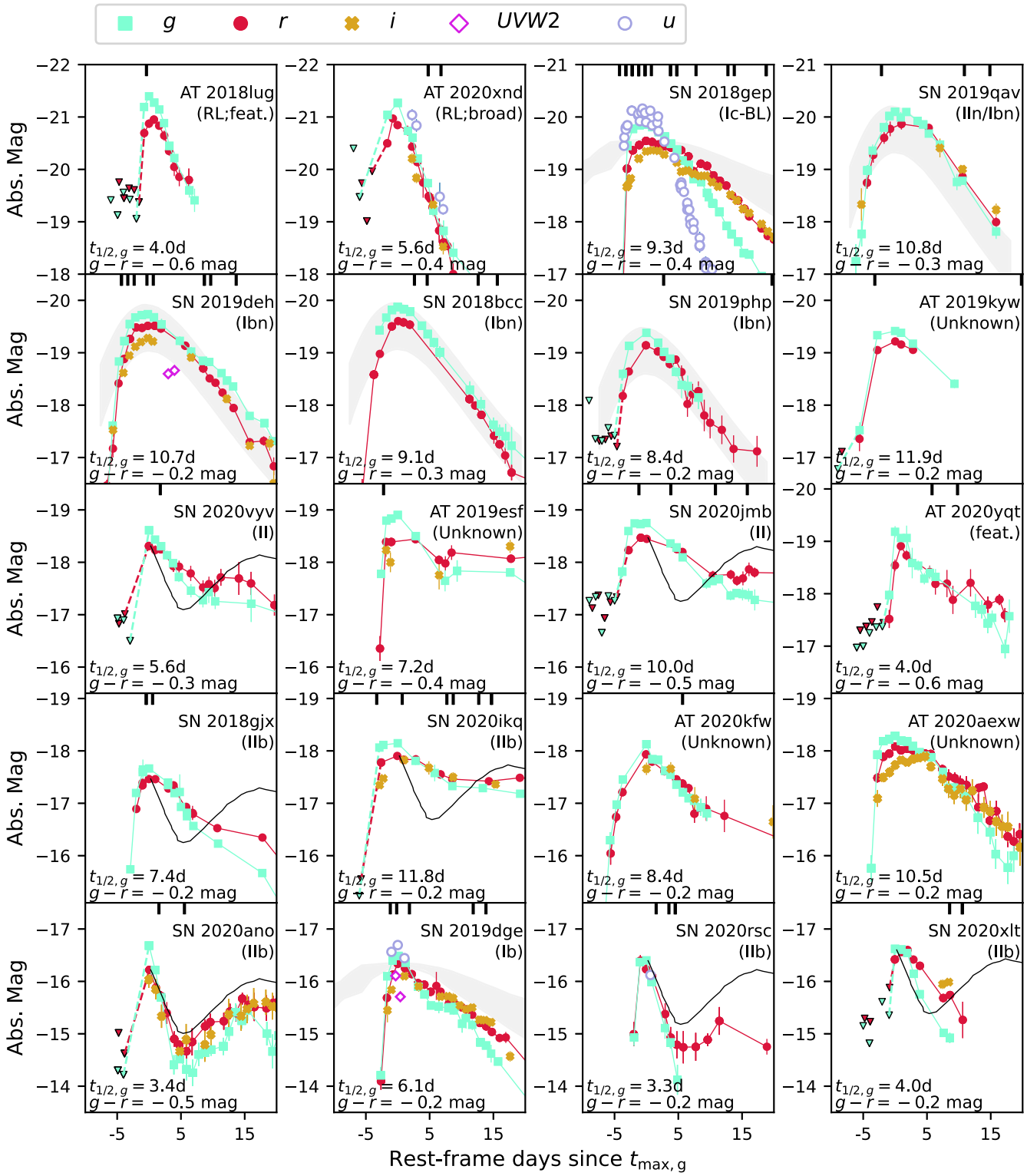

Figure 1. Light curves of ZTF FBOTs with redshift measurements. FBOTs were selected on the basis of duration above half-maximum light and peak color: 1 day $< t_{1/2} <$ 12 days and $g - r \leqslant -0.2$ mag. Upper limits are indicated with triangles, and dashed lines connect nondetections to detections. Epochs of spectroscopy are indicated with vertical lines along the top of each panel. The contrast in each panel is 4 mag along the *y*-axis and 30 days along the *x*-axis. In panels with Type Ibc and Type Ibn SNe we show Type Ibc and Type Ibn light-curve templates (Drout et al. 2011; Hosseinzadeh et al. 2017) for reference, scaled to the peak of the light curve. The gray region of the Type Ibc template is the standard deviation of a set of interpolated light curves (Drout et al. 2011). The gray region of the Type Ibn template contains 95% of the photometric points in a light-curve sample (Hosseinzadeh et al. 2017). For the Type II and Type IIb SNe we show the *V*-band light curve of the Type IIb SN 1993J for reference (Schmidt et al. 1993). In some cases light curves have been binned by day for clarity. Light curves of all remaining transients from Table 2 are shown in Figure 15 in the Appendix B

the fast transient SN 1885A (de Vaucouleurs & Corwin 1985; Perets et al. 2011). In addition, the calcium-rich transient SN 2019ehk (Jacobson-Galán et al. 2020), which has been referred to as Type IIb (De et al. 2021), passes the selection criteria laid out in Section 2.2 because the shock-cooling peak

Table 3
Literature FBOTs with Redshift Measurements and Well-sampled Light Curves

Name	Redshift	Class	Filter	M_{max}[a] (mag)	$t_{1/2,rise}$[b] (days)	$t_{1/2,fade}$[b] (days)	References
SNLS04D4ec[c]	0.593	Unknown	*i*	−20.26 ± 0.03	<3.81	8.60 ± 0.43	1
PTF09uj[d]	0.065	IIn	*r*	−19.09 ± 0.04	2.04 ± 0.76	5.05 ± 1.92	2
PS1-10ah[e]	0.074	Unknown	*g*	−17.5 ± 0.11	1.0 ± 0.1	6.3 ± 0.6	3
PS1-10bjp	0.113	Unknown	*g*	−18.2 ± 0.11	1.0 ± 0.1	7.7 ± 0.6	3
PS1-11qr	0.324	Unknown	*r*	−19.3 ± 0.08	2.9 ± 0.1	8.7 ± 0.4	3
PS1-12bb	0.101	Unknown	*g*	−16.97 ± 0.12	<1.8	6.3 ± 0.3	3
PS1-12bv	0.405	Unknown	*r*	−19.1 ± 0.11	<2.2	3–9	3
PS1-12brf	0.275	Unknown	*r*	−18.3 ± 0.08	<1.0	8.8 ± 0.6	3
PS1-13dwm	0.245	Unknown	*r*	−17.5 ± 0.13	<3.0	3–7	3
PTF12ldy[f]	0.106	Ibn	*R*	−19.20 ± 0.02	3.34 ± 0.17	7.57 ± 0.29	4
LSQ13ccw	0.0603	IIn/Ibn?	*g*	−18.4 ± 0.2	1.39 ± 0.10	3.86 ± 0.31	5
iPTF14aki	0.064	Ibn	*R*	−19.30 ± 0.03	3.34 ± 0.17	7.58 ± 0.30	4
iPTF15akq	0.109	Ibn	*R*, *r*	−18.62 ± 0.31	3.13 ± 0.61	8.86 ± 0.80	4
iPTF15ul	0.066	Ibn?	*g*	−21.2 ± 0.3	1.53 ± 0.05	3.72 ± 0.08	4
KSN2015K[d]	0.090	Unknown	Kepler clear	−18.78	1.15	5.54	6
DES16E2pv[d]	0.73	Unknown	*i*	−19.98 ± 0.65	0.71 ± 0.42	2.04 ± 1.54	7
DES15S1fli	0.45	Unknown	*r*	−19.62 ± 0.11	<3.39	8.60 ± 1.42	7
DES17X3cds	0.49	Unknown	*i*	−19.09 ± 0.06	3.20–5.42	5.51 ± 0.83	7
DES16C2ggt	0.31	Unknown	*r*	−18.12 ± 0.08	<2.93	6.32 ± 1.55	7
DES16C1cbd	0.54	Unknown	*i*	−19.38 ± 0.10	1.76 ± 0.27	5.84 ± 0.77	7
DES13X3gmd	0.78	Unknown	*i*	−19.25 ± 0.22	<3.75	7.37 ± 4.14	7
DES14S2pli	0.35	Unknown	*r*	−18.64 ± 0.06	<3.83	7.16 ± 1.63	7
DES13X3gms	0.65	Unknown	*i*	−19.47 ± 0.06	1.85–6.22	9.94 ± 1.76	7
DES15C3mgq	0.23	Unknown	*r*	−16.92 ± 0.06	<2.65	8.37 ± 0.35	7
DES17C3gen	0.92	Unknown	*z*	−19.55 ± 0.22	1.88–4.02	5.59 ± 2.59	7
DES14C3tnz	0.70	Unknown	*i*	−19.16 ± 0.16	2.40–4.46	5.51 ± 2.72	7
DES15E2nqh	0.52	Unknown	*i*	−19.22 ± 0.24	3.04–7.34	5.86 ± 2.17	7
DES17S2fee	0.24	Unknown	*r*	−17.98 ± 0.07	<3.27	5.87 ± 1.72	7
DES16X3cxn	0.58	Unknown	*i*	−19.37 ± 0.06	2.80–5.93	6.62 ± 0.42	7
DES16X1eho	0.81	Unknown	*z*	−21.02 ± 0.14	1.23–2.41	1.33 ± 0.26	7
DES13X1hav	0.58	Unknown	*i*	−19.57 ± 0.21	<1.63	5.90 ± 3.11	7
iPTF16asu[c]	0.187	Ic-BL	*g*	−20.3 ± 0.1	1.14 ± 0.13	10.62 ± 0.55	8
AT2018cow	0.0141	IIn/Ibn?RL[g]	*g*	−20.87 ± 0.05	1.10 ± 0.04	1.96 ± 0.12	9, 10
SN 2018kzr[h]	0.054	Ic	*g*	−18.80 ± 0.08	<2.0	1.6 ± 0.2	11
SN 2019bkc[i]	0.0209	Ic	*g*	−17.16 ± 0.03	5.28 ± 0.38	2.22 ± 0.10	12, 13
AT2018lqh	0.05446	Unknown	*g*	−16.96 ± 0.18	0.61 ± 0.06	1.54 ± 0.23	16
SN 2019ehk	0.00524	Ca-rich/IIb	*g*	−14.70 ± 0.02	1.31 ± 0.04	1.93 ± 0.06	15, 24
SN 2019aajs	0.0358	Ibn	*g*	−18.86 ± 0.03	2.11 ± 0.03	6.05 ± 0.24	14
SN 2019rsq	0.031	IIb	*g*	−16.47 ± 0.09	4.7 ± 0.4	4.4 ± 0.1	20
AT2020mrf	0.1353	UB;RL[j]	*g*	−20.0 ± 0.1	2.4 ± 0.2	4.8 ± 0.2	17
SN 1999cq	0.0263	Ic	*R*	−19.6	<3.95	9.6	18
HSC17bhyl	0.750	Unknown	*i*	−18.49 ± 0.04	2.38 ± 0.31	7.15 ± 1.95	19
SN 1885A	(In M31)	Unknown	*V*	−18.4 ± 0.4	$\lesssim$5	$\lesssim$5	21, 22
SN 2005ek	0.01662	Ic	*R*	−17.26 ± 0.15	2–4	5	23
SN 2021csp	0.084	Icn	*g*	−20.1	2.5 ± 0.5	8.3 ± 1.0	25
SN 2019jc	0.01948	Icn	*g*	−17.2 ± 0.1	2.6 ± 0.2	3.1 ± 0.1	26
SN 2021ckj	0.143	Icn	*g*	−19.9 ± 0.1	3.0 ± 0.5	4.7 ± 0.2	26

Notes.
[a] Corrected for Galactic extinction, assuming zero host extinction in all cases except iPTF15ul.
[b] Rest frame, measured using the light curve that most closely matches rest-frame *g* band.
[c] Measurements are from Ho et al. (2020b).
[d] Rise times, fade times, and peak luminosities (with approximate *K*-correction) calculated as part of this paper. DES light curves were provided by M. Pursiainen.
[e] Luminosity and timescale measurements from Tables 1 and 4 of Drout et al. (2014), taking *K*-corrected values.
[f] Peak magnitudes from Table 4 of Hosseinzadeh et al. (2017). Rise and fade times calculated as part of this paper.
[g] Strict spectroscopic definition based on presence of H and He emission features in optical spectrum. RL: radio-loud.
[h] Timescales calculated using *g* band, as well as one ATLAS *o*-band upper limit prior to peak.
[i] Photometry from Chen et al. (2020), with a ZTF data point added.
[j] Radio-loud, spectra mostly featureless, with an unidentified very broad feature.

References. (1) Arcavi et al. 2016; (2) Ofek et al. 2010; (3) Drout et al. 2014; (4) Hosseinzadeh et al. 2017; (5) Pastorello et al. 2015; (6) Rest et al. 2018; (7) Pursiainen et al. 2018; (8) Whitesides et al. 2017; (9) Prentice et al. 2018; (10) Perley et al. 2019; (11) McBrien et al. 2019; (12) Prentice et al. 2020b; (13) Chen et al. 2020; (14) Kool et al. 2023, in preparation; (15) Jacobson-Galán et al. 2020; (16) Ofek et al. 2021; (17) Yao et al. 2022; (18) Matheson et al. 2000; (19) Tampo et al. 2020; (20) Perley et al. 2020; (21) de Vaucouleurs & Corwin 1985; (22) Perets et al. 2011; (23) Drout et al. 2013; (24) De et al. 2021; (25) Perley et al. 2022; (26) Pellegrino et al. 2022.

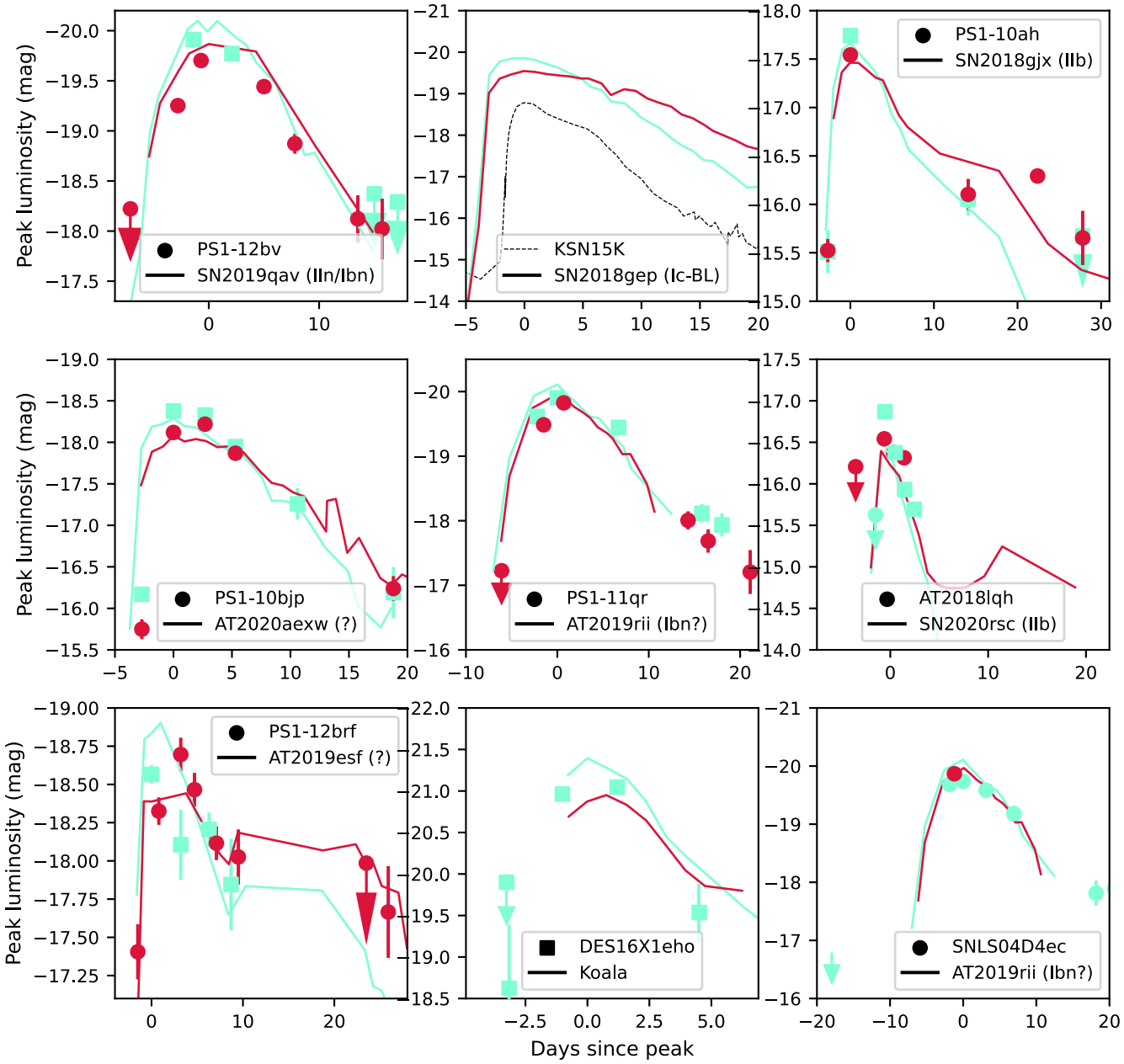

Figure 2. Light curves of FBOTs from the literature comparison sample, with the light curves of ZTF transients shown for comparison. The light curves of PS1 events are from Drout et al. (2014). The light curve of DES16X1eho is from M. Pursiainen (private communication). The light curve of KSN2015K is from Rest et al. (2018). The light curve of AT2018lqh is from Ofek et al. (2021). Literature light curves were taken to be as close to g (shown in cyan) and r (shown in red) band in the rest-frame as possible, for a more direct comparison with the ZTF light curves.

is significantly brighter than the peak of the radioactively powered light curve.

Several objects referred to as FBOTs in the literature do not meet our $t_{1/2} < 12$ day criterion: "Dougie" (Vinkó et al. 2015; Inserra 2019) and SN 2015U (Shivvers et al. 2016; Margutti et al. 2019) have too long of a duration. In addition, we do not include SN 2002bj (Poznanski et al. 2010; Margutti et al. 2019) because it did not have a sufficiently well-sampled peak; it was only detected on the decline. The events from Tanaka et al. (2016) were fast-rising, luminous, and blue (Fox & Smith 2019; Inserra 2019; Margutti et al. 2019) but were only detected during the rise phase—we therefore do not include them either. The remaining four events from Tampo et al. (2020) either do not have a spectroscopic redshift measurement or do not have a sufficiently well-sampled light curve for inclusion.

2.4. Optical Photometry

We performed forced photometry on P48 images for all events using the pipeline developed by F. Masci and R. Laher,[34] with the following additional steps:

1. We removed data taken in bad observing conditions by discarding observations with scisigpix, zpmaginpsci, or

[34] http://web.ipac.caltech.edu/staff/fmasci/ztf/forcedphot.pdf

Table 4
Optical Photometry of the ZTF Transients in Table 2

Name	Filter	JD	Flux (μJy)	eFlux (μJy)	Mag	eMag	Tel
…	…	…	…	…			
SN 2018bcc	*r*	2458224.93	12.36	4.55	20.51	99.00	P48
SN 2018bcc	*r*	2458224.95	15.16	6.21	20.17	99.00	P48
SN 2018bcc	*r*	2458226.84	103.84	3.71	18.86	0.04	P48
SN 2018bcc	*r*	2458226.86	110.24	3.51	18.79	0.03	P48
…	…	…	…	…			

Note. Nondetections are indicated with eMag = 99.

(This table is available in its entirety in machine-readable form.)

zpmaginpscirms exceeding five times the median of that value for the light curve.
2. We removed observations with flux values or χ^2 from the difference image recorded as NaN.
3. Following Yao et al. (2019), we grouped observations by `fcqfID`, a combination of field ID, CCD ID, quadrant ID, and filter ID.
4. For each group of `fcqfID`, we checked whether the stack of images used to construct a reference image could overlap with images of the target, by seeing whether the final reference image was within 15 days of the first ZTF alert issued. If so, we considered the data to be contaminated by the reference.
5. If the data were contaminated by the reference[35] (as defined in the previous bullet), we checked whether there were sufficient (at least 30) images to subtract a baseline flux value. We obtained images prior to 15 days before the first detection and after 100 days after the last detection. If there were at least 30 such images, we calculated the median flux value of all the baseline detections and subtracted that baseline value from the observations. If there were not sufficient baseline measurements, we excluded the observations.
6. Following the Masci & Laher documentation, we validated and rescaled the uncertainties on the flux values.
7. Following the Masci & Laher documentation, points with a signal-to-noise ratio (S/N) greater than 3 were regarded as detections and converted to magnitudes. Points with a lower S/N were regarded as upper limits and reported as 5σ.
8. We corrected for Milky Way extinction (Schlafly & Finkbeiner 2011) using the `extinction`package[36] with $R_V = 3.1$ and a Fitzpatrick (1999) extinction law.

When available, we added photometry obtained with other facilities: the IO:O on the Liverpool Telescope (LT; Steele et al. 2004), and the Rainbow Camera on the automated 60-inch telescope at Palomar Observatory (P60; Cenko et al. 2006). LT image reduction was provided by the basic IO:O pipeline. P60 and LT image subtraction was performed following Fremling et al. (2016), using PS1 images for *griz* and the Sloan Digital Sky Survey (SDSS) for *u* band. The final combined light curves are provided in Table 4. We discard points that are >20 days after the last alert or <10 days before the first alert. Then, we discard points >5 days after the last forced-photometry detection or <5 days before the first forced-photometry detection. The ZTF FBOT light curves with redshift measurements are shown in Figure 1; the remainder are shown in the Appendix B in Figure 15.

2.5. Optical Spectroscopy

Of the 38 ZTF transients in Table 2, 20 were classified using optical spectroscopy, and an additional 9 had redshift measurements but no classification. The redshift measurements and spectroscopic classifications are listed in Table 2.

Spectra of the transients and their host galaxies were obtained using a variety of telescopes: the Spectral Energy Distribution Machine (SEDM; Blagorodnova et al. 2018; Rigault et al. 2019), the Alhambra Faint Object Spectrograph and Camera (ALFOSC[37]) on the Nordic Optical Telescope (NOT; Djupvik & Andersen 2010), the Double Beam Spectrograph (DBSP; Oke & Gunn 1982) on the 200-inch Hale telescope at Palomar Observatory, the Spectrograph for the Rapid Acquisition of Transients (SPRAT; Piascik et al. 2014) on LT, the Low Resolution Imaging Spectrometer (LRIS; Oke et al. 1995) on the Keck I 10 m telescope, Binospec (Fabricant et al. 2019) on the MMT, the Optical System for Imaging and low-Intermediate-Resolution Integrated Spectroscopy (OSIRIS) on the Gran Telescopio Canarias (GTC; Cepa et al. 2000), the Gemini Multi-object Spectrograph (GMOS; Hook et al. 2004) on Gemini North, and the Device Optimized for the LOw RESolution (DOLORES) on the Telescopio Nazionale Galileo (TNG).

The SEDM pipeline is described in Rigault et al. (2019). NOT/ALFOSC spectra were reduced using `Foscgui`.[38] The SPRAT pipeline is based on the FrodoSpec pipeline (Barnsley et al. 2012), the P200/DBSP pipeline is described in Bellm & Sesar (2016), and the Keck/LRIS pipeline `Lpipe` is described in Perley (2019). Gemini, DOLORES, and GTC spectra were reduced using IRAF routines.[39] MMT/Binospec spectra were reduced using the standard pipeline (Kansky et al. 2019).

The spectra of several transients in Table 2 have already been published: SN 2018gep (Ho et al. 2019a; Pritchard et al. 2021), SN 2018gjx (Prentice et al. 2020a), AT2018lug (Ho et al. 2020b), SN 2019deh (Pellegrino et al. 2022), SN 2019dge (Yao et al. 2019), SN 2020oi (Horesh et al. 2020; Rho et al. 2021;

[35] In principle, a baseline should be subtracted for all events, but it has been found that this correction is very small, only <0.1% of transient flux values.
[36] https://github.com/kbarbary/extinction
[37] http://www.not.iac.es/instruments/alfosc/
[38] Foscgui is a graphic user interface aimed at extracting SN spectroscopy and photometry obtained with FOSC-like instruments. It was developed by E. Cappellaro. A package description can be found at http://sngroup.oapd.inaf.it/foscgui.html.
[39] IRAF is distributed by the National Optical Astronomy Observatories, which is operated by the Association of Universities for Research in Astronomy (AURA), Inc., under cooperative agreement with the National Science Foundation.

Gagliano et al. 2022), and AT2020xnd (Perley et al. 2021b). We provide a log of nonpublished spectroscopic observations (Appendix C, Table 11) and plot the spectroscopic evolution of each object (Appendix C, Figures 16, 17, 18, and 19).

2.6. UV and X-Ray Observations

TSix of the transients in Table 2 were observed with the UV/Optical Telescope (UVOT; Roming et al. 2005) and X-Ray Telescope (XRT; Burrows et al. 2005) on board the Neil Gehrels Swift Observatory (Gehrels et al. 2004). The UVOT and XRT observations of three of these transients have not yet been published and are provided in Tables 5 and 6.[40] We also provide UVOT/XRT data for the rapidly evolving Type Ibn SN 2019aajs that will be published as part of a ZTF Ibn sample paper (Kool et al. 2023, in preparation); SN 2019aajs did not pass our cuts because its rapidly evolving nature was only revealed by non-ZTF photometry. None of these objects were detected by XRT.

The brightness in the UVOT filters was measured with UVOT-specific tools in the HEAsoft version 6.26.1. Source counts were extracted from the images using a circular 3″-radius aperture. The background was estimated over a significantly larger area close to the SN position. The count rates were obtained from the images using the Swift tool `uvotsource`. They were converted to magnitudes using the UVOT photometric zero-points (Breeveld et al. 2011) and the UVOT calibration files from 2020 September. All magnitudes were transformed into the AB system using Breeveld et al. (2011). If the transient was affected by the host, we made use of archival UVOT observations or obtained templates after the SN faded. XRT data were reduced using the online tool[41] from the Swift team (Evans et al. 2007, 2009), using hydrogen column density values from Willingale et al. (2013).

2.7. Millimeter and Radio Observations

Four transients in Table 2 have published millimeter and/or radio observations (Ho et al. 2019a; Horesh et al. 2020; Ho et al. 2020b; Yao et al. 2020; Perley et al. 2021b). We observed an additional four objects with the IRAM Northern Extended Millimeter Array (NOEMA), the Submillimeter Array (SMA), and the Karl G. Jansky Very Large Array (VLA; Perley et al. 2011): three from Table 2 and one (SN 2019aajs) from Table 3. Observations are listed in Table 7; all resulted in nondetections.

We observed SN 2019aajs, SN 2019myn, SN 2019qav, and SN 2020rsc with the VLA. Data were calibrated using the automated pipeline available in the Common Astronomy Software Applications (CASA; McMullin et al. 2007), with additional flagging applied manually, and then imaged using the CLEAN algorithm (Högbom 1974).

SN 2019qav was observed with NOEMA under conditions of excellent atmospheric stability and transparency. Data calibration and analysis were done within the GILDAS[42] software package using CLIC for calibration and MAPPING for *uv*-plane analysis and imaging of the data. The absolute flux calibration accuracy is estimated to be better than 10%. The upper limit reported in Table 7 is from combining the two sidebands.

[40] The published events are SN 2019dge (Yao et al. 2020), SN 2018gep (Ho et al. 2019a), and SN 2020oi (Horesh et al. 2020).
[41] https://www.swift.ac.uk/user_objects/
[42] http://www.iram.fr/IRAMFR/GILDAS

Table 5
UVOT Photometry

Name (SN)	Date (JD)	Δt (days)	Filter	AB Mag
2019aajs	2458547.90	8.04	*UVW1*	18.57 ± 0.08
2019aajs	2458547.90	8.04	*U*	18.04 ± 0.09
2019aajs	2458547.90	8.04	*B*	17.93 ± 0.1
2019aajs	2458547.90	8.04	*UVW2*	19.05 ± 0.09
2019aajs	2458547.90	8.04	*V*	18.45 ± 0.23
2019aajs	2458547.90	8.04	*UVM2*	18.71 ± 0.07
2019aajs	2458551.15	11.29	*UVW1*	19.33 ± 0.11
2019aajs	2458551.15	11.29	*U*	18.60 ± 0.11
2019aajs	2458551.15	11.29	*B*	18.23 ± 0.12
2019aajs	2458551.16	11.29	*UVW2*	19.81 ± 0.11
2019aajs	2458551.16	11.30	*V*	18.37 ± 0.22
2019aajs	2458551.16	11.30	*UVM2*	19.54 ± 0.09
2019aajs	2458553.60	13.74	*UVW1*	19.38 ± 0.11
2019aajs	2458553.61	13.74	*U*	18.81 ± 0.12
2019aajs	2458553.61	13.75	*B*	18.81 ± 0.17
2019aajs	2458553.61	13.75	*UVW2*	20.24 ± 0.13
2019aajs	2458553.61	13.75	*V*	18.62 ± 0.25
2019aajs	2458553.61	13.75	*UVM2*	20.08 ± 0.12
2019aajs	2458569.30	29.44	*UVW1*	20.42 ± 0.19
2019aajs	2458569.30	29.44	*U*	19.81 ± 0.25
2019aajs	2458569.30	29.44	*B*	>20.0
2019aajs	2458569.30	29.44	*UVW2*	21.29 ± 0.24
2019aajs	2458569.30	29.44	*V*	>19.0
2019aajs	2458569.30	29.44	*UVM2*	21.06 ± 0.19
2019aajs	2458575.20	35.34	*UVW1*	20.80 ± 0.23
2019aajs	2458575.20	35.34	*U*	19.92 ± 0.22
2019aajs	2458575.20	35.34	*B*	>20.0
2019aajs	2458575.21	35.34	*UVW2*	21.30 ± 0.23
2019aajs	2458575.21	35.35	*V*	>19.0
2019aajs	2458575.21	35.35	*UVM2*	21.15 ± 0.2
2019deh	2458584.98	3.16	*UVW1*	17.55 ± 0.07
2019deh	2458584.98	3.16	*U*	17.28 ± 0.07
2019deh	2458584.98	3.16	*B*	17.60 ± 0.09
2019deh	2458584.98	3.17	*UVW2*	18.41 ± 0.08
2019deh	2458584.98	3.17	*V*	17.63 ± 0.15
2019deh	2458584.99	3.18	*UVM2*	18.01 ± 0.06
2019deh	2458585.68	3.87	*V*	17.55 ± 0.15
2019deh	2458585.69	3.87	*UVM2*	18.06 ± 0.07
2019deh	2458586.01	4.20	*UVW1*	17.62 ± 0.06
2019deh	2458586.01	4.20	*U*	17.27 ± 0.07
2019deh	2458586.01	4.20	*B*	17.34 ± 0.07
2019deh	2458586.02	4.20	*UVW2*	18.34 ± 0.08
2019qav	2458755.88	18.24	*UVW1*	21.59 ± 0.33
2019qav	2458755.88	18.24	*U*	21.06 ± 0.49
2019qav	2458755.88	18.24	*B*	21.64 ± 1.55
2019qav	2458755.88	18.24	*UVW2*	22.41 ± 0.33
2019qav	2458755.88	18.25	*V*	20.20 ± 0.78
2019qav	2458755.89	18.25	*UVM2*	22.22 ± 0.27
2020rsc	2459087.78	6.87	*UVW1*	>21.0
2020rsc	2459092.83	11.92	*U*	>20.0

Note. Epochs are given with respect to the first ZTF detection.

SN 2019aajs was observed with the SMA in the Extended configuration, using all eight antennas, under excellent conditions. Both receivers were tuned to local oscillator (LO) frequency of 225.5 GHz. Data were calibrated in IDL using the Millimeter Interferometer Reduction (MIR) package and then exported for additional analysis and imaging using the *Miriad* package (Sault et al. 1995). No obvious detection was seen in the dirty image, so no CLEANing was attempted.

In addition, we also queried ongoing radio surveys to determine whether any objects had been serendipitously

Table 6
Swift XRT Observations

Name (SN)	Date (JD)	Δt (days)	Count Rate (10^{-3} s^{-1})	Flux (10^{-13} erg cm^{-2} s^{-1})	Luminosity (10^{41} erg s^{-1})
2019aajs	2458547.90	8.04	<5.98	<2.24	<7.08
2019aajs	2458551.16	11.30	<4.52	<1.69	<5.36
2019aajs	2458553.61	13.75	<5.78	<2.16	<6.84
2019aajs	2458569.30	29.44	<5.39	<2.02	<6.39
2019aajs	2458575.21	35.34	<4.02	<1.50	<4.76
2019deh	2458584.99	3.17	<5.52	<1.92	<14.56
2019deh	2458586.01	4.20	<8.33	<2.89	<21.97
2019qav	2458755.88	18.25	<4.05	<1.37	<71.12
2020rsc	2459087.78	6.87	<7.08	<2.91	<7.00
2020rsc	2459092.83	11.92	<22.96	<9.43	<22.68

Note. Flux is given as unabsorbed flux. Conversions from count rate to flux assume a photon index $\Gamma = 2$, and values of $n_{\rm H}$ are taken from Willingale et al. (2013). Upper limits are 3σ. Epochs are given with respect to the first ZTF detection.

Table 7
Millimeter and Radio Observations

Object Name	Instrument	Program ID (PI)	Start Date (JD)	Δt (days)	ν (GHz)	f_ν (μJy)	L_ν (erg s^{-1} Hz^{-1})
SN 2019aajs	SMA	2018B-S047 (Ho)	2458564.19	24.33	230	<840	$<2.7 \times 10^{28}$
SN 2019aajs	VLA	18B-242 (Perley)	2458563.99	24.13	10	<15	$<4.8 \times 10^{26}$
SN 2019myn	VLA	18B-242 (Perley)	2458712.78	10.83	10	<16	$<4.3 \times 10^{27}$
SN 2019qav	NOEMA	S19BC (Ho)	2458753.20	15.56	90	<90	$<4.8 \times 10^{28}$
SN 2019qav	VLA	18B-242 (Perley)	2458765.42	27.78	10	<18	$<9.6 \times 10^{27}$
SN 2019qav	VLA	20A-374 (Ho)	2458922.12	184.48	10	<27	$<1.4 \times 10^{28}$
SN 2020rsc	VLA	20A-374 (Ho)	2459100.73	19.82	10	<15	$<3.6 \times 10^{26}$

Note. Upper limit given as 3× the image rms. Time given since first ZTF detection.

observed. To query the VLA Sky Survey (VLASS; Lacy et al. 2020), which observes at 3 GHz, we used the same approach as Ho et al. (2020b). Twenty-seven of the sources in our sample were observed by VLASS, but none are detected. Table 8 lists the sources, the date they were observed, and the associated rms values.

We also searched for radio counterparts in two surveys that are being undertaken with the Australian Square Kilometre Array Pathfinder (ASKAP; Hotan et al. 2021): the Rapid ASKAP Continuum Survey (RACS; McConnell et al. 2020) and phase one of the Variables And Slow Transients Pilot survey (VAST-P1; Murphy et al. 2013). RACS covers $\sim$35,000 deg^2 at 888 MHz to a typical rms noise of $\sim$250 μJy, while VAST-P1 targets 113 RACS fields with identical observing parameters, covering $\sim$5000 deg^2. There are 12 VAST epochs in total, with each field covered at least 5 times, and 7 on average. Nine of the sources in our sample were observed by RACS, and none had any associated radio emission. One source (AT 2020bdh) has additional coverage in VAST, and no emission is detected. Table 8 lists the observation details for sources in RACS and VAST.

2.8. Host Galaxy Photometry

We obtained host galaxy photometry for all transients with redshift measurements, provided in Table 9. We retrieved science-ready coadded images from the Galaxy Evolution Explorer (GALEX) general release 6/7 (Martin et al. 2005), the SDSS data release 9 (SDSS DR9; Ahn et al. 2012), PS1 Data Release 1 (Chambers et al. 2016), the Two Micron All Sky Survey (2MASS; Skrutskie et al. 2006), and preprocessed Wide-field Infrared Survey Explorer (WISE) images (Wright et al. 2010) from the unWISE archive (Lang 2014).[43] The unWISE images are based on the public WISE data and include images from the ongoing NEOWISE-Reactivation mission R3 (Mainzer et al. 2014; Meisner et al. 2017). The hosts of two objects (SN 2019php, AT 2020xnd) were too faint, so we retrieved deeper optical images from the DESI Legacy Imaging Surveys (LS; Dey et al. 2019) DR8. We measured the brightness of the host using LAMBDAR[44] (Lambda Adaptive Multi-Band Deblending Algorithm in R; Wright et al. 2016) and the methods described in Schulze et al. (2021). The 2MASS and unWISE photometries were converted from the Vega system to the AB system using the offsets reported by Blanton & Roweis (2007) and Cutri et al. (2013, their Table 3 in Section 4.4h).

In addition to this, we use the UVOT observations of SN 2018gep that were obtained after the transient faded. The brightness in the UVOT filters was measured with UVOT-specific tools in the HEAsoft[45] version 6.26.1. Source counts were extracted from the images using large apertures, to measure the total flux of the hosts. The background was estimated from regions close to the SN position. The count rates were obtained from the images using the Swift tool uvotsource. They were converted to magnitudes using the UVOT calibration file from 2020 September. All magnitudes were transformed into the AB system using Breeveld et al. (2011).

[43] http://unwise.me
[44] https://github.com/AngusWright/LAMBDAR
[45] https://heasarc.gsfc.nasa.gov/docs/software/heasoft

Table 8
Serendipitous Observations of the Transients in Table 2 by the VLA Sky Survey (3 GHz), the Rapid ASKAP Continuum Survey (888 MHz), and Phase One of the VAST Pilot Survey (888 MHz)

Name	Survey	MJD	Δt (days)	rms (μJy)
SN 2018bcc	RACS	58595	364	248
SN 2018gep	VLASS	58607	232	134
⋯	RACS	58595	221	535
SN 2018ghd	VLASS	59070	692	157
⋯	RACS	58598	221	353
SN 2018gjx	VLASS	58568	188	171
⋯	RACS	58595	216	257
AT 2018lug	VLASS	58551	176	133
⋯	RACS	58602	228	332
AT 2018lwd	VLASS	59074	755	141
AT 2019dcm	VLASS	58609	36	110
SN 2019deh	VLASS	58611	23	138
⋯	RACS	58598	11	248
SN 2019dge	VLASS	59072	488	156
AT 2019kyw	VLASS	59084	407	124
AT 2019lbr	VLASS	59090	414	217
SN 2019php	VLASS	59084	353	123
SN 2019qav	VLASS	59072	332	166
AT 2019qwx	VLASS	59091	336	161
SN 2019rta	VLASS	59135	375	175
AT 2019scr	VLASS	59067	303	162
SN 2019aajs	VLASS	59094	551	109
AT 2019aajt	VLASS	59111	525	140
⋯	RACS	58595	10	270
AT 2019aajv	VLASS	59074	353	143
SN 2020ano	VLASS	59063	191	139
AT 2020bdh	VAST	59090	215	380
SN 2020ikq	VLASS	59109	137	130
AT 2020kfw	VLASS	59093	101	130
AT 2020yqt	VLASS	59103	22	136
AT 2020aexw	VLASS	59072	20	141

Table 9
Photometry of the Host Galaxies

Object	Survey/Telescopes/Instrument	Filter	Brightness (mag)
SN 2018bcc	GALEX	FUV	20.00 ± 0.17
SN 2018bcc	GALEX	NUV	19.90 ± 0.06
SN 2018bcc	SDSS	g	18.53 ± 0.03
SN 2018bcc	SDSS	i	17.96 ± 0.09
SN 2018bcc	SDSS	r	18.24 ± 0.06
SN 2018bcc	SDSS	u	19.55 ± 0.11
SN 2018bcc	SDSS	z	17.93 ± 0.09
SN 2018bcc	WISE	W1	18.75 ± 0.14
SN 2018bcc	WISE	W2	19.52 ± 0.12

Note. All measurements are reported in the AB system and not corrected for reddening.

(This table is available in machine-readable form.)

3. Analysis of ZTF and Literature Transients

In Section 2, we selected transients with well-sampled light curves and durations of 1 day $< t_{1/2} <$ 12 days from both ZTF and the literature. In this section, we analyze the photometric and spectroscopic evolution of the transients from Section 2. We show that, based on timescales, colors, and luminosities, many of the ZTF transients can be securely classified as FBOTs.

3.1. Photometric Evolution

The photometric properties of FBOTs are summarized in Inserra (2019): peak magnitudes ranging from faint core-collapse SNe (CCSNe) to superluminous SNe, faster rise times than decline times, a wide range of decline timescales implying a variety of powering sources, and blue colors at peak light with reddening over time. The combination of a fast rise time and high peak luminosity rules out a radioactive decay power source in some cases; as summarized in Margutti et al. (2019), two popular alternatives are shock interaction with circumstellar matter and long-lived energy injection by a central engine.

The redshifts and peak magnitudes of the ZTF transients are reported in Tables 2 and 10, respectively. Of these objects, 11 had spectroscopic host galaxy redshifts measured prior to the discovery of the transient; for the remaining 18, the redshifts were measured via observations of the transient or the host galaxy after discovery.

We linearly interpolated the g- and r-band light curves in flux space to estimate a rise time $t_{1/2,\mathrm{rise}}$ and fade time $t_{1/2,\mathrm{fade}}$ from the half-maximum of the observed peak in each filter. We estimated error bars by performing a Monte Carlo with 600 realizations of the light curve. We estimated the absolute magnitude using Equation (1). The measured timescales are provided in Table 10.

Figure 3 shows the parameter space of duration and peak luminosity for the ZTF and literature FBOTs, color-coded by spectroscopic type (discussed in Section 3.2). The peak absolute magnitudes of the ZTF transients span $M = -16$ to -22 mag, similar to literature FBOT samples (Drout et al. 2014; Pursiainen et al. 2018) and similar to CCSNe. For reference, we also show the first peak of two double-peaked Type IIb SNe, SN 1993J and ZTF18aalrxas.

The top panel of Figure 4 compares the rise time to the fade time of the ZTF and literature FBOTs. Similar to literature FBOTs, the ZTF objects have a slower fade time than rise time and a wide range of fade times. The bottom panel of Figure 4 shows the rise time and peak luminosity of the ZTF and literature FBOTs.

We calculate the $g - r$ color on nights where observations were acquired in both filters (not correcting for host reddening). The peak-light colors are reported in Table 2. Similar to literature FBOTs, most transients are blue at maximum light and redden with time. There are exceptions, however, most notably the Type Ibn SNe and events with persistent interaction-dominated spectra (AT 2018cow and SN 2019qav). The evolution of $g - r$ color over time for each ZTF FBOT is shown in Figure 5.

3.2. Spectroscopic Classification of FBOTs

One of the challenges in spectroscopically classifying FBOTs is that the peak-light spectra often appear relatively featureless (Drout et al. 2014; Ho et al. 2019a, 2020b; Inserra 2019; Perley et al. 2019, 2021b; Karamehmetoglu et al. 2021). Some have weak features from interaction with circumstellar material (CSM), such as PTF09uj (Ofek et al. 2010), but such features have been difficult to discern in the low-S/N spectra often obtained for events at high redshift (Drout et al. 2014). Furthermore, by the phase at which SN features tend to become most distinguishable (2 weeks after peak light; Williamson et al. 2019), a rapidly fading event is

Table 10
Light-curve Properties of the ZTF Transients in Table 2

IAU Name	$m_{g,max}$ (mag)	$M_{g,max}$[d] (mag)	$t_{g,1/2,rise}$[c] (days)	$t_{g,1/2,fade}$ (days)	$m_{r,max}$ (mag)	$M_{r,max}$ (mag)	$t_{r,1/2,rise}$ (days)	$t_{r,1/2,fade}$ (days)
SN 2018bcc	17.46 ± 0.04	−19.82 ± 0.04	3.20 ± 0.08[a]	5.87 ± 0.37	17.74 ± 0.03	−19.55 ± 0.03	3.19 ± 0.09	7.84 ± 0.17
SN 2019dge	18.40 ± 0.02	−16.49 ± 0.02	1.98 ± 0.04	4.14 ± 0.17	18.57 ± 0.01	−16.31 ± 0.01	1.80 ± 0.07	7.68 ± 0.78
AT2018lwd	19.55 ± 0.05	⋯	2.02–3.0	4.27 ± 0.85	19.75 ± 0.07	⋯	2.06–3.01	6.29 ± 1.02
SN 2018gep	15.91 ± 0.00	−19.84 ± 0.00	3.27 ± 0.02	6.00 ± 0.17	16.23 ± 0.00	−19.51 ± 0.00	3.21 ± 0.05	10.90 ± 0.55
SN 2018ghd	18.49 ± 0.03	−17.73 ± 0.03	2.49 ± 0.10	7.03 ± 0.92	18.58 ± 0.04	−17.64 ± 0.04	2.26 ± 0.16	10.69 ± 4.12
AT2018lug	19.34 ± 0.05	−21.17 ± 0.05	1.12 ± 0.03	2.92 ± 0.14	19.82 ± 0.06	−20.69 ± 0.06	1.51–2.34	2.75 ± 0.34
SN 2018gjx	15.58 ± 0.01	−17.65 ± 0.01	2.32 ± 0.01	5.05 ± 0.08	15.78 ± 0.01	−17.45 ± 0.01	1.97–4.0	8.22 ± 0.19
AT2019dcm	19.09 ± 0.04	⋯	4.02–5.0	5.24 ± 0.31	19.17 ± 0.04	⋯	4.0–5.04	7.30 ± 0.40
SN 2019deh	17.22 ± 0.02	−19.73 ± 0.02	4.35 ± 0.07	6.33 ± 0.66	17.43 ± 0.05	−19.52 ± 0.05	5.00 ± 0.15	6.57 ± 0.42
AT2019aajt	19.49 ± 0.05	⋯	1.45 ± 0.04	4.22 ± 0.68	19.75 ± 0.05	⋯	1.36 ± 0.07	5.40 ± 0.47
AT2019aaju	19.41 ± 0.02	⋯	<3.1	8.80 ± 1.98	19.69 ± 0.06	⋯	<4.02	15.10 ± 5.15
AT2019esf	18.84 ± 0.03	−18.82 ± 0.03	2.31 ± 0.24	4.92 ± 0.59	19.20 ± 0.05	−18.47 ± 0.05	1.38 ± 0.09	21.97 ± 7.30
AT2019lbr	19.09 ± 0.04	⋯	2.25 ± 0.15	6.93 ± 0.79	19.35 ± 0.07	⋯	4.46 ± 0.20	6.53 ± 1.85
AT2019kyw	18.28 ± 0.04	−19.34 ± 0.04	4.35 ± 0.09	7.54 ± 0.47	18.48 ± 0.05	−19.14 ± 0.05	4.26 ± 0.14	>2.6
SN 2019myn	18.84 ± 0.02	−19.44 ± 0.02	3.48 ± 0.06	6.04 ± 0.84	18.91 ± 0.03	−19.37 ± 0.03	3.45 ± 0.15	5.45 ± 0.68
AT2019aajv	19.48 ± 0.03	⋯	0.80 ± 0.07	2.58 ± 0.50	19.86 ± 0.08	⋯	0.78 ± 0.12	1.77 ± 0.62
SN 2019php	18.68 ± 0.06	−19.29 ± 0.06	3.64 ± 0.11	4.71 ± 0.42	18.92 ± 0.04	−19.05 ± 0.04	3.21 ± 0.17	5.98 ± 0.28
SN 2019qav	18.99 ± 0.06	−19.96 ± 0.06	3.39 ± 0.28	7.38 ± 0.38	19.22 ± 0.10	−19.73 ± 0.10	4.51 ± 0.39	8.21 ± 0.42
AT2019qwx	19.03 ± 0.04	⋯	3.0–4.0	6.41 ± 0.51	19.29 ± 0.08	⋯	2.91–4.0	8.87 ± 2.83
SN 2019rii	18.75 ± 0.02	−20.00 ± 0.02	4.36 ± 0.16	5.61 ± 0.38	18.89 ± 0.03	−19.86 ± 0.03	3.96 ± 0.96	5.37 ± 1.61
SN 2019rta	17.88 ± 0.02	−17.53 ± 0.02	1.09 ± 0.03	5.74 ± 0.43	17.98 ± 0.03	−17.42 ± 0.03	1.20 ± 0.04	8.99 ± 1.09
AT2019scr	18.91 ± 0.05	⋯	<3.0	2.03 ± 0.24	19.48 ± 0.13	⋯	13.94–5.92	1.20 ± 1.51
AT2019van	18.54 ± 0.11	⋯	<3.31	4.75 ± 3.85	18.75 ± 0.18	⋯	1.36 ± 0.23	8.01 ± 1.93
SN 2020oi	14.06 ± 0.12	−17.75 ± 0.12	2.92 ± 0.33	8.05 ± 0.46	13.74 ± 0.12	−18.07 ± 0.12	6.07 ± 0.39	7.41 ± 0.76
SN 2020ano	19.06 ± 0.03	−16.65 ± 0.03	<3.9	1.46 ± 0.07	19.52 ± 0.06	−16.19 ± 0.06	<3.91	2.02 ± 0.79
AT2020bdh	18.60 ± 0.03	−17.72 ± 0.03	<2.87	7.50 ± 0.81	18.74 ± 0.06	−17.58 ± 0.06	<2.85	9.03 ± 2.21
AT2020bot	19.46 ± 0.04	−20.33 ± 0.04	1.19 ± 0.33	2.53 ± 0.14	19.54 ± 0.17	−20.26 ± 0.17	3.38 ± 0.30	0.55 ± 0.24
SN 2020ikq	18.27 ± 0.03	−18.10 ± 0.03	2.88–5.8	7.47 ± 1.11	18.51 ± 0.05	−17.86 ± 0.05	2.73–5.67	27.88 ± 2.11
SN 2020jmb	18.51 ± 0.03	−18.68 ± 0.03	3.61 ± 0.07	6.44 ± 0.37	18.78 ± 0.03	−18.41 ± 0.03	1.92–3.78	11.98 ± 1.87
SN 2020jji	19.50 ± 0.09	−16.64 ± 0.09	4.02 ± 0.56	6.76 ± 0.88	18.89 ± 0.17	−17.25 ± 0.17	3.13 ± 0.53	10.55 ± 1.00
AT2020mlq	19.71 ± 0.06	⋯	4.59 ± 0.42	6.44 ± 0.74	19.75 ± 0.06	⋯	3.71 ± 0.28	14.61 ± 2.53
AT2020kfw	19.05 ± 0.03	−18.07 ± 0.03	3.83 ± 0.12	4.54 ± 0.22	19.25 ± 0.04	−17.87 ± 0.04	3.67 ± 0.20	6.75 ± 0.33
AT2020aexw	19.39 ± 0.03	−18.21 ± 0.03	3.07 ± 0.04	7.44 ± 0.35	19.59 ± 0.05	−18.01 ± 0.05	2.87 ± 0.10	9.30 ± 0.95
AT2020yqt	19.17 ± 0.11	−19.08 ± 0.11	0.66 ± 0.07	3.38 ± 0.96	19.44 ± 0.09	−18.81 ± 0.09	1.35 ± 0.12	5.58 ± 0.83
SN 2020rsc	19.36 ± 0.07	−16.37 ± 0.07	1.62 ± 0.04	1.72 ± 0.28	19.36 ± 0.11	−16.36 ± 0.11	0.50 ± 0.27	2.75 ± 1.53
AT2020xnd	19.24 ± 0.04	−21.03 ± 0.04	1.6–4.81	2.39 ± 0.30	19.54 ± 0.06	−20.73 ± 0.06	0.88–3.26	3.60 ± 0.18
SN 2020vyv	18.68 ± 0.03	−18.55 ± 0.03	1.49 ± 0.07	4.13 ± 0.31	18.98 ± 0.05	−18.25 ± 0.05	2.08 ± 0.13	8.21 ± 1.24
SN 2020xlt	19.59 ± 0.04	−16.58 ± 0.04	<0.91	3.52 ± 0.31	19.61 ± 0.07	−16.56 ± 0.07	2.06–2.87	4.58 ± 0.39

Notes.
[a] Based on *r*-band points.
[b] A range indicates a rise or fade that was not resolved by detections.
[c] Times are given in the rest frame.
[d] Peak absolute magnitudes have an approximate *K*-correction applied.

difficult to observe. The advantage of a high-cadence and shallow survey like ZTF is that objects are discovered young and relatively nearby, respectively: for several of the ZTF FBOTs we were able to obtain spectra within 2–3 days of peak light with sufficiently high S/N to discern even weak CSM interaction features, as well as late-time spectra that enabled spectroscopic classifications. For our analysis here, we only consider spectra obtained with instruments other than the SEDM, due to its low resolution ($R \sim 100$).

The most common behavior at peak light is a spectrum dominated by a blue continuum, as has been found for previous FBOT samples (Drout et al. 2014; Inserra 2019). Some events show narrow (width of hundreds of kilometers per second) emission features of helium and hydrogen (Figure 6), while others show entirely featureless spectra or spectra with very broad absorption features ($v > 0.1c$; Figure 7). The events with very broad features or entirely featureless spectra include the most luminous objects in the ZTF sample (AT 2020xnd, SN 2018gep, AT 2018lug), suggesting that high velocities may link the high luminosity of the light curve and the broad features of the spectra.

SN 2019rii warrants particular note: it has He I $\lambda\lambda$3389, 4471, and 5876 (though neither λ6678 nor λ7065), with weak narrow emission at $v = 0$ and narrow absorption at $v = 900\,\mathrm{km\,s^{-1}}$ for λ5876 and $600\,\mathrm{km\,s^{-1}}$ for $\lambda\lambda$4471 and 3889. We tentatively classify it as a Type Ibn on the basis of this spectrum (and the late-time spectrum of the transient is dominated by the host galaxy), but note that this classification is not fully secure. We include this object in Figure 6, but note that it is not strictly an FBOT because its peak-light color is $g - r = -0.1$ mag.

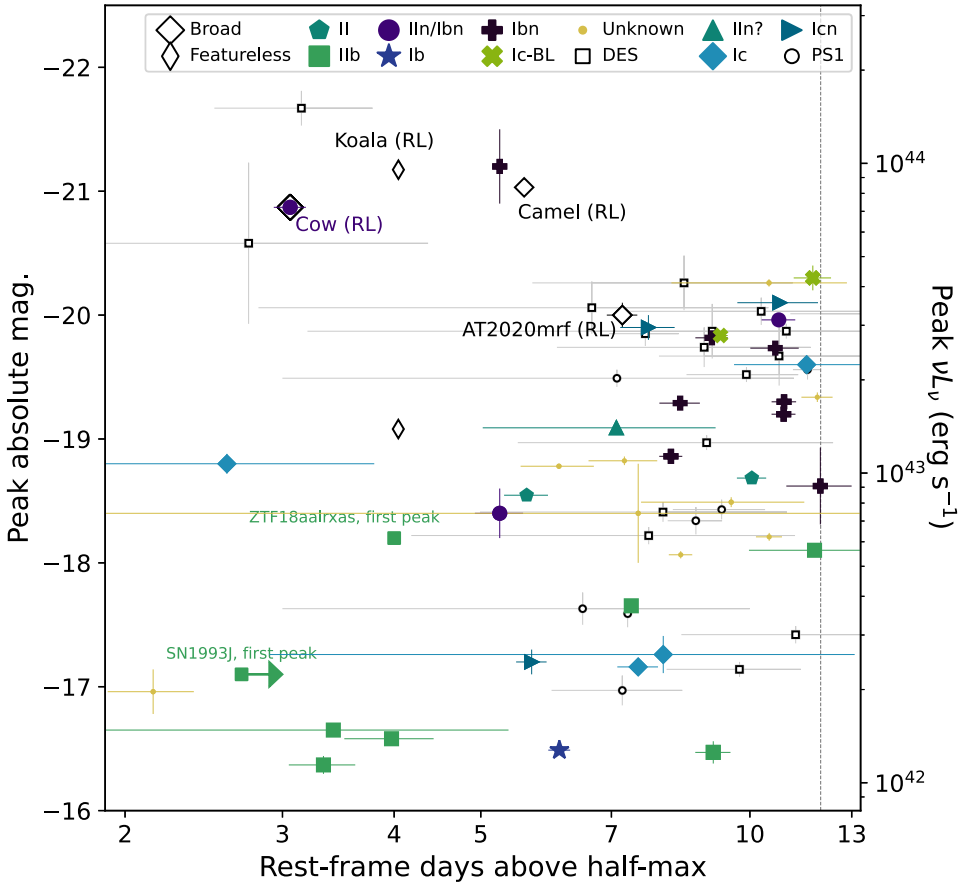

Figure 3. The luminosity–duration parameter space of ZTF and literature FBOTs. Measurements are in g band and rest frame when possible. The vertical line indicates the duration cut of $t_{1/2} = 12$ days that is commonly used to define FBOTs in the literature (Drout et al. 2014; Inserra 2019). Events with luminous radio emission (RL)—Cow/AT2018cow, Koala/AT2018lug, Camel/AT2020xnd, AT2020mrf—have particularly fast and luminous optical light curves and predominantly featureless spectra at peak light (with a very broad $v > 0.1c$ unidentified feature in some cases). Most spectroscopically classified FBOTs are members of established CCSN types. For clarity we do not plot SN 2019ehk because the peak luminosity is significantly fainter (−14.7 mag).

SN 2020vyv has a TNS classification of Type II SN based on a tentative broad Hα feature in the peak-light spectrum. As there is no definitive late-time spectrum, we list the classification as II? in Table 2. SN 2020rsc had a peak-light spectrum that already showed prominent P Cygni features, enabling the Type IIb classification.

Due to a lack of spectra obtained after peak, previous FBOT samples have not been able to conclude whether the objects were hydrogen-rich or hydrogen-poor (Drout et al. 2014; Pursiainen et al. 2018). By 1–3 weeks after peak light the spectra of most of the ZTF FBOTs began to exhibit P Cygni features from optically thin ejecta, enabling their spectroscopic classification as SNe. The compositions range from H-rich (Type II/IIb), to H-poor (Type Ib), to fully stripped (Type Ic-BL).

The subluminous FBOTs ($M > -18$ mag) most commonly evolve into Type II, Type IIb, and Type Ib SNe, as shown in Figure 8. We note that the distinction between these classes can be subtle when spectroscopic coverage is limited. For example, SN 2020jji and SN 2020jmb have spectra at 2 weeks after peak light that resemble both Type IIP and Type IIb objects, and we use a Type II classification to be more generic. The full sample of short-duration Type II and Type IIb events will be presented and modeled in a separate paper by Fremling et al.

The luminous ($M < -18$ mag) and somewhat longer duration (>6 days) FBOTs most commonly evolve into Type Ibn SNe. We show the Type Ibn post-peak spectra in Figure 9, together with spectra of the literature comparison sample objects that were also classified as Type Ibn (Pastorello et al. 2015; Hosseinzadeh et al. 2017). Type Ibn SNe are named for the strong and relatively narrow (∼2000 km s^{-1}) He I emission lines in their early spectra (Pastorello et al. 2008; Gal-Yam 2017; Smith et al. 2017). The detailed properties of the Type Ibn SNe observed in ZTF will be presented in a separate paper by Kool et al.

Finally, some events have post-peak spectra that remained dominated by a blue continuum with narrow emission lines, with no nebular emission from optically thin inner ejecta. In particular, SN 2019qav evolved in a similar fashion to the Type IIn/Ibn transition object SN 2005la (Pastorello et al. 2008; Smith et al. 2012), as we show in Figure 10. Similarly, AT 2018cow had He II emission lines that emerged after 1 week and Balmer emission lines that emerged 1 week after that but never developed P Cygni features. The only transient in the PS1 sample with a post-peak spectrum, PS1-12bb (+33 days), also had a persistently continuum-dominated spectrum, although weak features would not have been detectable at this low S/N. Drout et al. (2014) noted that a persistent continuum was unusual for rapidly declining SNe. Both SN 2019qav and PS1-12bb were slightly redder than the $g - r \leqslant -0.2$ mag of FBOTs.

In conclusion, a picture is emerging in which the FBOT spectroscopic classification is strongly correlated with its luminosity, with interacting SNe dominating the most luminous ($M < -18$ mag) events and Type IIb and Type Ib dominating the

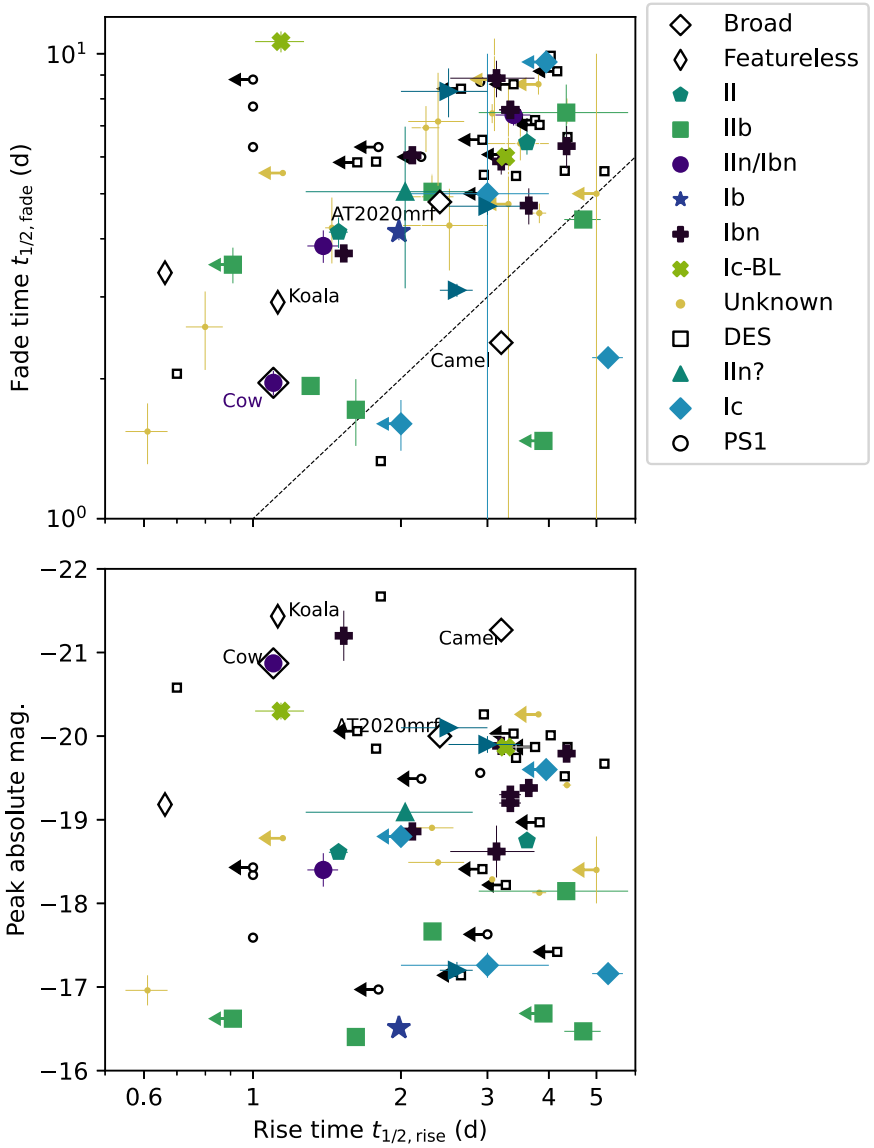

Figure 4. Top panel: the rise and fade times of ZTF FBOTs and well-observed FBOTs in the literature. The dashed line in the top panel indicates equal rise and fade times. Both ZTF FBOTs and unclassified FBOTs in the literature typically have longer fade times than rise times. Bottom panel: rise time vs. peak luminosity of ZTF and literature FBOTs. Timescales and luminosities are measured in g band, in the rest frame, from half-peak to peak. Radio-loud FBOTs (Cow/AT2018cow, Koala/AT2018lug, Camel/AT2020xnd, and AT2020mrf) have particularly high peak luminosities.

subluminous ($M > -18$ mag) events. Some of the most luminous events have broad absorption features from high velocities, suggesting that the high velocities are related to the high luminosity, and perhaps also to the presence of luminous radio emission.

3.3. X-Ray and Radio Emission

There is considerable interest in understanding to what extent AT 2018cow is part of a continuum that extends into other parts of the fast-transient parameter space and to what extent it is a distinct class. In the literature AT 2018cow is often described as an FBOT, but it has not been clear to what extent its properties are representative of the parameter space in Figure 3. In this section we discuss to what extent the luminous X-ray, millimeter, and radio emission of AT2018cow can be ruled out in other parts of the parameter space of Figure 3.

In Figure 11 we show the millimeter and radio upper limits presented in Section 2.7 compared to the light curve of AT 2018cow. The only events with similar millimeter and radio behavior—AT 2020xnd and AT 2018lug—also have very similar optical light curves to AT 2018cow. SN 2019qav (Type IIn/Ibn) also had a high luminosity and spectra persistently dominated by interaction, yet X-ray, millimeter, and radio observations rule out emission similar to that of AT 2018cow. SN 2020rsc (Type IIb) had a light curve similar to AT 2018cow in its duration (albeit significantly less luminous), yet we can also rule out X-ray/millimeter/radio emission similar to AT 2018cow by orders of magnitude. Finally, SN 2019deh was a rapidly evolving and luminous Type Ibn SN that remained persistently blue, with a relatively constant effective temperature—millimeter and radio observations also resulted in nondetections, ruling out emission similar to AT 2018cow by orders of magnitude.

To our knowledge, only two Type Ibn SNe have X-ray detections, and both were nearby: SN 2006jc (Immler et al. 2008) and SN 2010al (Ofek et al. 2013). Although these two events had a similar late-time luminosity to that of

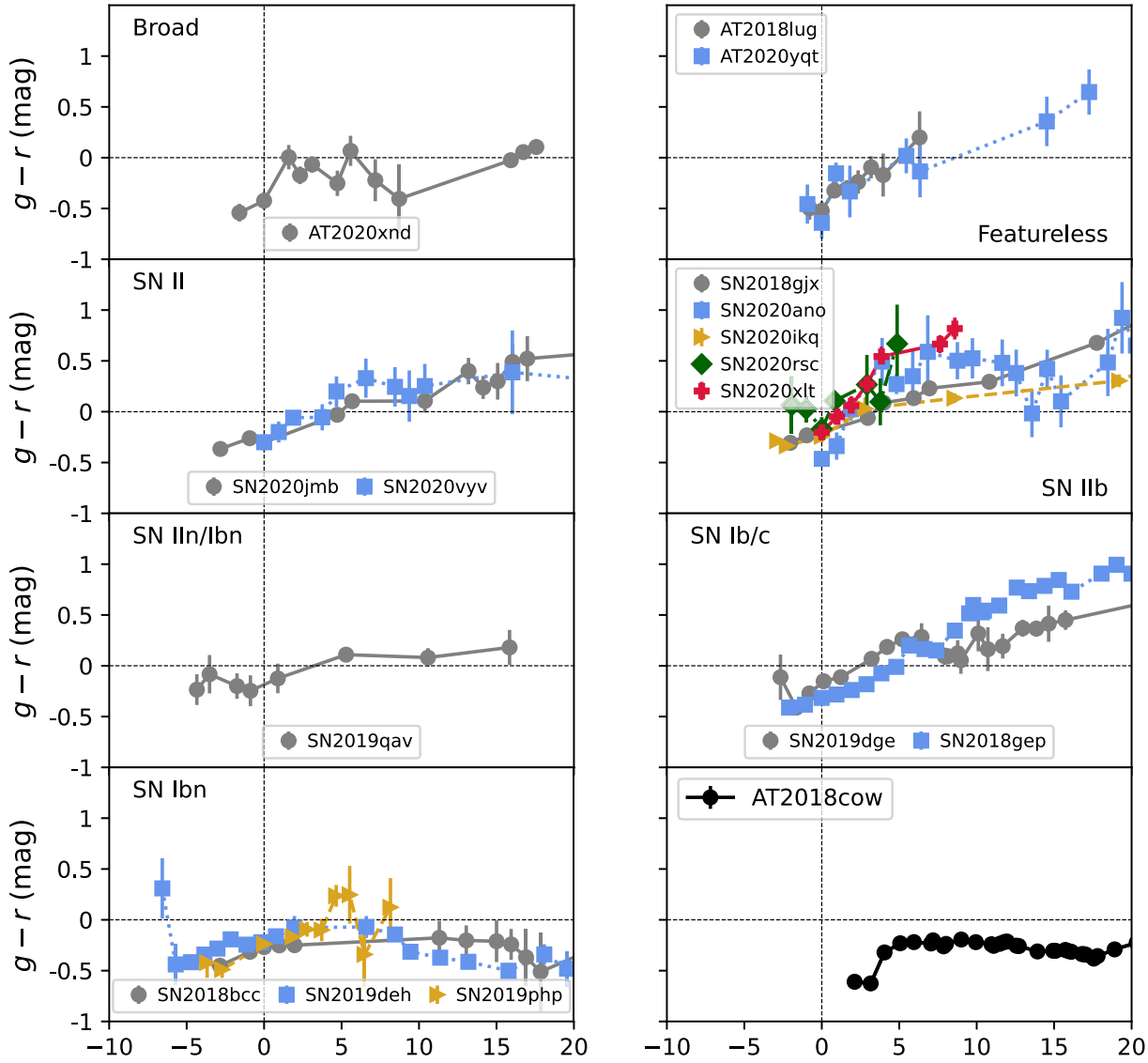

Figure 5. Color evolution of ZTF FBOTs, with AT2018cow shown on the lower right for comparison. Unlike AT2018cow, most events redden after peak, with the exception of the Type Ibn SNe and potentially the radio-loud event AT 2020xnd.

AT 2018cow ($\sim 10^{40}$ erg s^{-1}), the early-time luminosity was orders of magnitude smaller. SN 2006jc took 100 days to rise to peak luminosity in X-rays, whereas AT 2018cow rose to peak light in X-rays within 3 days.

Hence, although we cannot rule out AT2018cow-like X-ray, millimeter, and radio emission for all of the events in our sample, it appears that neither a high luminosity, nor persistent interaction, nor a constant blue color is predictive of this behavior on its own. Such emission is only seen in events that also have a rapidly fading light curve. This supports the idea that AT2018cow-like FBOTs are a distinct class and that a single term is too vague for a part of parameter space that includes events as diverse as AT 2018cow, subluminous Type IIb SNe with shock-cooling peaks, and the well-established class of Type Ibn SNe.

3.4. Host Galaxies

In this section we present the host galaxy properties of the objects in our sample. In the Appendix we describe the modeling procedure and provide a table of the fit parameters (Table 12) and the host properties (Table 13).

Figure 12 shows the B-band luminosities of the hosts of the ZTF FBOTs, which span $M_B \approx -12.7$ to -21.8 mag. The distribution is similar to that of regular CCSNe, which we illustrate with contours encircling 68%, 90%, and 95% of the PTF+iPTF CCSN sample (Schulze et al. 2021), which includes 888 objects spanning all major CCSN classes.

One noteworthy object is the Type Ibn SN 2019php. We detect a $g \sim 25.5 \pm 0.3$ mag object approximately $1''$ southeast of the transient position in Legacy Survey images. If this is indeed the host, its luminosity is $M_B \sim -12.7$ mag. Such faint galaxies are very rare but not unheard of for CCSN host galaxies (e.g., Gutiérrez et al. 2018; Schulze et al. 2021). If the marginally detected object is an image artifact, the SN 2019php host galaxy would be even fainter and pushing into the regime of the faintest and least massive star-forming galaxies (McConnachie 2012). It could also point to an extremely low surface brightness galaxy (e.g., van Dokkum et al. 2015).

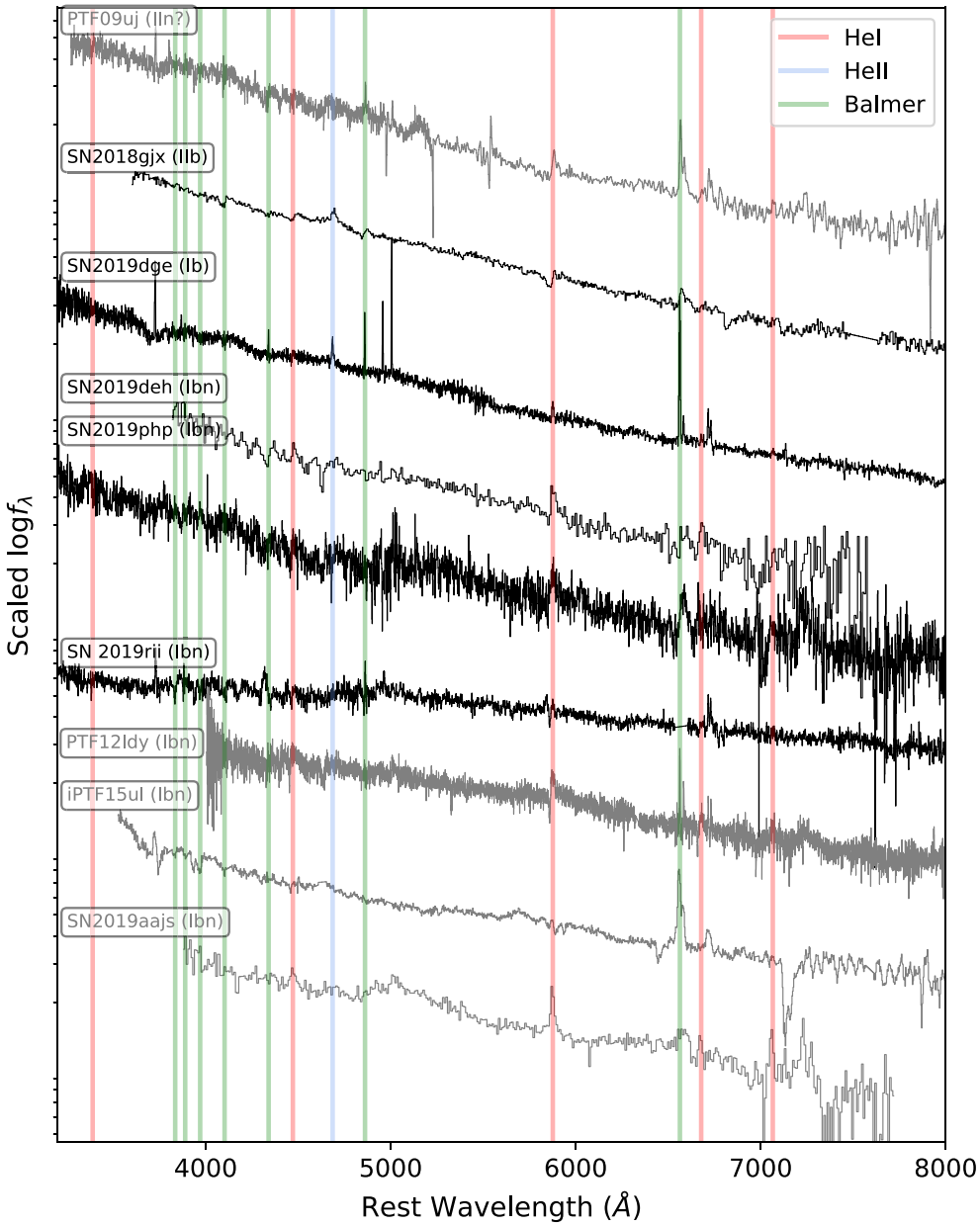

Figure 6. Peak-light spectra of well-observed FBOTs that show narrow emission features. ZTF FBOTs are shown in black. The spectrum of SN 2018gjx was downloaded from the TNS (Gromadzki et al. 2018). Comparison sample FBOTs are shown in gray. The comparison sample spectra were initially presented in Ofek et al. (2010) and Hosseinzadeh et al. (2017), and the spectrum of SN 2019dge was initially presented in Yao et al. (2020).

Figure 13 shows the host properties in the mass−star formation rate (SFR) plane. The hosts are located along the so-called main sequence of star-forming galaxies (indicated by the gray shaded region; based on Equation (5) in Elbaz et al. 2007). A small minority of objects occurred in galaxies that lie above the galaxy main sequence and are experiencing a starburst. This phenomenon is not exclusive to a particular spectroscopic subtype. Our results are similar to those of Wiseman et al. (2020), who studied the hosts of rapidly evolving transients between $z = 0.2$ and $z = 0.85$. As in Figure 12, we overlay the 68%, 90%, and 95% contours of the PTF CCSN host sample. The hosts of regular CCSNe occupy the same parameter space, including the starburst regime (e.g., Taggart & Perley 2021).

An outstanding object is AT 2020bot. It exploded ≈10 kpc from the center of an early-type galaxy. The GalaxyZoo Project classified the host morphology as elliptical (Lintott et al. 2008, 2011). The SDSS spectrum shows no emission lines. Such an environment is extreme for any type of transient originating from the explosion of a massive star, but it is not unheard of for CCSNe (Sanders et al. 2013; Hosseinzadeh et al. 2019; Irani et al. 2019, 2022). We discuss the implications in Section 5.

4. The Rate of AT2018cow-like Transients

The transient AT2018cow is widely referred to in the literature as an FBOT (e.g., Margutti et al. 2019), and FBOTs have been reported to have a volumetric rate of 1% of the CCSN rate (Drout et al. 2014; Pursiainen et al. 2018). However, our work shows that transients with similar properties to AT2018cow (X-ray, radio, unusual optical spectra, and rapidly fading optical light curves) are only a small subset of

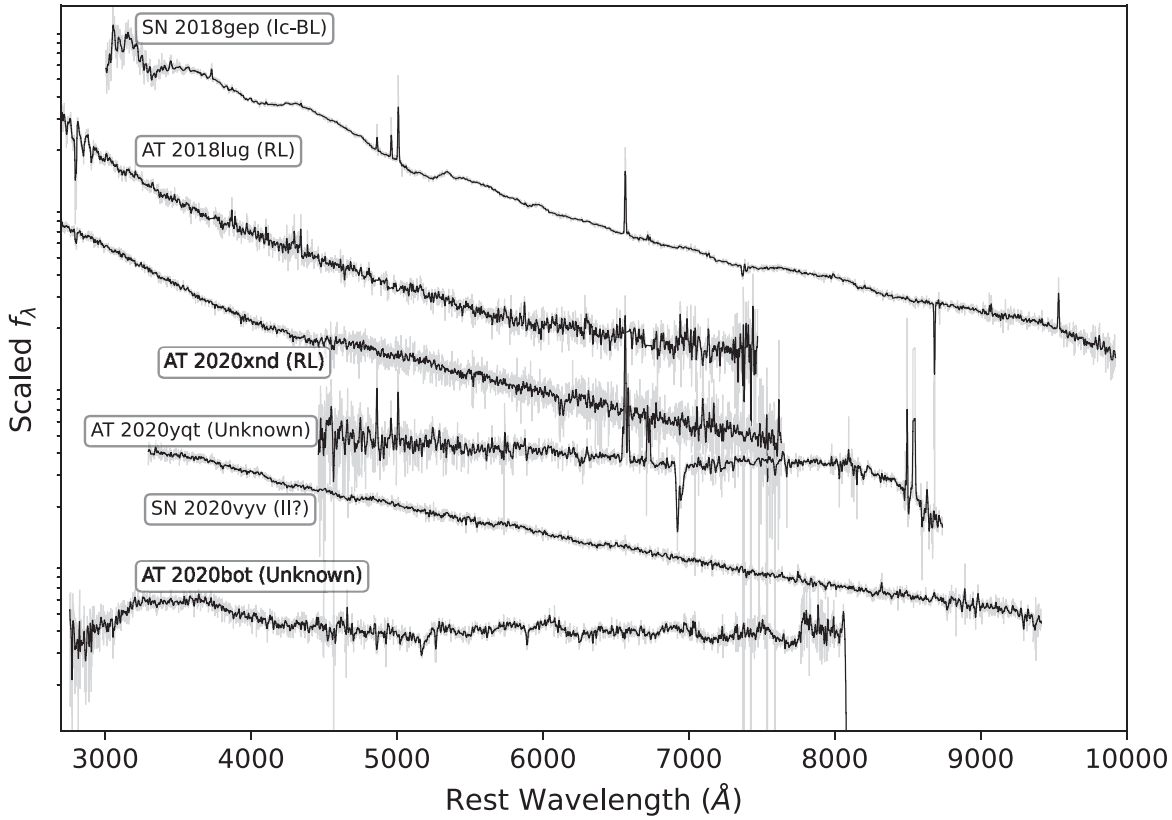

Figure 7. Peak-light spectra of well-observed ZTF FBOTs that are entirely featureless or show broad absorption features. The spectra of SN 2018gep, AT 2018lug, and AT 2020xnd were originally published in Ho et al. (2019a, 2020b) and Perley et al. (2021b), and the spectrum of SN 2020vyv was downloaded from the TNS (Siebert et al. 2020). AT 2020bot is not strictly an "FBOT" because its peak-light color is $g - r = -0.1$ mag.

FBOTs,[46] motivating a revised estimate of their rate, which is in turn an important clue to their progenitor system.

We estimate the rate of AT2018cow-like transients using two systematic ZTF classification efforts: the volume-limited survey (the Census of the Local Universe, or CLU; De et al. 2020) and the magnitude-limited survey (the Bright Transient Survey, or BTS; Fremling et al. 2020; Perley et al. 2020). CLU and BTS used different selection criteria from the search we performed in this paper, and both samples include AT2018cow.

CLU aims to classify all transients down to $r = 20.0$ mag within 200 Mpc, using data from all survey streams. Over the timescale of our search, CLU classified 429 CCSNe brighter than $M = -16$ mag within 150 Mpc. At this distance AT 2018cow would peak at 16 mag and remain over the $r = 20$ mag threshold for over 2 weeks, so CLU can be expected to be reasonably complete. The primary limitation is the use of a galaxy redshift catalog (Cook et al. 2019), so we caution that our rate is only valid for the types of galaxies well represented in this catalog. Given the detection of a single AT 2018cow-like object (AT 2018cow itself), and accounting for the fact that half of CCSNe are fainter than $M = -16$ mag (Li et al. 2011; Perley et al. 2020), we find a rate of 0.1% the CCSN rate, with a 95% confidence interval from binomial counting statistics of [0.003%, 0.6%]. In absolute terms, this corresponds to a volumetric rate of 70 yr^{-1} Gpc^{-3}.

We can also estimate the rate using the BTS (Fremling et al. 2020; Perley et al. 2020), which aims to classify all transients down to $r = 18.5$ mag in the public survey (15,000 deg^2). We consider a volume of 250 Mpc, out to which BTS should be quite complete for events like AT 2018cow. Using the BTS Survey Explorer,[47] and applying a quality cut, we find that there were 68 CCSNe classified in this volume brighter than $M = -18.5$ mag, as well as AT 2018cow itself. Correcting for the SN luminosity function (1%–3% are brighter than this; Perley et al. 2020), we find a rate of 0.01% with a 95% confidence interval of [0.0004%, 0.08%].

To be conservative, we take the lower limit from the BTS and the upper limit from CLU and estimate that the rate is 0.0004%–0.6% of the local CCSN rate, or 0.3–420 yr^{-1} Gpc^{-3}. Our rate estimate is consistent with the finding of Coppejans et al. (2020), using data from the Palomar Transient Factory, that the rate of events with light curves identical to AT 2018cow is <0.4% of the local CC SN rate.

Finally, although a measurement of the overall "FBOT" volumetric rate does not have a straightforward interpretation owing to their heterogeneity (Figure 3), we estimate the rate of 1 day $< t_{1/2} <$ 12 day transients in ZTF as a comparison to the high rates quoted in the literature (1% in Pursiainen et al. 2018; 4%–7% in Drout et al. 2014). For the faintest object in our sample ($M = -16.3$ mag), we conservatively estimate that the BTS would be complete out to 70 Mpc; at this distance, the source would be brighter than the BTS threshold for 1 week. There have been 55 CCSNe classified in this volume brighter than −16.3 mag, of which only SN 2018gjx would be called an FBOT (Table 2), and

[46] The term "luminous FBOT" (LFBOT) has recently been adopted for such events (e.g., Metzger 2022). In this paper we use "AT2018cow-like."

[47] https://sites.astro.caltech.edu/ztf/bts/explorer.php

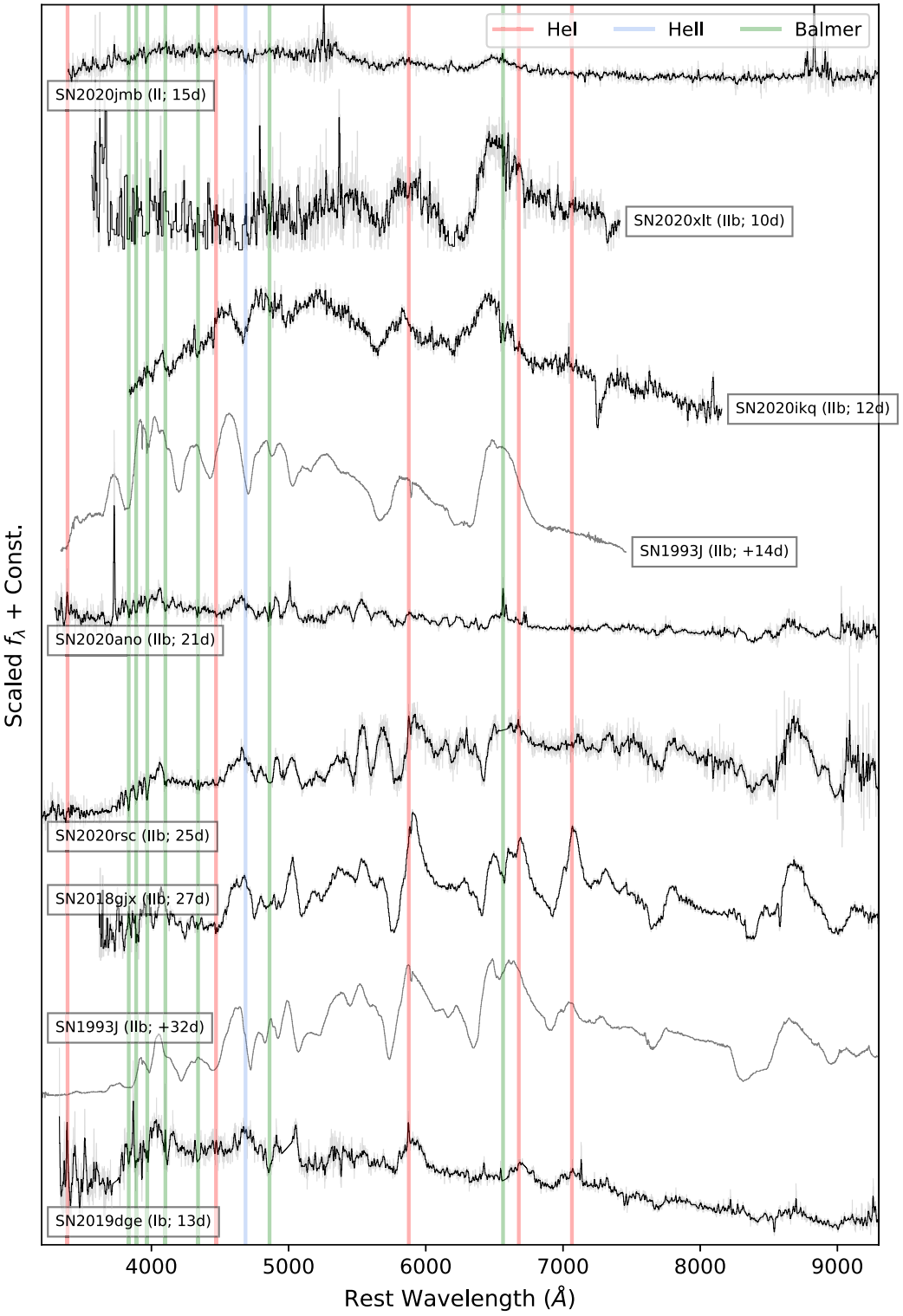

Figure 8. Post-peak spectra of the ZTF FBOTs classified as Type IIb or Type Ib SNe based on their H and He P Cygni features at late times. For comparison we show spectra of the Type IIb SN 1993J, obtained from WISeREP and originally from the UCB SN database (Silverman et al. 2012). The phase of the SN 1993J spectra is given with respect to the peak of the first (shock-cooling) peak, 1993 March 30. For the ZTF objects, epochs are given with respect to the maximum of the *g*-band light curve; raw spectra are shown in light gray, with smoothed spectra overlaid in black; and in some cases we have clipped host emission lines for clarity.

additionally AT 2018cow itself. Correcting for the SN luminosity function (50% are more luminous than −16.3 mag), we find a rate of 7% with a 95% confidence interval of [0.9%, 30%]. Our lower limit of ≈1% is consistent with previous results in the literature (Pursiainen et al. 2018; Drout et al. 2014) and is dominated by events at lower luminosities (predominantly Type IIb SNe).

5. Discussion

We have shown that "FBOTs," a class previously defined primarily by photometric properties, have multiple spectroscopic subtypes, summarized in Figure 14. In this section we discuss the implications of our findings for the progenitors and the powering mechanism for the optical light curves and make

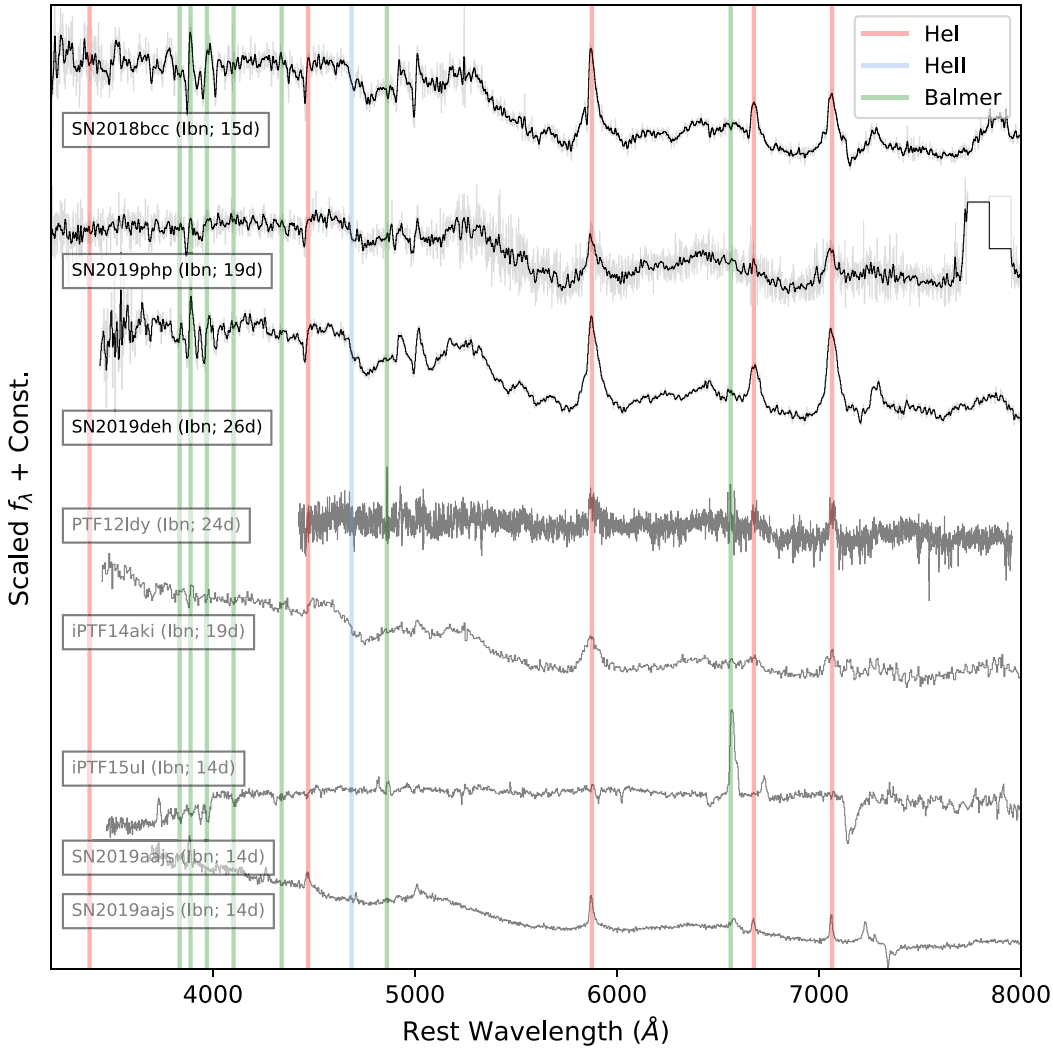

Figure 9. Post-peak spectra of well-observed ZTF FBOTs classified as Type Ibn based on their He P Cygni features at late times, together with the post-peak spectra of FBOTs classified as Type Ibn in the literature. Spectra of PTF 12ldy and iPTF 15ul were obtained from WISeREP and are originally from Hosseinzadeh et al. (2017).

suggestions for how to more effectively select rare exotic objects such as AT2018cow.

First, FBOT progenitors appear to be predominantly massive-star explosions, and most events fall into established SN spectroscopic classes. At the subluminous ($M > -18.5$ mag) end, the most common subtype is Type IIb SNe. The light-curve durations, luminosities, and colors are reminiscent of the shock-cooling peaks seen in double-peaked Type IIb SNe such as SN 1993J (Schmidt et al. 1993) and ZTF18aalrxas (Fremling et al. 2019), which are included in Figure 3. In fact, we see a distinct second peak in SN 2020ano, which is significantly less luminous than the first peak. By analogy, it seems reasonable to conclude that shock-cooling emission plays a key role in powering our events. We suggest that Type IIb SNe simply have a range of relative brightness of the shock-cooling peak and nickel-powered peak, and some FBOTs reflect cases where the former is significantly brighter than the latter. This could arise from material at particularly large radii (CSM), events with very low nickel masses, or both; we defer modeling of the Type IIb FBOTs to a forthcoming paper by Fremling et al.

FBOTs with peak luminosities between $M_g = -20$ mag and $M_g = -18.5$ mag are dominated by interacting SNe, particularly those of Type Ibn. The connection of Type Ibn SNe to fast-evolving transients has already been pointed out (Fox & Smith 2019; Karamehmetoglu et al. 2021; Xiang et al. 2021), and as discussed in Karamehmetoglu et al. (2021), the rise time of most Type Ibn SNe has not been well sampled, so their true duration is relatively uncertain. Type Ibn light curves are generally thought to be powered by CSM interaction, with material much more extended than that involved in the shock-cooling peaks we have discussed previously.

At the highest luminosities ($M \lesssim -20$ mag) lie the radio-loud events AT 2018cow (the Cow), AT 2020xnd (the Camel), and AT 2018lug (the Koala), as well as the unusual Type Ic-BL SNe SN 2018gep and iPTF16asu. In the shock interaction picture, a fast rise time and high peak luminosity arise from a fast shock speed—i.e., a significant amount of energy is coupled to ejecta traveling at high velocities. This is likely a distinguishing characteristic of these events. Indeed, these events are the only objects that show very broad absorption features in their optical spectra.

However, despite sharing several characteristics with other events—a high luminosity, a fast rise, persistent interaction, and

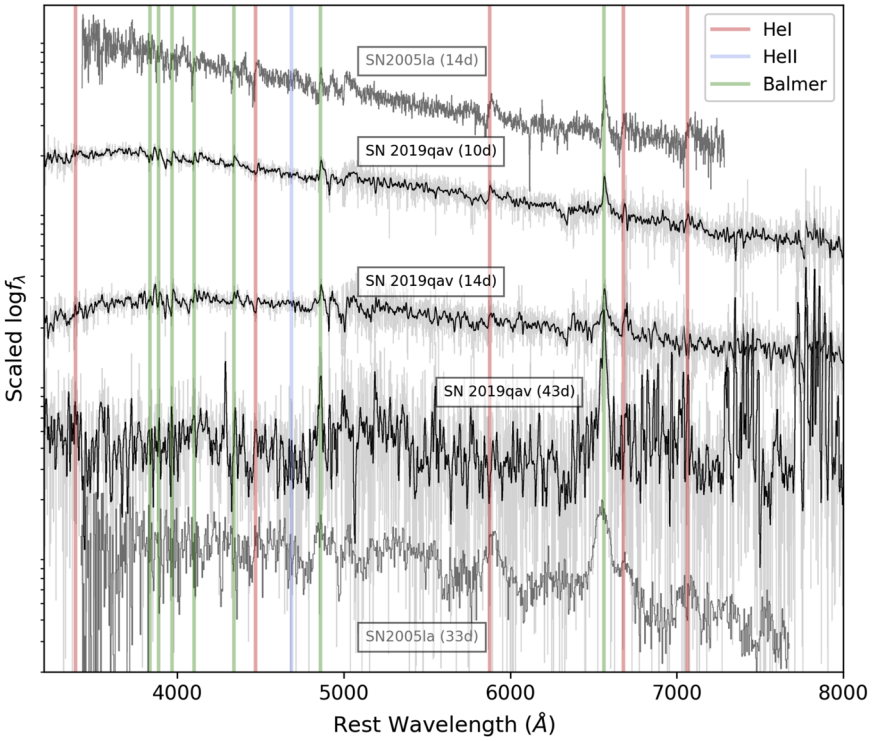

Figure 10. Post-peak evolution of SN 2019qav, which we classify as a Type IIn/Ibn transitional object owing to its similarity to SN 2005la. Spectra of SN 2005la were obtained from WiseREP and are originally from Modjaz et al. (2014) and Pastorello et al. (2008).

blue colors—it appears that only the AT2018cow-like events, the fastest-fading, most luminous transients, are accompanied by luminous millimeter, X-ray, and radio emission. One possible explanation is that these events are engine powered, while established classes of interacting SNe (like Type Ibn SNe) are not. A central engine has been suggested to power AT2018cow-like events on the basis of the luminous long-lived X-ray emission, which is in excess of what would be expected from circumstellar interaction (Ho et al. 2019b; Margutti et al. 2019; Coppejans et al. 2020; Bright et al. 2022; Ho et al. 2022a). The fact that they also stand out in duration−luminosity parameter space supports a distinct origin for the AT2018cow-like events. It is not yet clear whether they represent a distinct progenitor entirely.

It has been suggested that FBOTs as a whole have a high rate, 1% of the CCSN rate (Drout et al. 2014; Pursiainen et al. 2018). Clearly, this rate refers to multiple classes of objects, many of which are not distinct classes but rather a subset of broader classes (Type IIb SNe, Type Ibn SNe). Our work suggests that events similar to AT2018cow—the most luminous, fastest transients—are very rare, less than 0.1% of the CCSN rate.

By laying out the spectroscopic diversity of FBOTs classified as part of ZTF, our work illustrates the limitations of the simple cut on duration that has has been used in the literature. Figure 3 shows that an essential metric for selecting exotic events such as AT2018cow and SN 2018gep is the transient's peak luminosity. Currently, the completeness of galaxy redshift catalogs is only ≈50% even at $z = 0.05$ (Fremling et al. 2020). This fraction will be substantially improved by massively multiplexed spectroscopic surveys such as the Dark Energy Spectroscopic Instrument (DESI Collaboration et al. 2016). Transient luminosity estimates will also benefit from improved photometric redshifts from the Vera Rubin Observatory (Graham et al. 2018).

6. Summary

We present a systematically selected sample of FBOTs with spectroscopic classifications. The objects in our sample are similar to unclassified events in the literature in terms of their photometric evolution, host galaxy properties, and continuum-dominated spectra at peak light. By several weeks after peak light, the objects typically redden in color and develop spectra classifiable as traditional classes of CCSNe.

Our work supports suggestions in the literature that the dominant physical mechanisms at work in FBOTs are shock interaction with extended material, such as in the first peak of Type IIb SNe, and interaction, such as in Type Ibn SNe. Furthermore, we find that AT2018cow-like transients are a rare (<0.1% of CCSNe) subset of objects referred to broadly as FBOTs in the literature.

Identifying exotic FBOTs still requires substantial human intervention (Table 1). Events in a similar region of luminosity −timescale space to established SN classes (e.g., the ultrastripped SN 2019dge) must currently be identified through brute-force spectroscopic classification. Some exotic classes (e.g., AT2018cow-like objects or the Type Ic-BL SN 2018gep) stand out owing to their high luminosity. However, current galaxy redshift catalogs are highly incomplete, meaning that brute-force spectroscopic observations are still required to measure the redshift and distinguish exotic luminous objects at higher redshifts from more ordinary objects (e.g., Type IIb SNe) at lower redshifts. The completeness of galaxy redshifts in the local universe will increase in the next few years owing to massively multiplexed surveys such as DESI, but more targeted approaches will likely be required for the intermediate-redshift (z 0.1–0.3) galaxies in which most AT2018cow-like transients are currently being found.

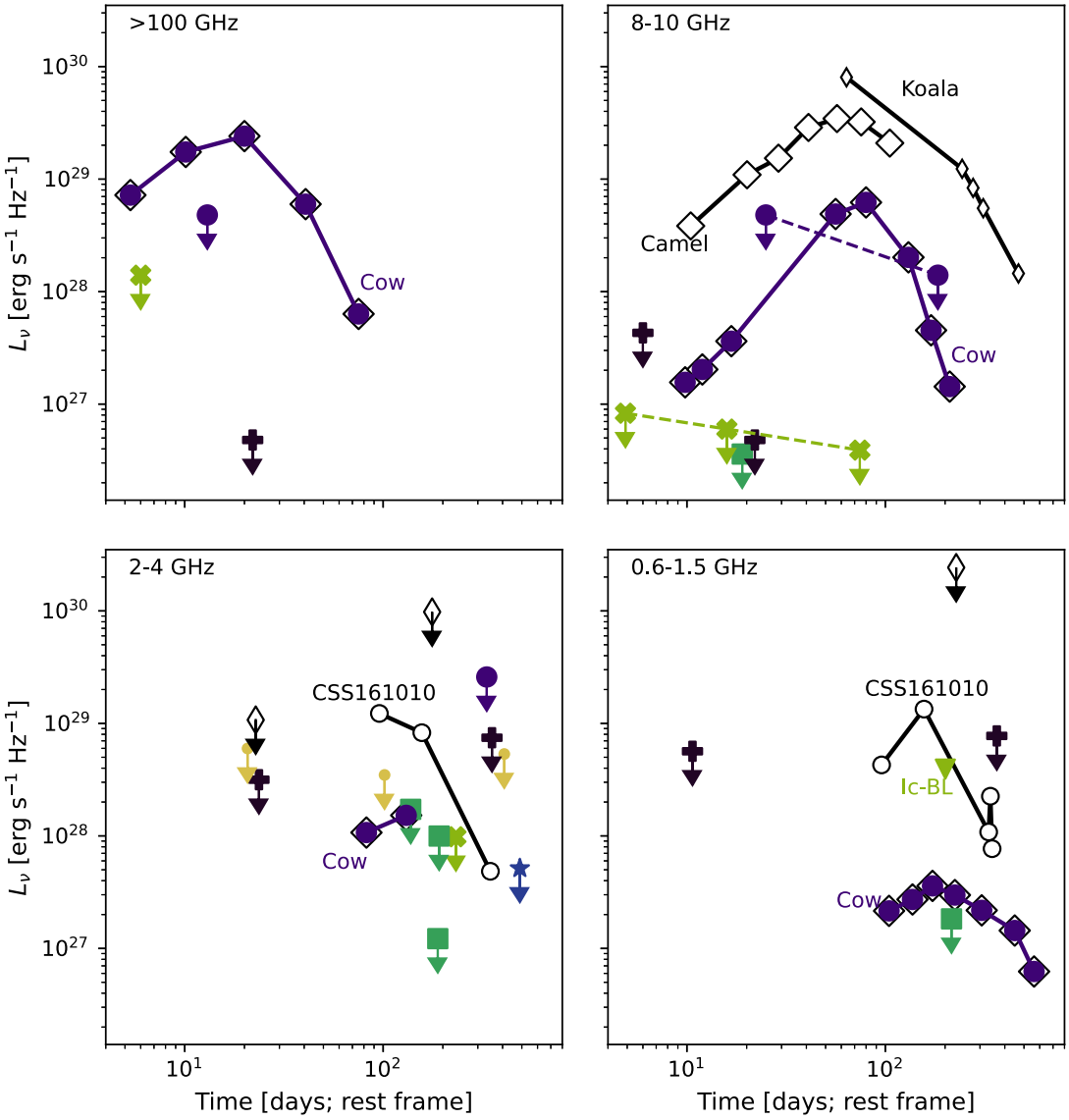

Figure 11. Millimeter and radio observations of ZTF FBOTs, with light curves of radio-loud FBOTs such as the Cow/AT2018cow and CSS161010 shown for comparison. The CSS161010 light curves are from Coppejans et al. (2020). The light curves of the Cow, the Koala/AT 2018lug, and SN 2018gep (Ic-BL) at 10 GHz were taken from the literature (Ho et al. 2019a; Margutti et al. 2019; Bietenholz et al. 2020; Coppejans et al. 2020; Ho et al. 2020b). The 10 GHz light curve of the Camel/AT 2020xnd is from Ho et al. (2022a). The 0.75 GHz light curve of the Cow is from Nayana & Chandra (2021). Additional observations at >100 GHz and 8–10 GHz are from this work. Limits at 2–4 GHz are from VLASS. Limits at 888 MHz are from the RACS and VAST (see text). In the bottom right panel, the positions of the Ic-BL and Ib markers have been shifted slightly for clarity. The only objects with robust detections of luminous (>10^{28} erg s^{-1} Hz^{-1}) millimeter and radio emission appear to be the shortest-duration, highest-luminosity optical transients: the Cow, the Koala, and the Camel.

In addition to the need for more complete galaxy redshift catalogs, we note that AT2018cow-like objects are primarily ultraviolet, not optical, transients. The Koala and the Camel have some of the bluest peak-light colors ($g-r=-0.6$ mag and $g-r=-0.4$, respectively) of the transients in Table 2. Such objects might therefore be more effectively discovered using wide-field ultraviolet time-domain surveys, such as ULTRASAT (Sagiv et al. 2014) and the Ultraviolet Explorer (Kulkarni et al. 2021).

The code used to produce the plots in this paper is available in a public Github repository.[48]

The authors would like to thank the anonymous referees for detailed comments that greatly improved the clarity of the paper. A.Y.Q.H. would like to thank Schuyler van Dyk for a thorough reading of the manuscript; Eliot Quataert, Dan Kasen, and Peter Nugent for useful discussions; and Miika Pursiainen for generously sharing the data for the DES objects. A.G.Y.'s research is supported by the EU via ERC grant No. 725161, the ISF GW excellence center, an IMOS space infrastructure grant, and BSF/Transformative and GIF grants, as well as The Benoziyo Endowment Fund for the Advancement of Science, the Deloro Institute for Advanced Research in Space and Optics, The Veronika A. Rabl Physics Discretionary Fund, Minerva, Yeda-Sela, and the Schwartz/Reisman Collaborative Science Program; A.G.Y. is the recipient of the Helen and Martin Kimmel Award for Innovative Investigation. R.L. acknowledges support from a Marie Skłodowska-Curie Individual Fellowship within the Horizon 2020 European Union (EU) Framework Programme for Research and Innovation (H2020-MSCA-IF-2017-794467).

[48] https://github.com/annayqho/fbot_survey.

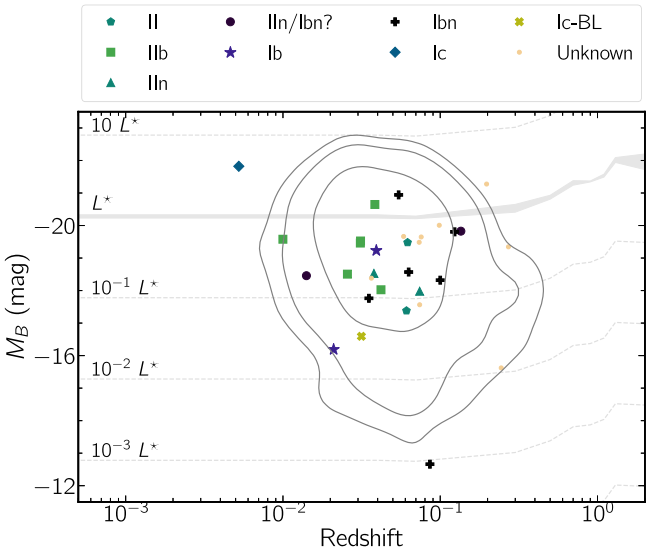

Figure 12. The absolute B magnitude of the host galaxies for the ZTF FBOTs as a function of redshift. Our events are found in the least luminous (10^{-3} $L^\star$) to the most luminous star-forming galaxies ($\lesssim 10^{-3}$ $L^\star$) ($L^\star$ is the characteristic luminosity of the B-band luminosity function of star-forming galaxies). Most hosts have luminosities of 10^{-2} to a few $L^\star$, similar to regular CCSNe (indicated by the contours encircling 68%, 90%, and 95% of the PTF+iPTF CCSN sample). We indicate the $L^\star$ presented in Faber et al. (2007) and multiples of it in gray.

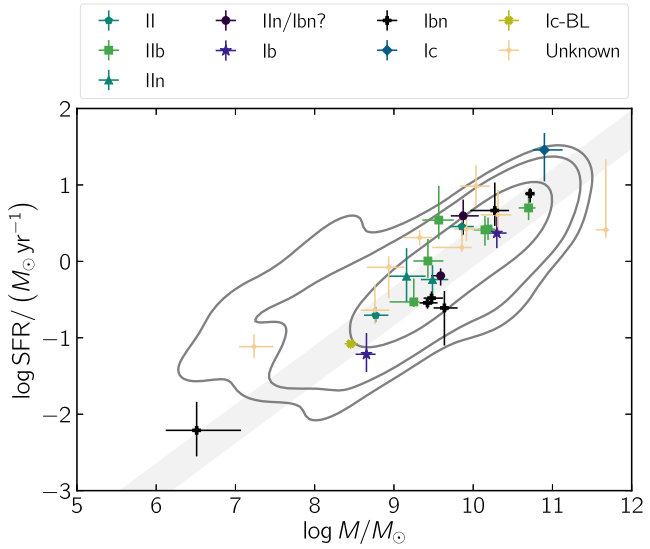

Figure 13. Host galaxies for ZTF FBOTs in the mass−SFR plane. Almost all exploded in star-forming galaxies. This is illustrated by their location with respect to the main sequence of star-forming galaxies (gray shaded region). The only exception is AT 2020bot, which exploded ∼10 kpc from the center of an elliptical galaxy. Moreover, the overwhelming majority of hosts also have properties consistent with those of CCSNe from the PTF+iPTF surveys (gray contours indicate the region encircling 68%, 90%, and 95% of the sample).

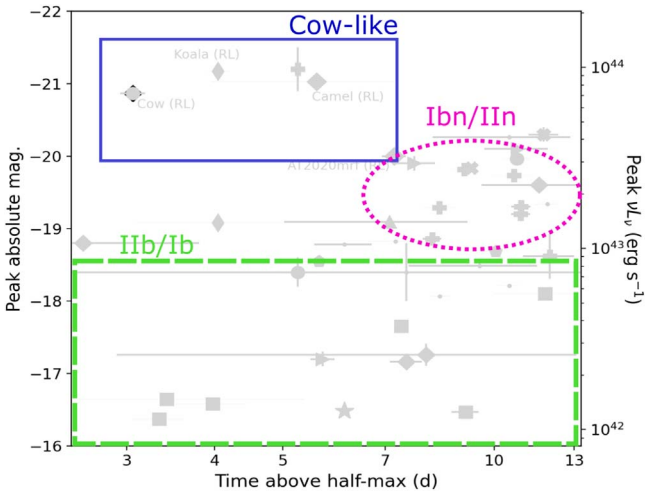

Figure 14. Same as Figure 3, but this time delineating predominant spectroscopic subgroups of FBOTs.

D.K. is supported by NSF grant AST-1816492. E.C.K. acknowledges support from the G.R.E.A.T research environment funded by *Vetenskapsrådet*, the Swedish Research Council, under project No. 2016–06012, and support from The Wenner-Gren Foundations. A.A.M. is funded by the Large Synoptic Survey Telescope Corporation (LSSTC), the Brinson Foundation, and the Moore Foundation in support of the LSSTC Data Science Fellowship Program; he also receives support as a CIERA Fellow by the CIERA Postdoctoral Fellowship Program (Center for Interdisciplinary Exploration and Research in Astrophysics, Northwestern University). E.O. O. acknowledges support from the Israeli Science Foundation, The Israeli Ministry of Science, The Bi-National Science foundation, and Minerva. A.J.C.T. acknowledges Y.-D. Hu and A. F. Azamat for their assistance regarding the GTC observation. L.T. acknowledges support from MIUR (PRIN 2017 grant 20179ZF5KS).

Based on observations obtained with the Samuel Oschin Telescope 48-inch and the 60-inch Telescope at the Palomar Observatory as part of the Zwicky Transient Facility project. ZTF is supported by the National Science Foundation under grant No. AST-1440341 and a collaboration including Caltech, IPAC, the Weizmann Institute for Science, the Oskar Klein Center at Stockholm University, the University of Maryland, the University of Washington, Deutsches Elektronen-Synchrotron and Humboldt University, Los Alamos National Laboratories, the TANGO Consortium of Taiwan, the University of Wisconsin at Milwaukee, and Lawrence Berkeley National Laboratories. Operations are conducted by COO, IPAC, and UW. The ZTF forced-photometry service was funded under the Heising-Simons Foundation grant No. 12540303 (PI: Graham). The GROWTH Marshal was supported by the GROWTH project funded by the National Science Foundation under grant No. 1545949.

SED Machine is based on work supported by the National Science Foundation under grant No. 1106171. The data presented here were obtained in part with ALFOSC, which is provided by the Instituto de Astrofisica de Andalucia (IAA) under a joint agreement with the University of Copenhagen and NOT. Based on observations made with the Gran Telescopio Canarias (GTC), installed at the Spanish Observatorio del Roque de los Muchachos of the Instituto de Astrofísica de Canarias, in the island of La Palma. Observations reported here were obtained at the MMT Observatory, a joint facility of the University of Arizona and the Smithsonian Institution. The Liverpool Telescope is operated on the island of La Palma by Liverpool John Moores University in the Spanish Observatorio del Roque de los Muchachos of the Instituto de Astrofisica de Canarias with financial support from the UK Science and Technology Facilities Council. Based on observations made with the Italian Telescopio Nazionale Galileo (TNG) operated on the island of La Palma by the Fundación Galileo Galilei of the INAF (Istituto Nazionale di Astrofisica) at the Spanish

Observatorio del Roque de los Muchachos of the Instituto de Astrofisica de Canarias.

Some of the data presented herein were obtained at the W. M. Keck Observatory, which is operated as a scientific partnership among the California Institute of Technology, the University of California, and the National Aeronautics and Space Administration. The Observatory was made possible by the generous financial support of the W. M. Keck Foundation. The authors wish to recognize and acknowledge the very significant cultural role and reverence that the summit of Maunakea has always had within the indigenous Hawaiian community. We are most fortunate to have the opportunity to conduct observations from this mountain.

This work made use of data supplied by the UK Swift Science Data Centre at the University of Leicester. The National Radio Astronomy Observatory is a facility of the National Science Foundation operated under cooperative agreement by Associated Universities, Inc. The Submillimeter Array is a joint project between the Smithsonian Astrophysical Observatory and the Academia Sinica Institute of Astronomy and Astrophysics and is funded by the Smithsonian Institution and the Academia Sinica. This work is based on observations carried out under project No. S19BC with the IRAM NOEMA Interferometer. IRAM is supported by INSU/CNRS (France), MPG (Germany), and IGN (Spain). The Australian SKA Pathfinder is part of the Australia Telescope National Facility, which is managed by CSIRO. Operation of ASKAP is funded by the Australian Government with support from the National Collaborative Research Infrastructure Strategy. ASKAP uses the resources of the Pawsey Supercomputing Centre. Establishment of ASKAP, the Murchison Radio-astronomy Observatory, and the Pawsey Supercomputing Centre are initiatives of the Australian Government, with support from the Government of Western Australia and the Science and Industry Endowment Fund. We acknowledge the Wajarri Yamatji people as the traditional owners of the Observatory site. Parts of this research were conducted by the Australian Research Council Centre of Excellence for Gravitational Wave Discovery (OzGrav), through project No. CE170100004.

This research made use of Astropy, a community-developed core Python package for Astronomy (Astropy Collaboration et al. 2013, 2018). The ztfquery code was funded by the European Research Council (ERC) under the European Union's Horizon 2020 research and innovation program (grant agreement No. 759194—USNAC, PI: Rigault).

The Legacy Surveys consist of three individual and complementary projects: the Dark Energy Camera Legacy Survey (DECaLS; Proposal ID #2014B-0404; PIs: David Schlegel and Arjun Dey), the Beijing-Arizona Sky Survey (BASS; NOAO Prop. ID #2015A-0801; PIs: Zhou Xu and Xiaohui Fan), and the Mayall *z*-band Legacy Survey (MzLS; Prop. ID #2016A-0453; PI: Arjun Dey). DECaLS, BASS, and MzLS together include data obtained, respectively, at the Blanco telescope, Cerro Tololo Inter-American Observatory, NSF's NOIRLab; the Bok telescope, Steward Observatory, University of Arizona; and the Mayall telescope, Kitt Peak National Observatory, NOIRLab. The Legacy Surveys project is honored to be permitted to conduct astronomical research on Iolkam Du'ag (Kitt Peak), a mountain with particular significance to the Tohono O'odham Nation.

This project used data obtained with the Dark Energy Camera (DECam), which was constructed by the Dark Energy Survey (DES) collaboration. Funding for the DES Projects has been provided by the U.S. Department of Energy, the U.S. National Science Foundation, the Ministry of Science and Education of Spain, the Science and Technology Facilities Council of the United Kingdom, the Higher Education Funding Council for England, the National Center for Supercomputing Applications at the University of Illinois at Urbana-Champaign, the Kavli Institute of Cosmological Physics at the University of Chicago, Center for Cosmology and Astro-Particle Physics at The Ohio State University, the Mitchell Institute for Fundamental Physics and Astronomy at Texas A&M University, Financiadora de Estudos e Projetos, Fundacao Carlos Chagas Filho de Amparo, Financiadora de Estudos e Projetos, Fundacao Carlos Chagas Filho de Amparo a Pesquisa do Estado do Rio de Janeiro, Conselho Nacional de Desenvolvimento Cientifico e Tecnologico and the Ministerio da Ciencia, Tecnologia e Inovacao, the Deutsche Forschungsgemeinschaft, and the Collaborating Institutions in the Dark Energy Survey. The Collaborating Institutions are Argonne National Laboratory, the University of California at Santa Cruz, the University of Cambridge, Centro de Investigaciones Energeticas, Medioambientales y Tecnologicas-Madrid, the University of Chicago, University College London, the DES-Brazil Consortium, the University of Edinburgh, the Eidgenossische Technische Hochschule (ETH) Zurich, Fermi National Accelerator Laboratory, the University of Illinois at Urbana-Champaign, the Institut de Ciencies de l'Espai (IEEC/CSIC), the Institut de Fisica d'Altes Energies, Lawrence Berkeley National Laboratory, the Ludwig Maximilians Universitat Munchen and the associated Excellence Cluster Universe, the University of Michigan, NSF's NOIRLab, the University of Nottingham, The Ohio State University, the University of Pennsylvania, the University of Portsmouth, SLAC National Accelerator Laboratory, Stanford University, the University of Sussex, and Texas A&M University. The Legacy Survey team makes use of data products from the Near-Earth Object Widefield Infrared Survey Explorer (NEOWISE), which is a project of the Jet Propulsion Laboratory/California Institute of Technology. NEOWISE is funded by the National Aeronautics and Space Administration. The Legacy Surveys imaging of the DESI footprint is supported by the Director, Office of Science, Office of High Energy Physics of the U.S. Department of Energy under contract No. DE-AC02-05CH1123, by the National Energy Research Scientific Computing Center, a DOE Office of Science User Facility under the same contract; and by the U.S. National Science Foundation, Division of Astronomical Sciences under contract No. AST-0950945 to NOAO.

Facilities: Hale, Swift, EVLA, VLA, Liverpool:2 m, PO:1.2 m, PO:1.5 m, NOT, GTC, Sloan, AAVSO, ASKAP, Keck:1, IRAM:NOEMA, SMA, MMT, TNG, ASKAP, GALEX, PS1, CTIO:2MASS, FLWO:2MASS, WISE, NEOWISE, Blanco, Gemini: North.

Software: `CASA` (McMullin et al. 2007), `astropy` (Astropy Collaboration et al. 2013, 2018), `matplotlib` (Hunter 2007), `scipy` (Virtanen et al. 2020), `ztfquery` (Rigault 2018), `extinction`, `penquins`.

Appendix A
Details of Individual Events

Here we provide details on the discovery and follow-up observations of events in our sample that have not yet been published elsewhere.

A.1. SN 2018ghd / ZTF18abvkmgw / ATLAS18vew

SN 2018ghd was detected by ATLAS (Tonry et al. 2018b; Smith et al. 2020a) on 2018 September 14 and reported to TNS the same day (Tonry et al. 2018a). It was first detected in ZTF data as ZTF18abvkmgw on 2018 September 12 as part of the Caltech 1DC survey at $g = 20.48 \pm 0.22$ mag and saved by an alert-stream scanner on September 13 as part of a filter for rapidly evolving transients. It was in a galaxy with an SDSS spectrum and known redshift of $z = 0.0385$. On September 15 it was saved by the CLU filter, and it was saved by the public BTS survey on September 16. As part of CLU and BTS, it received a series of SEDM spectra, with the first obtained on September 14. These spectra were not definitive for classification. It was classified as a Type II SN based on an SEDM spectrum on September 21 (Fremling et al. 2018) and then reclassified as a Type Ib SN with an LRIS spectrum on November 10.

A.2. SN 2018gjx / ZTF18abwkrbl / ATLAS18vis / Gaia18csc / kait-18ao / PS19do / PSP18C

SN 2018gjx was discovered by the Xingming Observatory Sky Survey (XOSS) as PSP18C on 2018 September 15 and reported to TNS on September 16 (Zhang et al. 2018). The source was coincident with NGC 865 ($z = 0.00999$). The first ZTF detection was also on 2018 September 15, at $g = 17.91 \pm 0.06$ mag, as part of the Caltech 1DC survey. The source was saved by alert-stream scanners on 2018 September 17 as part of the infant SN and CLU programs, and an SEDM spectrum was triggered that showed flash features; an SEDM spectrum obtained the next day showed that the features had disappeared. It was also saved as part of BTS on September 17, as it exceeded the 19th magnitude threshold in an image obtained as part of the public survey ($r = 16.16 \pm 0.04$ mag).

ePESSTO (Smartt et al. 2015) classified the source as SN II based on a September 18 spectrum obtained with the ESO Faint Object Spectrograph and Camera (EFOSC2) on the 3.6 m New Technology Telescope (NTT) at La Silla (Gromadzki et al. 2018). Based on an October 12 SEDM spectrum, the classification was revised to SN IIb (Dahiwale & Fremling 2020b).

A.3. SN 2019aajs / ZTF19aakssbm

SN 2019aajs was discovered by ZTF on 2019 February 25 at $r = 19.10 \pm 0.17$ mag in an image obtained as part of the high-cadence partnership survey. It was saved on February 26 as part of a search for rapidly evolving transients because it rose 1.5 mag in 1 day. This led to an extensive sequence of follow-up observations, including imaging, spectroscopy, millimeter, and radio. The object was classified as a Type Ibn SN using an LT spectrum taken on 2019 March 2.

A.4. SN 2019deh / ZTF19aapfmki / ATLAS19gez / PS19aaq

SN 2019deh was first detected in a ZTF public-survey image on 2019 April 7 at $r = 20.75 \pm 0.28$ mag and again the same night as part of the 1DC survey. It was reported to the TNS on April 10 (Nordin et al. 2019a) by the alert management, photometry, and evaluation of light curves (AMPEL) system (Soumagnac & Ofek 2018; Nordin et al. 2019g). It was classified as a Type Ibn SN by SPRAT using a spectrum obtained on 2019 April 12 (Prentice et al. 2019).

A.5. AT 2019esf / ZTF19aatoboa / PS19afa

AT 2019esf was discovered by ZTF in an image obtained on 2019 May 3 at $g = 19.97 \pm 0.16$ mag as part of the public survey and detected the next night as part of both the high-cadence and 1DC surveys. It was saved on May 4 by filters for infant SNe and fast transients. As part of the rapidly evolving transients program, it received a P60 spectrum at peak light that did not show distinct features. It was uploaded to TNS by AMPEL on May 6 (Nordin et al. 2019b). The host galaxy redshift was measured with a Keck spectrum on 2020 February 17.

A.6. AT 2019kyw / ZTF19abfarpa

AT 2019kyw was discovered by ZTF (Fremling 2019), first detected at $g = 20.18 \pm 0.31$ mag in an image obtained on 2019 July 6 as part of the public survey. It was saved as part of BTS, infant SNe, and CLU and received an inconclusive SEDM spectrum on July 9 as part of routine classification efforts. It received additional DBSP spectra on August 1 and August 9 that led to a redshift measurement but no conclusion about the transient itself.

A.7. SN 2019myn / ZTF19abobxik / PS19eop

SN 2019myn was discovered by ZTF (Nordin et al. 2019d), first detected at $g = 21.24 \pm 0.31$ mag in an image obtained on 2019 August 5 as part of the high-cadence partnership survey. It was saved by a filter for rapidly evolving transients on August 11, and SEDM and LT were triggered for spectroscopy and imaging. Given the rapid evolution, the VLA was triggered, and the observation took place on August 17. An LRIS spectrum on August 31 led to the Type Ibn classification. The source will be included in a Type Ibn sample paper by Kool et al.

A.8. SN 2019php / ZTF19abuvqgw / ATLAS19ufu

SN 2019php was discovered by ATLAS on September 2 and reported to TNS that day (Tonry et al. 2019b). The first ZTF detection was on 2019 August 31 as part of the public survey and passed the AMPEL filter (Nordin et al. 2019g). It was detected the next night (September 1) as part of the Caltech 1DC Survey and passed a filter for fast transients. As part of the fast-transient program, it received a spectrum with DBSP on September 9 that was relatively featureless. It received an additional spectrum on September 23 with LRIS that led to the Type Ibn classification.

A.9. SN 2019qav / ZTF19abyjzvd / PS19fbn

SN 2019qav was discovered by Pan-STARRS1 (Chambers et al. 2016) on September 11 and reported to TNS on

September 12 (Chambers et al. 2019). The first ZTF detection was at $r = 20.31 \pm 0.24$ mag on 2019 September 8 as part of the partnership high-cadence survey. It was saved on September 12 by the infant SN filter, and SEDM was triggered for a spectrum. On September 14 it was recognized that the rise was unusually fast. An LRIS spectrum on September 24 showed H and He features and led to the measurement of $z = 0.137$. Given the unusual spectrum, it was thought that this might be an analog to AT 2018cow, and as a result a variety of facilities were triggered: Swift, NOEMA, and the VLA. We obtained a spectrum of the host galaxy with LRIS on 2021 April 14, leading to a more precise redshift ($z = 0.1353$) from strong star-forming emission lines.

A.10. SN 2019rii / ZTF19acayojs / ATLAS19wqu

SN 2019rii was first identified in the ZTF public stream by ALeRCE broker (Förster et al. 2021) and reported to TNS on September 28. The first ZTF detection was on 2019 September 25 at $g = 20.30 \pm 0.21$ mag as part of the high-cadence partnership survey. It was saved on October 2 as part of a filter for rapidly evolving transients. It was observed the same night with DBSP, leading to the redshift measurement of $z = 0.1234$ from narrow emission lines from the host galaxy. An additional spectrum was obtained on October 26 with LRIS, which showed distinct He I lines. Given the He features and rapid evolution, it was tentatively classified as a Type Ibn.

A.11. SN 2019rta / ZTF19accjfgv

SN 2019rta was first detected on 2019 October 3 at $g = 17.96 \pm 0.07$ mag in the ZTF public survey and reported to TNS by AMPEL (Nordin et al. 2019g) the same day (Nordin et al. 2019e). The source was saved on October 3 as part of the BTS, and SEDM was triggered for a spectrum. It was saved again on October 5 as part of CLU, and a DBSP spectrum obtained that night showed a blue continuum and strong emission lines from the host galaxy. A final spectrum was obtained with LRIS on October 27 that led to the Type IIb classification (Dahiwale & Fremling 2019).

A.12. SN 2020ano / ZTF20aahfqpm

SN 2020ano was first detected on 2020 January 23 at $i = 19.93 \pm 0.21$ mag in an image obtained as part of the ZTF Uniform Depth Survey (ZUDS). It was also detected in a public image and reported to TNS the same day by ALeRCE (Forster et al. 2020e). It was saved by the AmpelRapid filter, and SEDM was triggered. The spectrum showed primarily a blue continuum. It was also saved that day by a filter for fast transients.

The next day (January 24) it was saved by scanners as part of the CLU experiment owing to its proximity to a galaxy at $z = 0.0311$. By this day, it was clear that it was fading quickly. From the blue colors and rapid behavior, it was thought to perhaps be a foreground CV. A GMOS-N spectrum was obtained on January 29, and by January 31 it was clear from ZUDS photometry that it was rising again in all three filters—this became clear in the regular alerts by February 6. An LRIS spectrum obtained on February 18 showed a good match to SN 1993J, leading to the Type IIb classification.

A.13. AT 2020bdh / ZTF20aaivtof / ATLAS20elz

AT 2020bdh was discovered by ALeRCE on 2020 January 27 using the ZTF public stream and reported to TNS the same day (Forster et al. 2020d). The magnitude at discovery was $g = 18.69 \pm 0.07$ mag. It was also detected the next night as part of the 1DC survey. It was saved on January 29 as part of CLU, on February 2 as part of a search for rapidly evolving transients, and on February 3 as part of the BTS. SEDM was triggered, but observations were unsuccessful. A broad Hα feature was noted in a report to TNS (Smith et al. 2020b) from an ePESSTO spectrum obtained on February 13. A DBSP spectrum obtained as part of routine ZTF classification led to a redshift measurement but not a definitive classification. The spectrum also tentatively showed a broad emission feature around Hα.

A.14. AT 2020bot / ZTF20aakypiu / PS20va

AT 2020bot was discovered by ZTF at $r = 20.41 \pm 0.24$ mag in an image obtained as part of ZUDS on 2020 January 30. On February 1 it passed the infant SN filter. Its proximity to an SDSS galaxy of known redshift ($z = 0.197$) implied a high luminosity; together with the fast rise, this led us to initiate follow-up observations, including LT and P60 imaging. DBSP and GMOS-N spectra were inconclusive, although the GMOS-N spectrum was noted to have broad features somewhat similar to young Ic-BL SNe. Attempts at follow-up spectroscopy with DBSP and Keck were unsuccessful.

A.15. SN 2020ikq / ATLAS20lfu / ZTF20aaxhzhc / PS20ctw

SN 2020ikq was discovered by ATLAS and reported to the TNS on 2020 April 28 (Tonry et al. 2020). It was first detected by ZTF and saved by a scanner on April 29 at $g = 18.42 \pm 0.08$ mag in public-survey data, as part of BTS and CLU. SN 2020ikq was classified as a Type IIb SN by the NOT on 2020 May 15 (Angus 2020).

A.16. SN 2020jmb / ZTF20aayrobw / ATLAS20lwn

SN 2020jmb was first detected on 2020 May 8 at $g = 19.52 \pm 0.21$ mag in the Caltech 1-day cadence survey. The source was saved by alert-stream scanners on 2020 May 10 as part of a search for rapidly evolving transients and separately as part of the CLU experiment owing to its proximity to a galaxy at $z = 0.032$ (the transient later proved unassociated). It was reported to TNS as part of CLU (De 2020a). The source was saved as part of BTS on 2020 May 11, when it exceeded the 19th magnitude threshold in an image obtained as part of the public survey ($g = 18.56 \pm 0.07$ mag). A spectrum was obtained with the SEDM on 2020 May 11 under the CLU program, which showed no distinct features. Additional spectra were obtained with the LT on May 16 and the SEDM on May 23, neither of which showed distinct features. Finally, a spectrum was obtained on May 27 with DBSP on the P200 for the rapidly evolving transients program, which showed a prominent Hα feature and narrow emission lines from the host galaxy consistent with $z = 0.061$, leading to the classification as a Type II SN (Dahiwale & Fremling 2020a).

A.17. SN 2020jji / ZTF20aazchcq / ATLAS20mfw / PS20czx

SN 2020jji was first detected in the ZTF public survey on 2020 May 1 at $r = 20.53 \pm 0.30$ mag. It was saved on May 10

as part of the AMPEL and CLU filters and reported to TNS that day (De 2020a). It received a follow-up spectrum by the SEDM that night, which was inconclusive. On May 16 it was saved by a scanner as part of the fast transients program and received a DBSP spectrum as part of that effort. The DBSP spectrum showed a Type IIn classification.

A.18. AT 2020kfw / ZTF20ababxjv / ATLAS20nfg

AT 2020kfw was first detected by ZTF on 2020 May 17 at $r = 20.53 \pm 0.20$ mag in an image obtained as part of the public survey and reported to TNS by ALeRCE (Forster et al. 2020a). It was detected later that night in the 1DC survey. On May 23 it had peaked and started fading, and as a result it passed a filter for fast transients. The resulting DBSP spectrum was of low quality and not conclusive.

A.19. AT 2020aexw / ZTF20abmocba

AT 2020aexw was discovered by ZTF, first detected on 2020 July 18 at $r = 20.52 \pm 0.21$ mag as part of ZUDS. It was saved on July 19 by AMPEL and on July 26 by the rapidly evolving transients program. LT follow-up imaging was acquired. A NOT spectrum was attempted but not successful. A DBSP spectrum was obtained on August 12, resulting in a redshift measurement from very strong emission lines.

A.20. AT 2020yqt / ZTF20abummyz / PS20ksm

AT 2020yqt was discovered by Pan-STARRS1 on 2020 August 22 and reported to TNS on 2020 November 1 (Chambers et al. 2020). It was first detected as part of the ZTF 1DC survey on 2020 August 19 at $r = 19.95 \pm 0.17$ mag and saved by a scanner on August 20 as part of a filter for rapidly evolving transients. The host galaxy had an SDSS spectrum that classified it as a starburst, with a redshift $z = 0.09855 \pm 0.00001$. Due to the fast evolution, we triggered a Gemini ToO program (PI: A. Miller) and obtained a GMOS-N spectrum on August 25 that was primarily featureless. Subsequent spectra with P200 and LRIS did not show obvious SN features and were dominated by host galaxy light.

A.21. SN 2020rsc / ZTF20aburywx / ATLAS20xxj

SN 2020rsc was first detected on 2020 August 19 as part of the public survey at $g = 19.58 \pm 0.17$ mag and reported to TNS by ALeRCE (Forster et al. 2020c). It was also detected that night as part of the Caltech 1DC survey and saved on 2020 August 20 by a filter for rapidly evolving transients. The next day, it was noted that it was already fading, and a Gemini ToO was triggered. The GMOS-N spectrum on August 22 showed He I at 8000 km s^{-1}. On 2020 August 22 the source passed the CLU filter. An additional spectrum with MMT+Binospec was obtained on August 24, and a GTC spectrum was obtained on August 25. Swift was triggered and observed on August 26, and the VLA was triggered on September 2, with the observation taking place on September 9. A final Keck spectrum on September 15 led to the Type IIb classification.

A.22. SN 2020vyv / ZTF20acigusw / ATLAS20bdhi / PS20kra

SN 2020vyv was first detected in the ZTF public survey on 2020 October 12 at $r = 19.17 \pm 0.10$ mag. It was saved the same day by AMPEL and the BTS survey and reported to TNS (Fremling 2020). It was classified as a Type II SN with a Keck/LRIS spectrum on 2020 October 14 (Siebert et al. 2020).

A.23. SN 2020xlt / ZTF20aclfmwn

SN 2020xlt was first detected on 2020 October 19 in public-survey data at $r = 19.93 \pm 0.22$, and it was reported to TNS that day by ALeRCE (Forster et al. 2020b). It was also detected that night as part of the Caltech 1DC survey and the next night as part of the high-cadence partnership survey. It was saved on October 19 as part of AMPEL (Nordin et al. 2019g) and the infant SN program, and SEDM was triggered: the spectrum was featureless. Despite the proximity to a bright extended galaxy, the redshift was unknown. The transient was noted to be fading on October 22, and on October 26 it passed a filter for rapidly evolving transients, leading to a GTC+OSIRIS spectrum on 2020 October 30 that enabled the redshift measurement of $z = 0.0389$ and the classification as a Type IIb.

Appendix B
Photometric Evolution of Individual Events

In Figure 15 we provide light curves for the Table 2 transients that are not included in Figure 1.

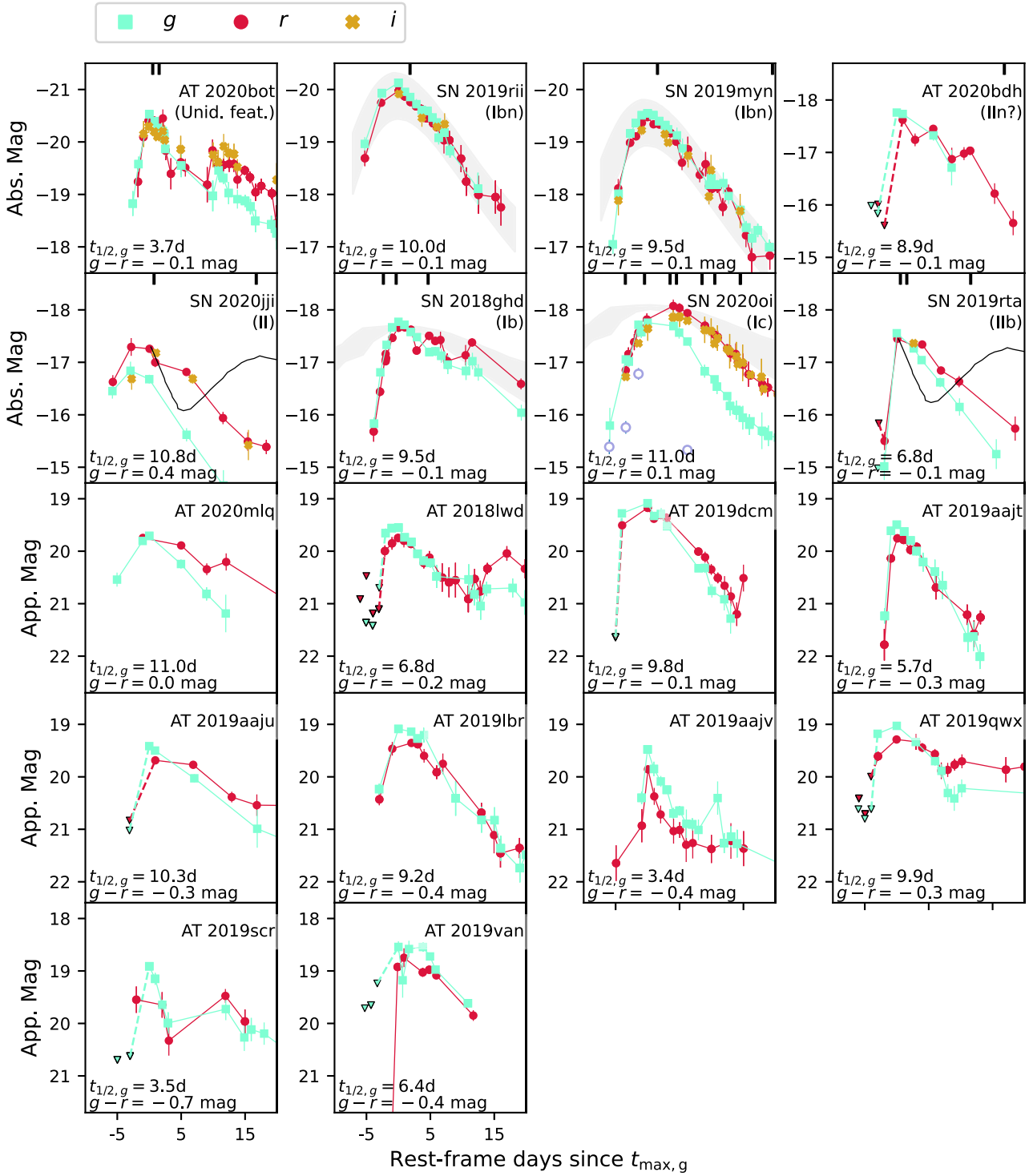

Figure 15. Light curves for ZTF transients in Table 2 that are not shown in Figure 1. In panels with H-poor SNe we show the Type Ibc template from Drout et al. (2011) for reference. In the Type II and Type IIb panels we show the *V*-band light curve of SN 1993J (Schmidt et al. 1993) for reference. In some cases light curves have been binned by day for clarity.

Appendix C
Log of Optical Spectra

In Table 11 we provide the full log of optical spectra, some of which were obtained from TNS. We do not report observations for objects with extensive spectroscopic observations previously presented in the literature: AT 2018cow (Perley et al. 2019), SN 2018gep (Ho et al. 2019a), SN 2019dge (Yao et al. 2020), and SN 2020oi.

Table 11
Log of Spectroscopic Observations of Objects Presented in This Paper

Name	UT Date	Target	Phase	Telescope + Instrument
SN 2018ghd	20180914	Transient	−2	P60+SEDM
SN 2018ghd	20180916	Transient	0	P60+SEDM
SN 2018ghd	20180921	Transient	4	P60+SEDM
SN 2018ghd	20181110	Transient	54	Keck I+LRIS
SN 2018ghd	20190105	Transient	110	Keck I+LRIS
SN 2018gjx	20180918	Transient	0	P60+SEDM
SN 2018gjx	20180918	Transient	0	EFOSC2+NTT (1)
SN 2018gjx	20180919	Transient	0	P60+SEDM
SN 2018gjx	20181012	Transient	23	P60+SEDM
SN 2018gjx	20181016	Transient	27	NOT+ALFOSC
SN 2018gjx	20181110	Transient	52	Keck I+LRIS
SN 2018gjx	20181130	Transient	72	TNG+DOLORES
SN 2018gjx	20190105	Transient	108	Keck I+LRIS
SN 2018gjx	20190706	Transient	290	Keck I+LRIS
SN 2019aajs	20190227	Transient	−1	LT+SPRAT
SN 2019aajs	20190302	Transient	1	LT+SPRAT
SN 2019aajs	20190304	Transient	3	NOT+ALFOSC
SN 2019aajs	20190315	Transient	14	NOT+ALFOSC
SN 2019aajs	20190406	Transient	36	Keck I+LRIS
SN 2019deh	20190410	Transient	−4	P60+SEDM
SN 2019deh	20190410	Transient	−4	LT+SPRAT
SN 2019deh	20190411	Transient	−3	LT+SPRAT
SN 2019deh	20190412	Transient	−2	LT+SPRAT
SN 2019deh	20190414	Transient	0	LT+SPRAT
SN 2019deh	20190415	Transient	0	P60+SEDM
SN 2019deh	20190423	Transient	8	NOT+ALFOSC
SN 2019deh	20190423	Transient	8	P60+SEDM
SN 2019deh	20190424	Transient	9	P200+DBSP
SN 2019deh	20190428	Transient	13	P60+SEDM
SN 2019deh	20190511	Transient	26	NOT+ALFOSC
AT 2019esf	20190504	Transient	−2	P60+SEDM
AT 2019esf	20200218	Host	287	Keck I+LRIS
AT 2019kyw	20190709	Transient	−3	P60+SEDM
AT 2019kyw	20190801	Transient	19	P200+DBSP
AT 2019kyw	20190809	Transient	27	P200+DBSP
SN 2019myn	20190813	Transient	1	P60+SEDM
SN 2019myn	20190831	Transient	19	Keck I+LRIS
SN 2019php	20190907	Transient	2	P200+DBSP
SN 2019php	20190924	Transient	19	Keck I+LRIS
SN 2019qav	20190911	Transient	−2	P60+SEDM
SN 2019qav	20190924	Transient	10	Keck I+LRIS
SN 2019qav	20190928	Transient	14	Keck I+LRIS
SN 2019qav	20191027	Transient	43	Keck I+LRIS
SN 2019rii	20191003	Transient	1	P200+DBSP
SN 2019rii	20191027	Transient	25	Keck I+LRIS
SN 2019rta	20191004	Transient	0	P60+SEDM
SN 2019rta	20191005	Transient	1	P200+DBSP
SN 2019rta	20191015	Transient	11	P60+SEDM
SN 2019rta	20191027	Transient	23	Keck I+LRIS
SN 2020ano	20200125	Transient	1	P60+SEDM
SN 2020ano	20200129	Transient	5	Gemini+GMOS
SN 2020ano	20200214	Transient	21	P200+DBSP
SN 2020ano	20200218	Transient	25	Keck I+LRIS
AT 2020bdh	20200213	Transient	16	EFOSC2+NTT (2)
AT 2020bdh	20200226	Transient	29	P200+DBSP
AT 2020bot	20200202	Transient	0	P200+DBSP
AT 2020bot	20200203	Transient	1	Gemini+GMOS
SN 2020ikq	20200429	Transient	−3	P60+SEDM
SN 2020ikq	20200503	Transient	0	P60+SEDM
SN 2020ikq	20200510	Transient	7	LT+SPRAT
SN 2020ikq	20200511	Transient	8	P60+SEDM
SN 2020ikq	20200515	Transient	12	NOT+ALFOSC
SN 2020ikq	20200517	Transient	14	P60+SEDM
SN 2020jmb	20200511	Transient	−1	P60+SEDM

Table 11
(Continued)

Name	UT Date	Target	Phase	Telescope + Instrument
SN 2020jmb	20200516	Transient	3	LT+SPRAT
SN 2020jmb	20200523	Transient	10	P60+SEDM
SN 2020jmb	20200528	Transient	15	P200+DBSP
SN 2020jji	20200511	Transient	0	P60+SEDM
SN 2020jji	20200527	Transient	16	P200+DBSP
AT 2020kfw	20200528	Transient	5	P200+DBSP
AT 2020aexw	20200812	Host	21	P200+DBSP
AT 2020yqt	20200825	Transient	5	Gemini+GMOS
AT 2020yqt	20200829	Transient	9	P200+DBSP
AT 2020yqt	20200920	Transient	31	Keck I+LRIS
SN 2020rsc	20200822	Transient	−2	Gemini+GMOS
SN 2020rsc	20200824	Transient	0	MMT+**Binospec**
SN 2020rsc	20200825	Transient	0	GTC+OSIRIS
SN 2020rsc	20200915	Transient	21	Keck I+LRIS
SN 2020vyv	20201014	Transient	1	Keck I+LRIS (3)
SN 2020xlt	20201028	Transient	8	P60+SEDM
SN 2020xlt	20201030	Transient	10	GTC+OSIRIS

Note. Phase given with respect to the observed maximum of the *g*-band light curve.
References. (1) Gromadzki et al. 2018; (2) Smith et al. 2020b; (3) Siebert et al. 2020.

Appendix D
Spectroscopic Evolution of Individual Events

In Figures 16–19, we plot the full set of spectra for each object.

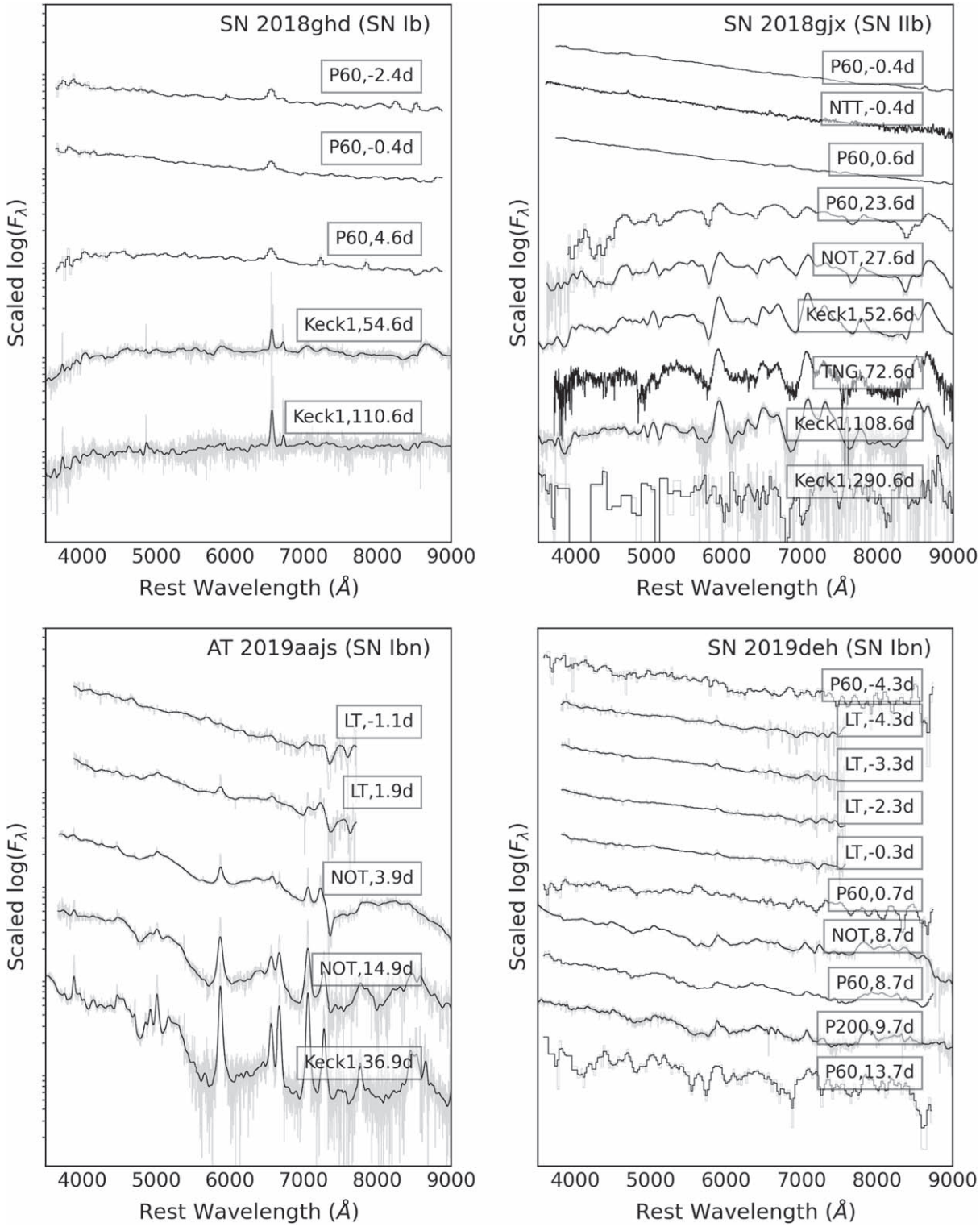

Figure 16. Spectroscopic evolution for the ZTF transients in Table 2. Raw spectra are shown in light gray, and smoothed spectra are overlaid in black.

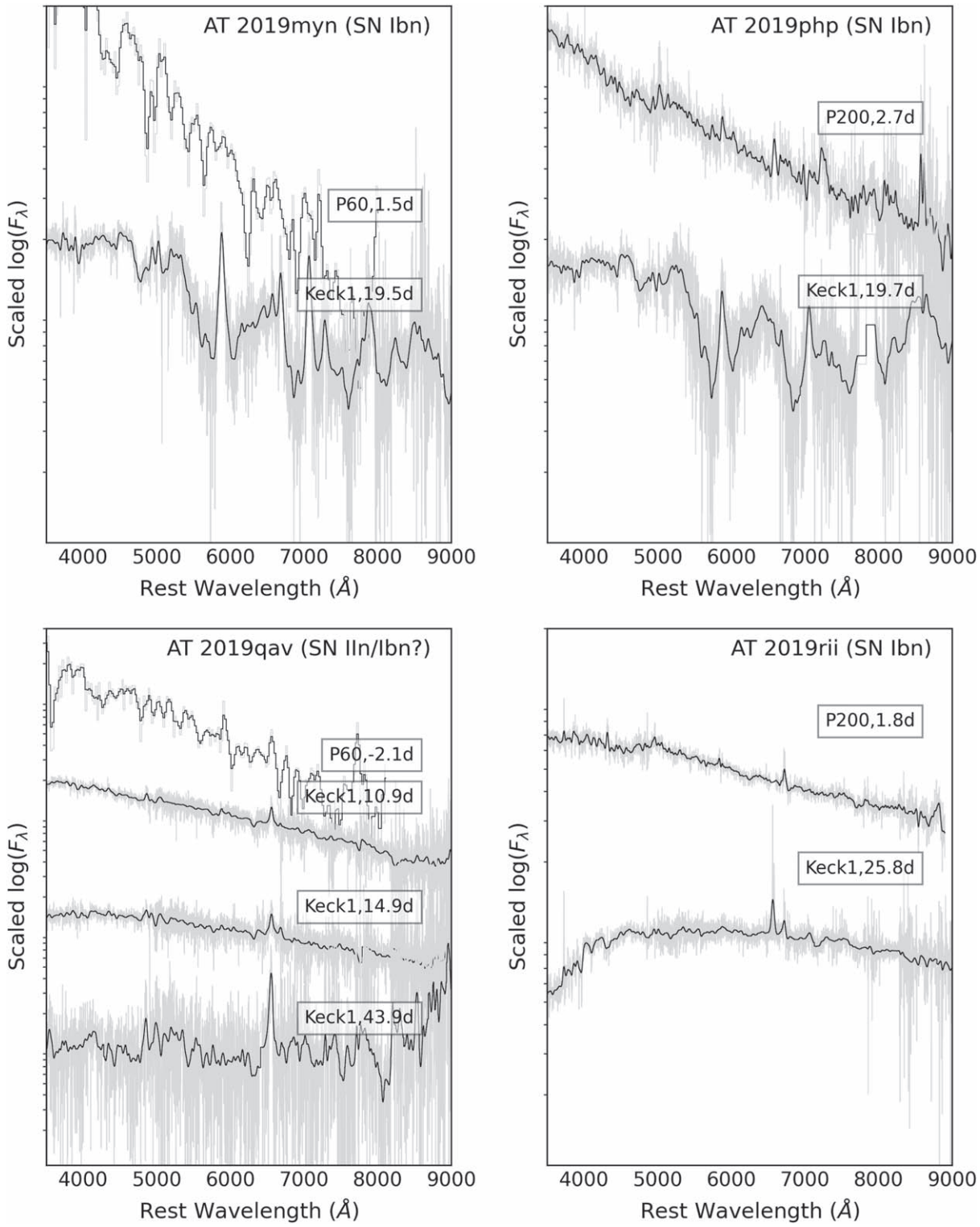

Figure 17. Spectroscopic evolution for the ZTF transients in Table 2. Raw spectra are shown in light gray, and smoothed spectra are overlaid in black.

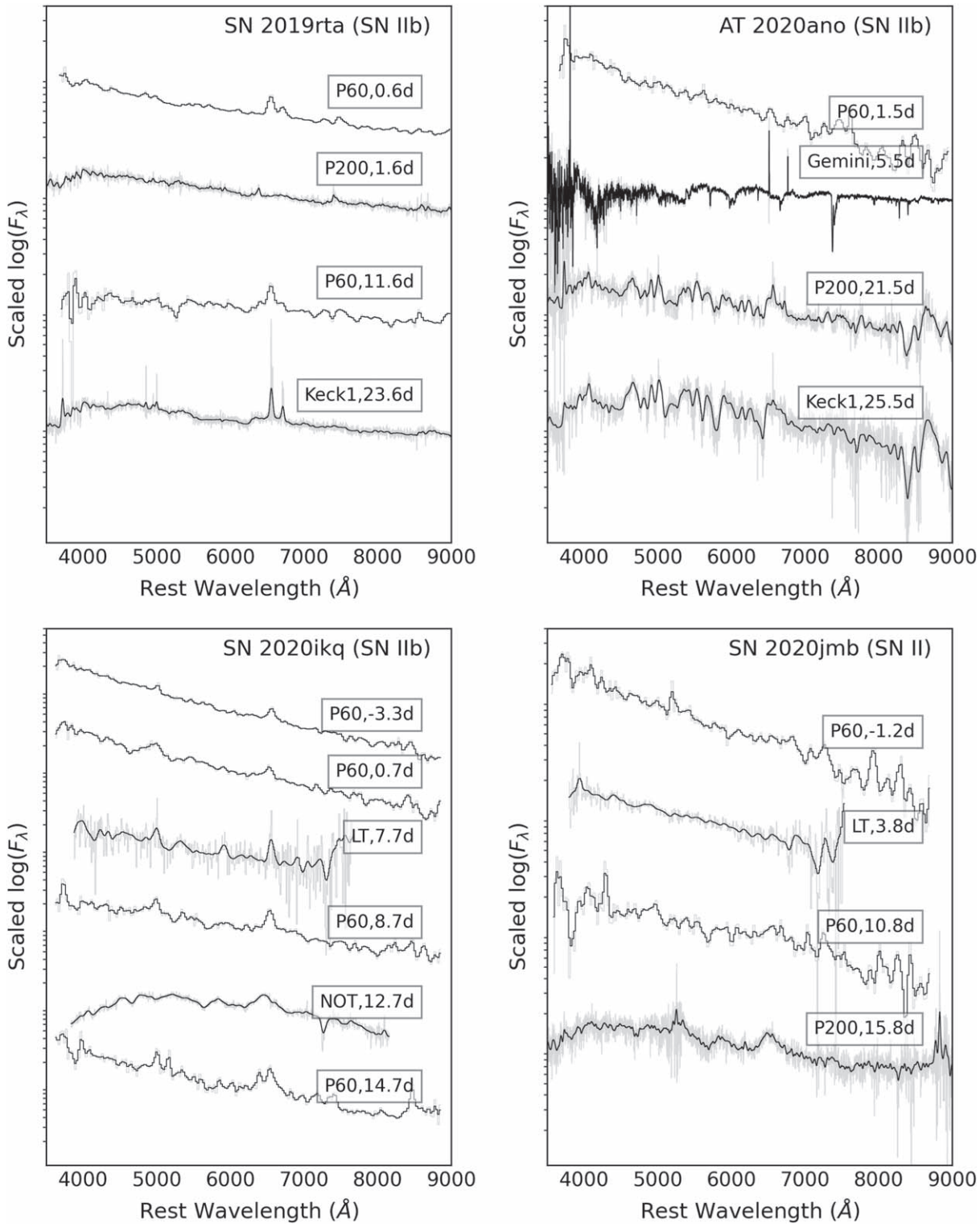

Figure 18. Spectroscopic evolution for the ZTF transients in Table 2. Raw spectra are shown in light gray, and smoothed spectra are overlaid in black.

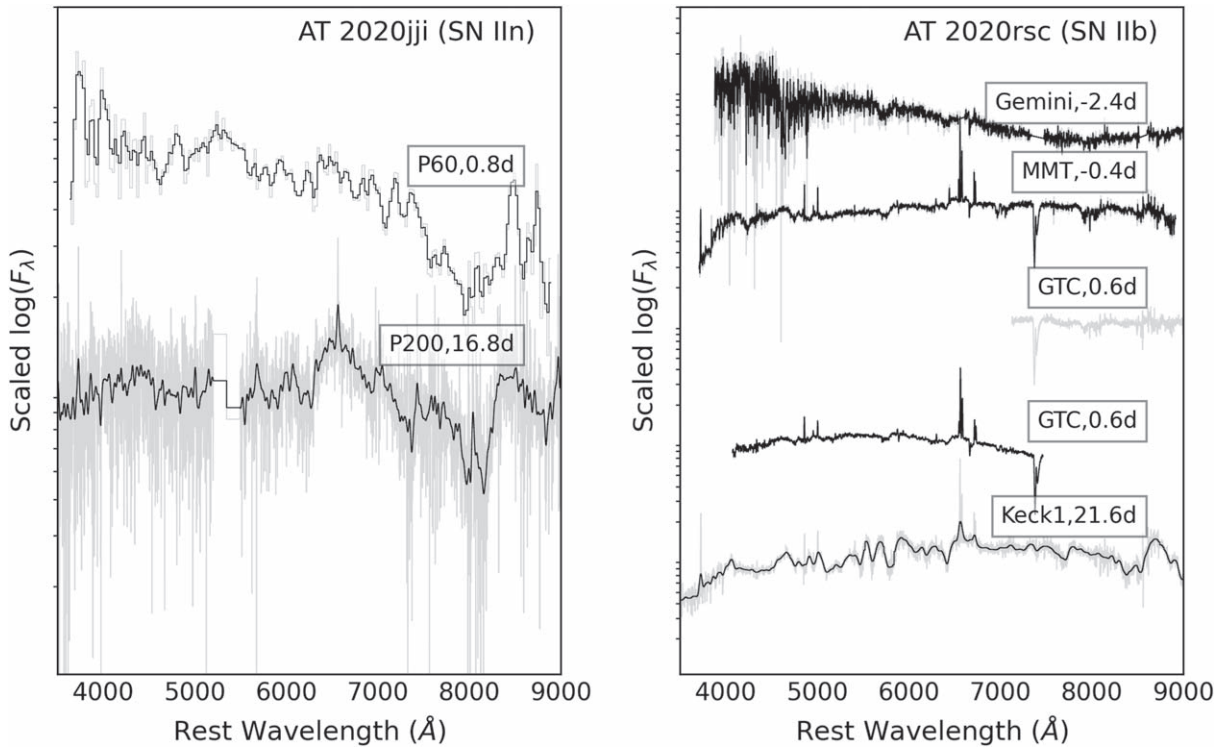

Figure 19. Spectroscopic evolution for the ZTF transients in Table 2. Raw spectra are shown in light gray, and smoothed spectra are overlaid in black.

Appendix E
Host Galaxy Properties

In this appendix we provide additional details and figures for the host galaxy properties described in Section 3.4. We model the spectral energy distributions (SEDs) with the software package CIGALE (Code Investigating GALaxy Evolution; Burgarella et al. 2005; Noll et al. 2009; Boquien et al. 2019). The models and fitting parameters are summarized in Table 12. We adopt the Bruzual & Charlot (2003) simple stellar population model to compute the stellar emission and the Chabrier (2003) initial mass function. Furthermore, we assume a linear-exponential star formation history (SFH; functional form $t \times \exp(-t/\tau)$, where t is the age of the SFH episode and τ is the e-folding timescale). To calculate the nebular emission from the ionized gas in H II regions, we fix the CIGALE ionization parameter log $U_{\rm ion}$ as -2. We use a modified Calzetti et al. (2000) starburst attenuation curve to model the dust attenuation. Dust emission was included via the Dale et al. (2014) dust templates. More details on the models used can be found in Boquien et al. (2019). We generate 24,385,536 models and choose the best-fit SED using Bayesian inference. In Figure 20 we show the best-fit SED for the host galaxy of AT 2020yqt as an example, and we list the derived host-galaxy properties in Table 13.

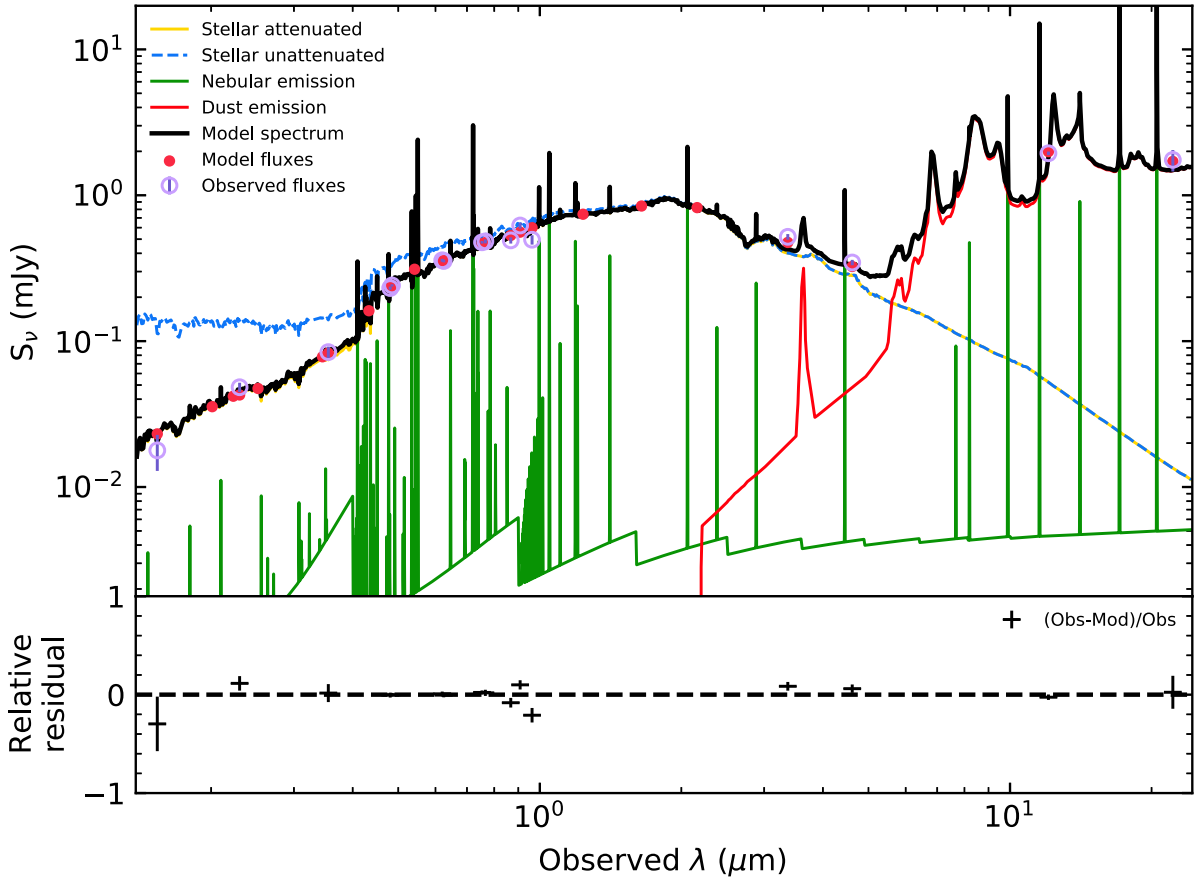

Figure 20. The SED of AT 2020yqt's host galaxy (open circles) from the UV to mid-IR. The solid black line shows the best-fitting model of the SED. The SED model consists of a stellar component (yellow curve); a contribution from ionized gas, e.g., star-forming regions (green curve); and emission from heated dust (red curve) at >30,000 Å. The photometry predicted by the best-fit model is shown by the red circles. The blue curve represents the stellar component corrected for host attenuation.

Table 12
The Models and Fitting Parameters Used for CIGALE

Galaxy Attributes	Brief Description
SFH	SFR $\propto \frac{t}{\tau^2}\exp(-t/\tau)$ τ = 250, 500, 1000, 2000, 4000, 6000, 8000 Myr Age t = 250, 500, 1000, 2000, 4000, 8000, 12,000 Myr
SSP models	BC03 (Bruzual & Charlot 2003) + Chabrier IMF (Chabrier 2003) Stellar metallicity = 0.0004, 0.004, 0.008, 0.02 $Z_\odot$
Dust attenuation	Modified power-law curves (Calzetti et al. 2000) + differential reddening of stars according to age $E(B-V)_{\rm young}$ = 0.0, 0.2, 0.3, 0.5, 0.8, 1.0, 1.5, 2.0, 3.0 $E(B-V)_{\rm old}$ = 0.3, 0.50, 1.0 UV − bump wavelength = 217.5 nm UV − bump amplitude = 0.0, 1.0, 2.0, 3.0 power-law slope = −0.13, −0.2 , −0.5
Dust emission	Dust templates of Dale et al. (2014) + energy balance AGN fraction = 0 alpha = 1.0, 1.5, 2.0, 2.5
Nebular	log $U_{\rm ion}$ = −2.0 emission-line width = 300.0 km s^{-1}

Table 13
Summary of the Host Galaxy SED Modeling

Object	χ^2/n. o. f.	M_B (mag)	log $M/M_\odot$	log SFR/($M_\odot$ yr^{-1})	logAge yr^{-1}	$E(B-V)$ (mag)
SN 2018bcc	2.10/9	−18.57	$9.47^{+0.15}_{-0.10}$	$-0.48^{+0.09}_{-0.08}$	$9.91^{+0.12}_{-0.19}$	$0.25^{+0.06}_{-0.03}$
AT2018cow	56.74/24	−18.46	$9.59^{+0.06}_{-0.12}$	$-0.19^{+0.10}_{-0.13}$	$9.93^{+0.10}_{-0.15}$	$0.25^{+0.07}_{-0.04}$
SN 2019dge	0.61/14	−16.19	$8.65^{+0.12}_{-0.14}$	$-1.22^{+0.28}_{-0.23}$	$9.89^{+0.13}_{-0.21}$	$0.31^{+0.15}_{-0.08}$
SN 2018gep	9.85/19	−16.59	$8.45^{+0.09}_{-0.08}$	$-1.08^{+0.04}_{-0.07}$	$9.81^{+0.18}_{-0.19}$	$0.25^{+0.06}_{-0.03}$
SN 2018ghd	2.09/15	−19.23	$10.30^{+0.12}_{-0.13}$	$0.37^{+0.32}_{-0.20}$	$9.89^{+0.13}_{-0.23}$	$0.58^{+0.43}_{-0.24}$
SN 2018gjx	3.11/16	−19.58	$10.19^{+0.08}_{-0.13}$	$0.42^{+0.15}_{-0.14}$	$9.91^{+0.12}_{-0.21}$	$0.28^{+0.12}_{-0.06}$
SN 2019aajs	1.55/9	−17.76	$9.64^{+0.17}_{-0.14}$	$-0.61^{+0.22}_{-0.49}$	$9.94^{+0.09}_{-0.13}$	$0.28^{+0.11}_{-0.06}$
SN 2019deh	5.75/17	−20.94	$10.72^{+0.05}_{-0.07}$	$0.89^{+0.07}_{-0.12}$	$9.95^{+0.09}_{-0.12}$	$0.25^{+0.06}_{-0.03}$
SN 2019myn	5.43/14	−18.32	$9.42^{+0.13}_{-0.10}$	$-0.54^{+0.06}_{-0.08}$	$9.90^{+0.13}_{-0.19}$	$0.25^{+0.06}_{-0.03}$
SN 2019php	1.27/3	−12.66	$6.51^{+0.56}_{-0.39}$	$-2.21^{+0.37}_{-0.34}$	$8.94^{+0.80}_{-0.38}$	$0.37^{+0.58}_{-0.13}$
SN 2019qav	14.49/18	−19.83	$9.87^{+0.20}_{-0.16}$	$0.60^{+0.21}_{-0.25}$	$9.66^{+0.22}_{-0.50}$	$0.25^{+0.08}_{-0.04}$
SN 2019rii	4.23/10	−19.81	$10.27^{+0.18}_{-0.31}$	$0.67^{+0.37}_{-0.20}$	$9.84^{+0.17}_{-0.63}$	$0.28^{+0.15}_{-0.06}$
SN 2019rta	10.75/11	−18.50	$9.43^{+0.20}_{-0.18}$	$0.01^{+0.29}_{-0.22}$	$9.72^{+0.24}_{-0.55}$	$0.33^{+0.19}_{-0.10}$
SN 2020oi	1.22/10	−21.82	$10.90^{+0.23}_{-0.14}$	$1.46^{+0.22}_{-0.41}$	$9.75^{+0.23}_{-0.52}$	$0.43^{+0.49}_{-0.15}$
SN 2020ano	0.64/7	−19.52	$9.57^{+0.19}_{-0.21}$	$0.54^{+0.45}_{-0.25}$	$9.23^{+0.55}_{-0.49}$	$0.32^{+0.26}_{-0.09}$
SN 2020ikq	8.57/16	−18.02	$9.25^{+0.07}_{-0.31}$	$-0.53^{+0.31}_{-0.07}$	$9.91^{+0.12}_{-0.49}$	$0.25^{+0.06}_{-0.03}$
SN 2020jmb	5.93/13	−17.38	$8.77^{+0.16}_{-0.15}$	$-0.70^{+0.11}_{-0.09}$	$9.78^{+0.20}_{-0.41}$	$0.26^{+0.08}_{-0.04}$
SN 2020jji	1.00/14	−18.53	$9.49^{+0.20}_{-0.15}$	$-0.24^{+0.19}_{-0.32}$	$9.86^{+0.15}_{-0.21}$	$0.25^{+0.08}_{-0.04}$
SN 2020rsc	9.05/14	−19.46	$10.15^{+0.13}_{-0.14}$	$0.41^{+0.18}_{-0.21}$	$9.88^{+0.14}_{-0.25}$	$0.32^{+0.15}_{-0.09}$
SN 2020vyv	4.68/18	−19.48	$9.86^{+0.15}_{-0.15}$	$0.46^{+0.20}_{-0.12}$	$9.74^{+0.23}_{-0.50}$	$0.26^{+0.11}_{-0.05}$
SN 2020xlt	6.18/11	−20.65	$10.70^{+0.09}_{-0.12}$	$0.70^{+0.16}_{-0.16}$	$9.93^{+0.10}_{-0.15}$	$0.26^{+0.09}_{-0.04}$
AT2018lug	19.49/14	−19.34	$9.32^{+0.16}_{-0.21}$	$0.31^{+0.10}_{-0.10}$	$9.29^{+0.22}_{-0.32}$	$0.25^{+0.06}_{-0.03}$
AT2019esf	23.53/17	−19.65	$9.91^{+0.18}_{-0.15}$	$0.42^{+0.20}_{-0.16}$	$9.78^{+0.21}_{-0.50}$	$0.29^{+0.11}_{-0.06}$
AT2019kyw	4.10/11	−17.56	$8.76^{+0.18}_{-0.18}$	$-0.64^{+0.33}_{-0.18}$	$9.70^{+0.25}_{-0.56}$	$0.28^{+0.11}_{-0.06}$
AT2020bdh	2.95/11	−18.38	$8.93^{+0.20}_{-0.27}$	$-0.08^{+0.14}_{-0.41}$	$9.22^{+0.64}_{-0.32}$	$0.25^{+0.06}_{-0.03}$
AT2020bot	10.77/17	−21.28	$11.67^{+0.04}_{-0.12}$	$0.41^{+0.92}_{-0.10}$	$9.78^{+0.09}_{-0.12}$	$0.29^{+0.53}_{-0.07}$
AT2020kfw	2.96/15	−19.66	$10.31^{+0.17}_{-0.22}$	$0.61^{+0.33}_{-0.25}$	$9.84^{+0.17}_{-0.50}$	$0.42^{+0.51}_{-0.16}$
AT2020aexw	10.15/16	−19.48	$9.86^{+0.12}_{-0.38}$	$0.18^{+0.36}_{-0.05}$	$9.90^{+0.12}_{-0.66}$	$0.26^{+0.11}_{-0.05}$
AT2020yqt	7.74/16	−20.01	$10.04^{+0.17}_{-0.20}$	$0.98^{+0.27}_{-0.26}$	$9.26^{+0.55}_{-0.36}$	$0.42^{+0.48}_{-0.14}$
AT2020xnd	4.62/3	−15.62	$7.23^{+0.25}_{-0.19}$	$-1.12^{+0.16}_{-0.15}$	$8.71^{+0.35}_{-0.22}$	$0.27^{+0.11}_{-0.05}$

Note. The absolute magnitudes are not corrected for host reddening. The SFRs are corrected for host reddening. The abbreviation "n.o.f." stands for number of filters. The "age" in the last column refers to the age of the stellar population.

ORCID iDs

Anna Y. Q. Ho https://orcid.org/0000-0002-9017-3567
Daniel A. Perley https://orcid.org/0000-0001-8472-1996
Avishay Gal-Yam https://orcid.org/0000-0002-3653-5598
Ragnhild Lunnan https://orcid.org/0000-0001-9454-4639
Jesper Sollerman https://orcid.org/0000-0003-1546-6615
Steve Schulze https://orcid.org/0000-0001-6797-1889
Kaustav K. Das https://orcid.org/0000-0001-8372-997X
Dougal Dobie https://orcid.org/0000-0003-0699-7019
Yuhan Yao https://orcid.org/0000-0001-6747-8509
Christoffer Fremling https://orcid.org/0000-0002-4223-103X
Shreya Anand https://orcid.org/0000-0003-3768-7515
Igor Andreoni https://orcid.org/0000-0002-8977-1498
Eric C. Bellm https://orcid.org/0000-0001-8018-5348
Rachel J. Bruch https://orcid.org/0000-0001-8208-2473
Kevin B. Burdge https://orcid.org/0000-0002-7226-836X
Alberto J. Castro-Tirado https://orcid.org/0000-0003-2999-3563
Richard Dekany https://orcid.org/0000-0002-5884-7867
Andrew J. Drake https://orcid.org/0000-0003-0228-6594
Dmitry A. Duev https://orcid.org/0000-0001-5060-8733
Matthew J. Graham https://orcid.org/0000-0002-3168-0139
George Helou https://orcid.org/0000-0003-3367-3415
David L. Kaplan https://orcid.org/0000-0001-6295-2881
Viraj Karambelkar https://orcid.org/0000-0003-2758-159X
Mansi M. Kasliwal https://orcid.org/0000-0002-5619-4938
Erik C. Kool https://orcid.org/0000-0002-7252-3877
S. R. Kulkarni https://orcid.org/0000-0001-5390-8563
Ashish A. Mahabal https://orcid.org/0000-0003-2242-0244
Michael S. Medford https://orcid.org/0000-0002-7226-0659
A. A. Miller https://orcid.org/0000-0001-9515-478X
Jakob Nordin https://orcid.org/0000-0001-8342-6274
Eran Ofek https://orcid.org/0000-0002-6786-8774
Reed Riddle https://orcid.org/0000-0002-0387-370X
Yashvi Sharma https://orcid.org/0000-0003-4531-1745
Roger Smith https://orcid.org/0000-0001-7062-9726
Adam J. Stewart https://orcid.org/0000-0001-8026-5903
Leonardo Tartaglia https://orcid.org/0000-0003-3433-1492
Anastasios Tzanidakis https://orcid.org/0000-0003-0484-3331
Jan Martin Winters https://orcid.org/0000-0001-6114-9173

References

Ahn, C. P., Alexandroff, R., Allende Prieto, C., et al. 2012, ApJS, 203, 21
Andreoni, I., Kool, E. C., Sagués Carracedo, A., et al. 2020, ApJ, 904, 155
Angus, C. 2020, TNSCR, 1392, 1

Arcavi, I., Wolf, W. M., Howell, D. A., et al. 2016, ApJ, 819, 35
Astropy Collaboration, Price-Whelan, A. M., Sipőcz, B. M., et al. 2018, AJ, 156, 123
Astropy Collaboration, Robitaille, T. P., Tollerud, E. J., et al. 2013, A&A, 558, A33
Barnsley, R. M., Smith, R. J., & Steele, I. A. 2012, AN, 333, 101
Bellm, E. C. 2016, PASP, 128, 084501
Bellm, E. C., Kulkarni, S. R., Barlow, T., et al. 2019a, PASP, 131, 068003
Bellm, E. C., Kulkarni, S. R., Graham, M. J., et al. 2019b, PASP, 131, 018002
Bellm, E. C., & Sesar, B. 2016, pyraf-dbsp: Reduction pipeline for the Palomar Double Beam Spectrograph, Astrophysics Source Code Library, ascl:1602.002
Bietenholz, M. F., Margutti, R., Coppejans, D., et al. 2020, MNRAS, 491, 4735
Blagorodnova, N., Neill, J. D., Walters, R., et al. 2018, PASP, 130, 035003
Blanton, M. R., & Roweis, S. 2007, AJ, 133, 734
Boquien, M., Burgarella, D., Roehlly, Y., et al. 2019, A&A, 622, A103
Breeveld, A. A., Landsman, W., Holland, S. T., et al. 2011, in AIP Conf. Ser. 1358, American Institute of Physics Conference Series, ed. J. E. McEnery, J. L. Racusin, & N. Gehrels (Melville, NY: AIP), 373
Bright, J. S., Margutti, R., Matthews, D., et al. 2022, ApJ, 926, 112
Bruch, R., Schulze, S., Yang, Y., et al. 2019, TNSTR, 973, 1
Bruzual, G., & Charlot, S. 2003, MNRAS, 344, 1000
Burgarella, D., Buat, V., & Iglesias-Páramo, J. 2005, MNRAS, 360, 1413
Burrows, D. N., Hill, J. E., Nousek, J. A., et al. 2005, SSRv, 120, 165
Calzetti, D., Armus, L., Bohlin, R. C., et al. 2000, ApJ, 533, 682
Cenko, S. B., Fox, D. B., Moon, D.-S., et al. 2006, PASP, 118, 1396
Cepa, J., Aguiar, M., Escalera, V. G., et al. 2000, Proc. SPIE, 4008, 623
Chabrier, G. 2003, PASP, 115, 763
Chambers, K. C., Boer, T. D., Bulger, J., et al. 2019, TNSTR, 1814, 1
Chambers, K. C., Boer, T. D., Bulger, J., et al. 2020, TNSTR, 3320, 1
Chambers, K. C., Magnier, E. A., Metcalfe, N., et al. 2016, arXiv:1612.05560
Chen, C., & Shen, R.-F. 2022, RAA, 22, 035017
Chen, P., Dong, S., Stritzinger, M. D., et al. 2020, ApJL, 889, L6
Cook, D. O., Kasliwal, M. M., Van Sistine, A., et al. 2019, ApJ, 880, 7
Coppejans, D. L., Margutti, R., Terreran, G., et al. 2020, ApJL, 895, L23
Cutri, R. M., Wright, E. L., Conrow, T., et al. 2013, Explanatory Supplement to the AllWISE Data Release Products
Dahiwale, A., & Fremling, C. 2019, TNSCR, 2407, 1
Dahiwale, A., & Fremling, C. 2020a, TNSCR, 1756, 1
Dahiwale, A., & Fremling, C. 2020b, TNSCR, 2234, 1
Dale, D. A., Helou, G., Magdis, G. E., et al. 2014, ApJ, 784, 83
De, K. 2020a, TNSTR, 1294, 1
De, K., Fremling, U. C., Gal-Yam, A., et al. 2021, ApJL, 907, L18
De, K., Kasliwal, M. M., Tzanidakis, A., et al. 2020, ApJ, 905, 58
de Vaucouleurs, G., & Corwin, H. G., Jr. 1985, ApJ, 295, 287
Dekany, R., Smith, R. M., Riddle, R., et al. 2020, PASP, 132, 038001
DESI Collaboration, Aghamousa, A., Aguilar, J., et al. 2016, arXiv:1611.00036
Dey, A., Schlegel, D. J., Lang, D., et al. 2019, AJ, 157, 168
Djupvik, A. A., & Andersen, J. 2010, ASSP, 14, 211
Drout, M. R., Chornock, R., Soderberg, A. M., et al. 2014, ApJ, 794, 23
Drout, M. R., Soderberg, A. M., Gal-Yam, A., et al. 2011, ApJ, 741, 97
Drout, M. R., Soderberg, A. M., Mazzali, P. A., et al. 2013, ApJ, 774, 58
Duev, D. A., Mahabal, A., Masci, F. J., et al. 2019, MNRAS, 489, 3582
Elbaz, D., Daddi, E., Le Borgne, D., et al. 2007, A&A, 468, 33
Evans, P. A., Beardmore, A. P., Page, K. L., et al. 2007, A&A, 469, 379
Evans, P. A., Beardmore, A. P., Page, K. L., et al. 2009, MNRAS, 397, 1177
Faber, S. M., Willmer, C. N. A., Wolf, C., et al. 2007, ApJ, 665, 265
Fabricant, D., Fata, R., Epps, H., et al. 2019, PASP, 131, 075004
Fitzpatrick, E. L. 1999, PASP, 111, 63
Forster, F. 2019, TNSTR, 1906, 1
Forster, F., Bauer, F. E., Galbany, L., et al. 2020a, TNSTR, 1380, 1
Forster, F., Bauer, F. E., Munoz-Arancibia, A., et al. 2020b, TNSTR, 3172, 1
Förster, F., Cabrera-Vives, G., Castillo-Navarrete, E., et al. 2021, AJ, 161, 242
Forster, F., Hernandez-Garcia, L., Munoz-Arancibia, A., et al. 2020c, TNSTR, 2542, 1
Forster, F., Pignata, G., Bauer, F. E., et al. 2020d, TNSTR, 278, 1
Forster, F., Pignata, G., Bauer, F. E., et al. 2020e, TNSTR, 225, 1
Fox, O. D., & Smith, N. 2019, MNRAS, 488, 3772
Fremling, C. 2019, TNSTR, 1272, 1
Fremling, C. 2020, TNSTR, 3094, 1
Fremling, C., Dugas, A., & Sharma, Y. 2018, TNSCR, 1567, 1
Fremling, C., Ko, H., Dugas, A., et al. 2019, ApJL, 878, L5
Fremling, C., Miller, A. A., Sharma, Y., et al. 2020, ApJ, 895, 32
Fremling, C., Sollerman, J., Taddia, F., et al. 2016, A&A, 593, A68
Gagliano, A., Izzo, L., Kilpatrick, C. D., et al. 2022, ApJ, 924, 55
Gal-Yam, A. 2017, in Handbook of Supernovae, ed. A. W. Alsabti & P. Murdin (Cham: Springer), 195
Gal-Yam, A. 2021, TNSCR, 547, 1
Gehrels, N., Chincarini, G., Giommi, P., et al. 2004, ApJ, 611, 1005
Graham, M. J., Kulkarni, S. R., Bellm, E. C., et al. 2019, PASP, 131, 078001
Graham, M. L., Connolly, A. J., Ivezić, Ž., et al. 2018, AJ, 155, 1
Gromadzki, M., Wevers, T., Lyman, J., & Yaron, O. 2018, TNSCR, 1410, 1
Gutiérrez, C. P., Anderson, J. P., Sullivan, M., et al. 2018, MNRAS, 479, 3232
Ho, A. Y. Q., Goldstein, D. A., Schulze, S., et al. 2019a, ApJ, 887, 169
Ho, A. Y. Q., Margalit, B., Bremer, M., et al. 2022a, ApJ, 932, 116
Ho, A. Y. Q., Perley, D. A., Beniamini, P., et al. 2020a, ApJ, 905, 98
Ho, A. Y. Q., Perley, D. A., Kulkarni, S. R., et al. 2020b, ApJ, 895, 49
Ho, A. Y. Q., Perley, D. A., Yao, Y., et al. 2022b, ApJ, 938, 85
Ho, A. Y. Q., Phinney, E. S., Ravi, V., et al. 2019b, ApJ, 871, 73
Högbom, J. A. 1974, A&AS, 15, 417
Hook, I. M., Jørgensen, I., Allington-Smith, J. R., et al. 2004, PASP, 116, 425
Horesh, A., Sfaradi, I., Ergon, M., et al. 2020, ApJ, 903, 132
Hosseinzadeh, G., Arcavi, I., Valenti, S., et al. 2017, ApJ, 836, 158
Hosseinzadeh, G., McCully, C., Zabludoff, A. I., et al. 2019, ApJL, 871, L9
Hotan, A. W., Bunton, J. D., Chippendale, A. P., et al. 2021, PASA, 38, e009
Hunter, J. D. 2007, CSE, 9, 90
Immler, S., Modjaz, M., Landsman, W., et al. 2008, ApJL, 674, L85
Inserra, C. 2019, NatAs, 3, 697
Irani, I., Prentice, S. J., Schulze, S., et al. 2022, ApJ, 927, 10
Irani, I., Schulze, S., Gal-Yam, A., et al. 2019, ApJ, 887, 127
Jacobson-Galán, W. V., Margutti, R., Kilpatrick, C. D., et al. 2020, ApJ, 898, 166
Kansky, J., Chilingarian, I., Fabricant, D., et al. 2019, PASP, 131, 075005
Karamehmetoglu, E., Fransson, C., Sollerman, J., et al. 2021, A&A, 649, A163
Kasliwal, M. M., Cannella, C., Bagdasaryan, A., et al. 2019, PASP, 131, 038003
Kulkarni, S. R., Harrison, F. A., Grefenstette, B. W., et al. 2021, arXiv:2111.15608
Lacy, M., Baum, S. A., Chandler, C. J., et al. 2020, PASP, 132, 035001
Lang, D. 2014, AJ, 147, 108
Li, W., Chornock, R., Leaman, J., et al. 2011, MNRAS, 412, 1473
Lintott, C., Schawinski, K., Bamford, S., et al. 2011, MNRAS, 410, 166
Lintott, C. J., Schawinski, K., Slosar, A., et al. 2008, MNRAS, 389, 1179
Lyutikov, M. 2022, MNRAS, 515, 2293
Mahabal, A., Rebbapragada, U., Walters, R., et al. 2019, PASP, 131, 038002
Mainzer, A., Bauer, J., Cutri, R. M., et al. 2014, ApJ, 792, 30
Margutti, R., Metzger, B. D., Chornock, R., et al. 2019, ApJ, 872, 18
Marques-Chaves, R., Perez-Fournon, I., Angel, C. J., et al. 2020, TNSTR, 1781, 1
Martin, D. C., Fanson, J., Schiminovich, D., et al. 2005, ApJL, 619, L1
Masci, F. J., Laher, R. R., Rusholme, B., et al. 2019, PASP, 131, 018003
Matheson, T., Filippenko, A. V., Chornock, R., Leonard, D. C., & Li, W. 2000, AJ, 119, 2303
McBrien, O. R., Smartt, S. J., Chen, T.-W., et al. 2019, ApJL, 885, L23
McConnachie, A. W. 2012, AJ, 144, 4
McConnell, D., Hale, C. L., Lenc, E., et al. 2020, PASA, 37, e048
McMullin, J. P., Waters, B., Schiebel, D., Young, W., & Golap, K. 2007, in ASP Conf. Ser. 376, CASA Architecture and Applications, ed. R. A. Shaw, F. Hill, & D. J. Bell (San Francisco, CA: ASP), 127
Meisner, A. M., Lang, D., & Schlegel, D. J. 2017, AJ, 153, 38
Metzger, B. D. 2022, ApJ, 932, 84
Modjaz, M., Blondin, S., Kirshner, R. P., et al. 2014, AJ, 147, 99
Murphy, T., Chatterjee, S., Kaplan, D. L., et al. 2013, PASA, 30, e006
Nayana, A. J., & Chandra, P. 2021, ApJL, 912, L9
Noll, S., Burgarella, D., Giovannoli, E., et al. 2009, A&A, 507, 1793
Nordin, J., Brinnel, V., Giomi, M., et al. 2019a, TNSTR, 543, 1
Nordin, J., Brinnel, V., Giomi, M., et al. 2019b, TNSTR, 720, 1
Nordin, J., Brinnel, V., Giomi, M., et al. 2019c, TNSTR, 1258, 1
Nordin, J., Brinnel, V., Giomi, M., et al. 2019d, TNSTR, 1461, 1
Nordin, J., Brinnel, V., Giomi, M., et al. 2019e, TNSTR, 1984, 1
Nordin, J., Brinnel, V., Giomi, M., et al. 2019f, TNSTR, 2389, 1
Nordin, J., Brinnel, V., Giomi, M., et al. 2020, TNSTR, 356, 1
Nordin, J., Brinnel, V., van Santen, J., et al. 2019g, A&A, 631, A147
Ofek, E. O., Adams, S. M., Waxman, E., et al. 2021, ApJ, 922, 247
Ofek, E. O., & Ben-Ami, S. 2020, PASP, 132, 125004
Ofek, E. O., Fox, D., Cenko, S. B., et al. 2013, ApJ, 763, 42
Ofek, E. O., Rabinak, I., Neill, J. D., et al. 2010, ApJ, 724, 1396
Oke, J. B., Cohen, J. G., Carr, M., et al. 1995, PASP, 107, 375
Oke, J. B., & Gunn, J. E. 1982, PASP, 94, 586
Pastorello, A., Hadjiyska, E., Rabinowitz, D., et al. 2015, MNRAS, 449, 1954

Pastorello, A., Quimby, R. M., Smartt, S. J., et al. 2008, MNRAS, 389, 131
Patterson, M. T., Bellm, E. C., Rusholme, B., et al. 2019, PASP, 131, 018001
Pellegrino, C., Howell, D. A., Vinkó, J., et al. 2022, ApJ, 926, 125
Perets, H. B., Badenes, C., Arcavi, I., Simon, J. D., & Gal-yam, A. 2011, ApJ, 730, 89
Perley, D. 2021, TNSCR, 570, 1
Perley, D., Yao, Y., & Ho, A. 2021a, TNSTR, 443, 1
Perley, D. A. 2019, PASP, 131, 084503
Perley, D. A., Fremling, C., Sollerman, J., et al. 2020, ApJ, 904, 35
Perley, D. A., Ho, A. Y. Q., Yao, Y., et al. 2021b, MNRAS, 508, 5138
Perley, D. A., Mazzali, P. A., Yan, L., et al. 2019, MNRAS, 484, 1031
Perley, D. A., Sollerman, J., Schulze, S., et al. 2022, ApJ, 927, 180
Perley, R. A., Chandler, C. J., Butler, B. J., & Wrobel, J. M. 2011, ApJL, 739, L1
Piascik, A. S., Steele, I. A., Bates, S. D., et al. 2014, Proc. SPIE, 9147, 91478H
Planck Collaboration, Ade, P. A. R., Aghanim, N., et al. 2016, A&A, 594, A13
Poznanski, D., Chornock, R., Nugent, P. E., et al. 2010, Sci, 327, 58
Prentice, S. J., Maguire, K., Boian, I., et al. 2020a, MNRAS, 499, 1450
Prentice, S. J., Maguire, K., Flörs, A., et al. 2020b, A&A, 635, A186
Prentice, S. J., Maguire, K., Skillen, K., Magee, M. R., & Clark, P. 2019, TNSCR, 567, 1
Prentice, S. J., Maguire, K., Smartt, S. J., et al. 2018, ApJL, 865, L3
Pritchard, T. A., Bensch, K., Modjaz, M., et al. 2021, ApJ, 915, 121
Pursiainen, M., Childress, M., Smith, M., et al. 2018, MNRAS, 481, 894
Rest, A., Garnavich, P. M., Khatami, D., et al. 2018, NatAs, 2, 307
Rho, J., Evans, A., Geballe, T. R., et al. 2021, ApJ, 908, 232
Ricker, G. R., Winn, J. N., Vanderspek, R., et al. 2014, Proc. SPIE, 9143, 914320
Rigault, M. 2018, ztfquery, a python tool to access ZTF data, Zenodo, doi:10.5281/zenodo.1345222
Rigault, M., Neill, J. D., Blagorodnova, N., et al. 2019, A&A, 627, A115
Rivera Sandoval, L. E., Maccarone, T. J., Corsi, A., et al. 2018, MNRAS, 480, L146
Roming, P. W. A., Kennedy, T. E., Mason, K. O., et al. 2005, SSRv, 120, 95
Sagiv, I., Gal-Yam, A., Ofek, E. O., et al. 2014, AJ, 147, 79
Sanders, N. E., Soderberg, A. M., Foley, R. J., et al. 2013, ApJ, 769, 39
Sault, R. J., Teuben, P. J., & Wright, M. C. H. 1995, in ASP Conf. Ser. 77, A Retrospective View of MIRIAD, ed. R. A. Shaw, H. E. Payne, & J. J. E. Hayes (San Francisco, CA: ASP), 433
Schlafly, E. F., & Finkbeiner, D. P. 2011, ApJ, 737, 103
Schmidt, B. P., Kirshner, R. P., Eastman, R. G., et al. 1993, Natur, 364, 600
Schulze, S., Yaron, O., Sollerman, J., et al. 2021, ApJS, 255, 29
Shivvers, I., Zheng, W. K., Mauerhan, J., et al. 2016, MNRAS, 461, 3057
Siebert, M. R., Tinyanont, S., Taggart, K., Dimitriadis, G., & Foley, R. J. 2020, TNSCR, 3121, 1
Silverman, J. M., Foley, R. J., Filippenko, A. V., et al. 2012, MNRAS, 425, 1789
Skrutskie, M. F., Cutri, R. M., Stiening, R., et al. 2006, AJ, 131, 1163
Smartt, S. J., Valenti, S., Fraser, M., et al. 2015, A&A, 579, A40
Smith, K. W., Smartt, S. J., Young, D. R., et al. 2020a, PASP, 132, 085002
Smith, M., Möller, A., Amenouche, M., et al. 2020b, TNSAN, 39, 1
Smith, N., Kilpatrick, C. D., Mauerhan, J. C., et al. 2017, MNRAS, 466, 3021
Smith, N., Mauerhan, J. C., Silverman, J. M., et al. 2012, MNRAS, 426, 1905
Soumagnac, M. T., & Ofek, E. O. 2018, PASP, 130, 075002
Steele, I. A., Smith, R. J., Rees, P. C., et al. 2004, Proc. SPIE, 5489, 679
Tachibana, Y., & Miller, A. A. 2018, PASP, 130, 128001
Taggart, K., & Perley, D. A. 2021, MNRAS, 503, 3931
Tampo, Y., Tanaka, M., Maeda, K., et al. 2020, ApJ, 894, 27
Tanaka, M., Tominaga, N., Morokuma, T., et al. 2016, ApJ, 819, 5
Tonry, J., Denneau, L., Heinze, A., et al. 2019a, TNSTR, 1194, 1
Tonry, J., Denneau, L., Heinze, A., et al. 2019b, TNSTR, 1694, 1
Tonry, J., Denneau, L., Heinze, A., et al. 2019c, TNSTR, 2014, 1
Tonry, J., Denneau, L., Heinze, A., et al. 2020, TNSTR, 1158, 1
Tonry, J., Stalder, B., Denneau, L., et al. 2018a, TNSTR, 1379, 1
Tonry, J. L., Denneau, L., Heinze, A. N., et al. 2018b, PASP, 130, 064505
van Dokkum, P. G., Abraham, R., Merritt, A., et al. 2015, ApJL, 798, L45
Vinkó, J., Yuan, F., Quimby, R. M., et al. 2015, ApJ, 798, 12
Virtanen, P., Gommers, R., Oliphant, T. E., et al. 2020, NatMe, 17, 261
Whitesides, L., Lunnan, R., Kasliwal, M. M., et al. 2017, ApJ, 851, 107
Williamson, M., Modjaz, M., & Bianco, F. B. 2019, ApJL, 880, L22
Willingale, R., Starling, R. L. C., Beardmore, A. P., Tanvir, N. R., & O'Brien, P. T. 2013, MNRAS, 431, 394
Wiseman, P., Angus, C., Smith, M., et al. 2019, TNSAN, 56, 1
Wiseman, P., Pursiainen, M., Childress, M., et al. 2020, MNRAS, 498, 2575
Wright, A. H., Robotham, A. S. G., Bourne, N., et al. 2016, MNRAS, 460, 765
Wright, E. L., Eisenhardt, P. R. M., Mainzer, A. K., et al. 2010, AJ, 140, 1868
Xiang, D., Wang, X., Lin, W., et al. 2021, ApJ, 910, 42
Yao, Y., De, K., Kasliwal, M. M., et al. 2020, ApJ, 900, 46
Yao, Y., Ho, A. Y. Q., Medvedev, P., et al. 2022, ApJ, 934, 104
Yao, Y., Miller, A. A., Kulkarni, S. R., et al. 2019, ApJ, 886, 152
Yaron, O., & Gal-Yam, A. 2012, PASP, 124, 668
Zackay, B., Ofek, E. O., & Gal-Yam, A. 2016, ApJ, 830, 27
Zhang, M., Ding, Y., Liu, S., et al. 2018, TNSTR, 1393, 1